**National Technical University of Athens**
**School of Mechanical Engineering**
**Fluids Section**
**Parallel CFD & Optimization Unit**

# Formulation, Programming and Use of the Continuous Adjoint Method for Proton Exchange Membrane Fuel Cells

# Διατύπωση, Προγραμματισμός και Χρήση της Συνεχούς Συζυγούς Μεθόδου για Κυψέλες Καυσίμου με Μεμβράνη Ανταλλαγής Πρωτονίων

Diploma Thesis

**Othon G. Freskos**

Advisor: Kyriakos C. Giannakoglou, Professor NTUA

Athens, 2026

# Abstract

This work concerns the mathematical formulation of the continuous adjoint method and the programming of the corresponding software for the modelling and adjoint-based optimization of proton exchange membrane fuel cells (PEMFCs) within the OpenFOAM environment. The PEMFC technology is a promising option for future energy conversion systems; the main objective of this study is the improvement of a key performance indicator, namely the generated current density, through the optimization of the porosity distribution in the porous layer.

In the first stage of the work, the open-source OpenFuelCell2 platform is used and extended in order to develop a customized continuous adjoint solver. The primary solver is formulated as a coupled two-phase, multi-species, and multi-region system of equations, in which the conservation equations of mass and momentum, species transport, heat transfer, electric potential, and water diffusion in the membrane are solved. The main advantage of the two-phase solver is that it solves each phase separately, thereby providing higher accuracy in the description of the physical phenomena and improved numerical stability.

Appropriate modifications are made to the original solver to improve the physical consistency of the model. Specifically, an analytical Kozeny–Carman formulation is applied to model porous media resistance as an explicit function of the porosity field, thereby establishing a direct dependence between permeability and porous resistance. In addition, an alternative numerical approach for the computation of the Nernst potential is incorporated into the formulation of the electrochemical source terms.

The development and assessment of the continuous adjoint method is carried out progressively. In the first part, the development focuses exclusively on the electrical domains (proton and electronic), while treating the remaining physical quantities as constant and known. The implementation of the adjoint method is verified through systematic comparison with finite differences.

The adjoint formulation is then extended to include the full model for single-phase flow, including the continuity and momentum conservation equations. This extension leads to the formulation of a system of three adjoint equations. This adjoint model is again verified through comparison with the finite difference method.

Finally, an iterative optimization framework is developed, which is used to update the porosity field with the aim of maximizing the generated current density.

# Περίληψη

Η διπλωματική εργασία αφορά την ανάπτυξη της μαθηματικής διατύπωσης της συνεχούς συζυγούς μεθόδου και, κατ' επέκταση, ενός υπολογιστικού κώδικα για την βελτιστοποίηση μέσω των υπολογισθέντων παραγώγων κυψελών καυσίμου με μεμβράνη ανταλλαγής πρωτονίων (PEMFCs) στο περιβάλλον του OpenFOAM. Η τεχνολογία PEMFC αποτελεί μια πολλά υποσχόμενη επιλογή για μελλοντικά συστήματα μετατροπής ενέργειας. Κύριος στόχος της μελέτης είναι η βελτίωση ενός βασικού δείκτη απόδοσης, της παραγόμενης πυκνότητας ρεύματος, μέσω της βελτιστοποίησης της κατανομής του πορώδους στην πορώδη στρώση.

Στο αρχικό στάδιο της εργασίας, χρησιμοποιείται και επεκτείνεται η ανοικτού κώδικα πλατφόρμα OpenFuelCell2, με απώτερω σκοπό την ανάπτυξη του αντίστοιχου συνεχούς συζυγούς επιλύτη (continuous adjoint solver). Ο πρωτεύων διφασικός επιλύτης διατυπώνεται ως ένα συζευγμένο διφασικό, πολυσυστατικό και πολυπεριοχικό σύστημα, στο οποίο επιλύονται οι εξισώσεις διατήρησης μάζας και ορμής, μεταφοράς χημικών ειδών, μεταφοράς θερμότητας, ηλεκτρικού δυναμικού, καθώς και διάχυσης νερού στη μεμβράνη. Ο διφασικός επιλύτης επιλύει κάθε φάση με τις δικές της εξισώσεις, προσφέροντας έτσι μεγαλύτερη ακρίβεια στην περιγραφή των φαινομένων και βελτιωμένη αριθμητική ευστάθεια.

Πραγματοποιούνται κατάλληλες τροποποιήσεις στον αρχικό επιλύτη με στόχο τη βελτίωση της φυσικής συνέπειας του μοντέλου. Συγκεκριμένα, εφαρμόζεται η αναλυτική διατύπωση Kozeny–Carman για τη μοντελοποίηση της αντίστασης του πορώδους μέσου ως ρητής συνάρτησης του πεδίου πορώδους, καθιερώνοντας έτσι άμεση εξάρτηση μεταξύ διαπερατότητας και πορώδους αντίστασης. Επιπλέον, εισάγεται μια εναλλακτική αριθμητική προσέγγιση για τον υπολογισμό του δυναμικού Nernst, η οποία ενσωματώνεται στη διατύπωση των ηλεκτροχημικών πηγών.

Στη συνέχεια, αναπτύσσεται σταδιακά η συνεχής συζυγής διατύπωση. Σε μια πρώτη φάση, η ανάπτυξη επικεντρώνεται αποκλειστικά στις ηλεκτρικές περιοχές (πρωτονικές και ηλεκτρονικές), θεωρώντας τα υπόλοιπα φυσικά μεγέθη ως σταθερά και γνωστά. Η υλοποίηση της συζυγούς διατύπωσης επαληθεύεται μέσω σύγκρισης με πεπερασμένων διαφορές.

Η συζυγής διατύπωση επεκτείνεται στη συνέχεια ώστε να περιλαμβάνει την πλήρη περιγραφή της μονοφασικής ροής, συμπεριλαμβανομένων των εξισώσεων συνέχειας και διατήρησης της ορμής. Η επέκταση αυτή οδηγεί σε σύστημα τριών συζυγών εξισώσεων. Το προγραμματισθέν συζυγές μοντέλο επαληθεύεται επίσης μέσω συγκρίσης με πεπερασμένες διαφορές.

Τέλος, αναπτύσσεται ένα επαναληπτικό πλαίσιο βελτιστοποίησης για την ενημέρωση του πεδίου πορώδους με στόχο τη μεγιστοποίηση της παραγόμενης πυκνότητας ρεύματος.

# Acknowledgements

First, I would like to express my sincere gratitude to my supervisor, Professor Kyriakos Giannakoglou, for providing me with the opportunity to work on this challenging and highly interesting topic, as well as for his continuous guidance and invaluable support throughout the preparation of this diploma thesis. I would also like to sincerely thank Dr. Varvara Asouti for her valuable guidance, continuous support, and constructive discussions throughout the preparation of this diploma thesis. Her expertise in computational fluid dynamics, adjoint methods, and optimization techniques has significantly contributed to this work and to my understanding of PEMFC modelling and optimization. I am also grateful to Dr. Evangelos Papoutsis–Kiachagias for his support and valuable assistance, particularly in OpenFOAM programming, where his deep knowledge was especially helpful in the development of this work.

Finally, I would like to express my appreciation to all the members of the research group PCOpt NTUA who contributed, directly or indirectly, to the completion of this work through their support, discussions, and scientific collaboration.

# Contents

# List of Abbreviations

**PEMFC** Proton Exchange Membrane Fuel Cell

**CFD** Computational Fluid Dynamics

**FDs** Finite Differences

**GDL** Gas Diffusion Layer

**CL** Catalyst Layer

**MPL** Microporous Layer

**HOR** Hydrogen Oxidation Reaction

**ORR** Oxygen Reduction Reaction

# Chapter 1

# Introduction

## 1.1 Fuel Cells and PEMFC Technology

A fuel cell is an electrochemical energy conversion device that transforms the chemical energy of a fuel($H_2$) directly into electrical energy through electron transfer redox reactions. Among the various types of fuel cells, hydrogen-based systems have gained particular attention due to their high efficiency and environmentally friendly operation. In contrast to conventional combustion-based power generation technologies, fuel cells produce electricity with zero emissions, as their primary by-products are water and heat. This makes them a promising technology in the transition towards sustainable and low-carbon energy systems. Proton Exchange Membrane Fuel Cells (PEMFCs) represent one of the most widely studied and commercially promising fuel cell technologies. Their operation relies on a solid polymer electrolyte membrane that allows the transport of protons while acting as an electrical insulator between the electrodes. As shown in Fig. 1.1, hydrogen is supplied to the anode, where it dissociates into protons and electrons. The protons migrate through the membrane to the cathode, while the electrons travel through an external circuit, generating electric current. At the cathode, oxygen reacts with the protons and electrons to form water. The overall process is efficient, clean, and suitable for a wide range of applications, including automotive systems, portable power devices, and stationary energy generation. The reactions taking place both in anode and in cathode are shown in Fig. 1.2.

## 1.2 Challenges and Multiphysics Nature of PEMFCs

PEMFCs offer several advantages, such as high power density, fast start-up times, and relatively low operating temperatures, typically in the range of 60–80°C. These characteristics make them particularly attractive for transportation applications, where rapid response and compact design are essential. However, despite their advantages, several technical

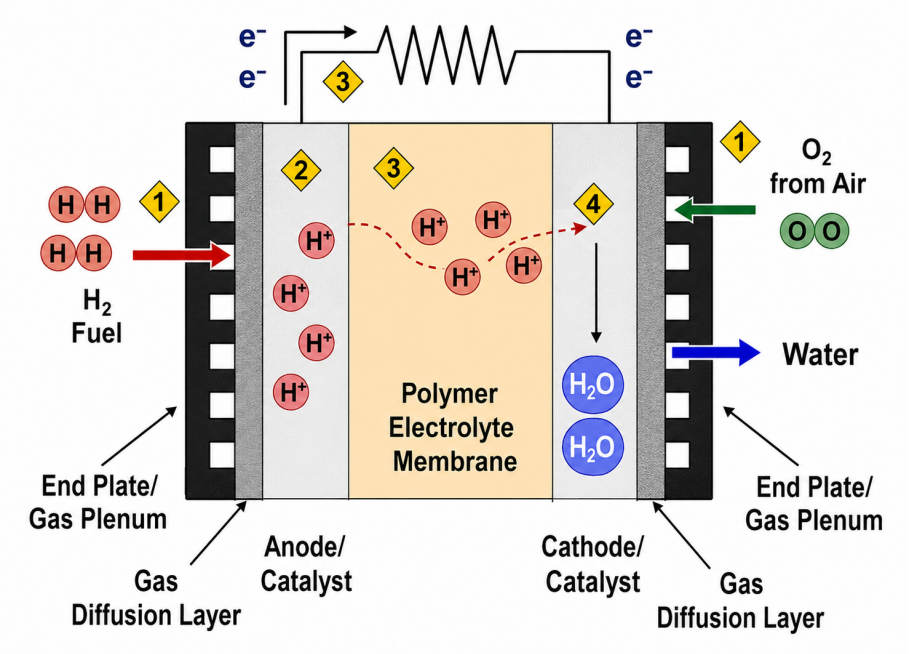


Figure 1.1: Schematic representation of a Proton Exchange Membrane Fuel Cell (PEMFC) (not to scale), illustrating its main components, including the bipolar plates (BP), gas channels (GC), gas diffusion layers (GDL), catalyst layers (CL), and the polymer electrolyte membrane. Hydrogen is supplied to the anode, where it dissociates into protons and electrons, while oxygen is supplied to the cathode, where water is produced. Source: From [9]

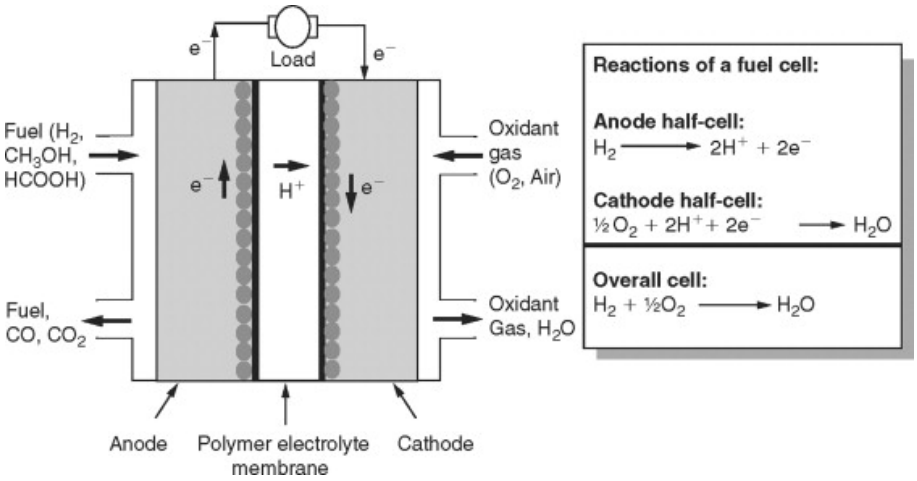


Figure 1.2: Electrochemical reactions in a PEMFC. The transport of electrons through the external circuit produces electrical power. Source: From [2]

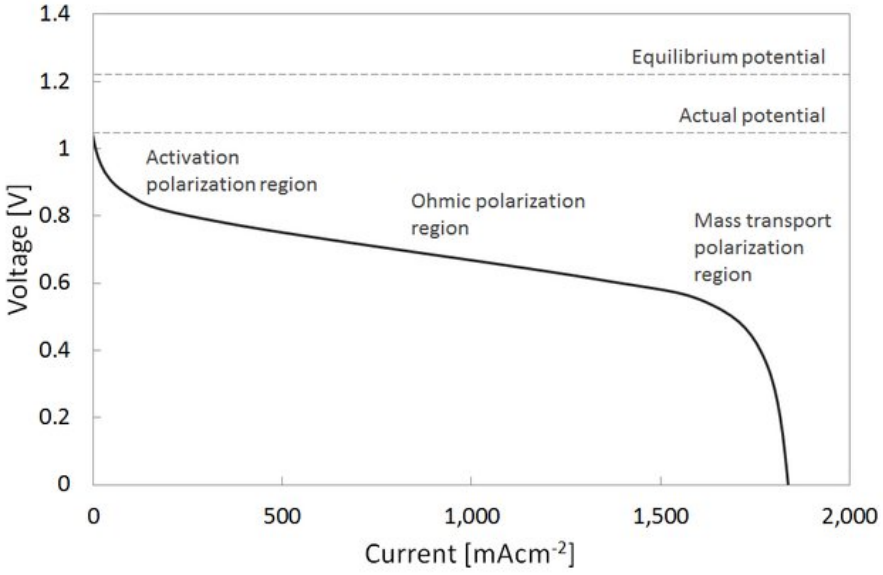


Figure 1.3: Typical polarization curve of a PEMFC, showing the relationship between cell voltage and current density. The three main loss regions are identified: activation losses at low current densities, ohmic losses at intermediate currents, and concentration-mass transport losses at high current densities. Source: From [16]

challenges remain: water management, durability, cost reduction, and performance optimization. Efficient water management is especially critical, as both flooding and membrane dehydration can significantly degrade performance [11].

As shown in Fig. 1.3, this is a typical polarization curve of a PEMFC. The polarization curve describes the relationship between the cell voltage and the current density, and is a fundamental diagnostic tool for assessing fuel cell performance. In general, the curve shows decreasing voltage as current density increases, due to various irreversibilities in the system.

Three main loss regions are identified [4]: activation losses at low current densities, which are associated with the kinetics of the electrochemical reactions; ohmic losses at intermediate current densities, caused primarily by ionic and electronic resistances within the membrane, electrodes, and interconnects; and concentration (mass transport) losses at high current densities, which arise from limitations in reactant transport to the catalytic sites. The maximum voltage is observed at open-circuit conditions at the beginning of the curve, where no current is drawn from the cell.

## 1.3 Regions of a PEMFC

As shown in Fig. 1.1, the PEMFC consists of several distinct regions, which can be broadly classified into porous layers, solid conductive structures, and fluid channels. The porous regions include the Catalyst Layer (CL) and the Gas Diffusion Layer (GDL), while the

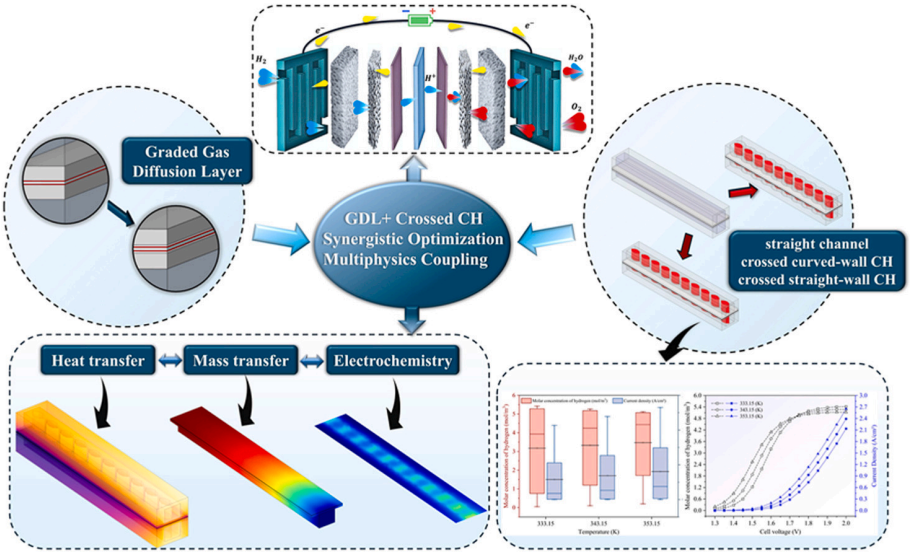


Figure 1.4: Illustration of the multiphysics nature of PEM fuel cell operation, highlighting the coupling between fluid flow, species transport, electrochemical reactions, and heat transfer within the different layers of the cell. Source: From [19]

solid structures are represented by the Bipolar plates(BPs). In addition, the cell contains fluid flow channels that enable the transport of reactant gases.

The membrane is a key component of the PEMFC and acts as a proton-conducting electrolyte. Its primary function is to allow the transport of protons from the anode to the cathode while preventing the crossover of electrons and reactant gases. In this way, the membrane ensures charge separation and enables the electrochemical reactions to proceed efficiently.

The fluid channels are responsible for distributing reactant gases, namely hydrogen at the anode and oxygen (or air) at the cathode. They also facilitate the removal of product water from the cell. The geometry and flow conditions within these channels significantly influence the uniformity of reactant distribution and the overall mass transport behaviour.

The bipolar plates provide structural support to the cell and serve as current collectors. They conduct electrons between adjacent cells in a stack configuration and ensure uniform current distribution. Additionally, they incorporate the flow field channels and contribute to thermal management and mechanical integrity of the system.

It is important to note the presence of the porous regions, namely the GDL and the CL, Fig. 1.1. The GDL serves as a transport medium for reactant gases, liquid water, and electrons, while also providing structural support and ensuring uniform distribution of species to the catalyst layer. On the other hand, CL is the electrochemically active region where the oxygen reduction reaction and hydrogen oxidation reaction take place.

The porosity within these porous layers plays a crucial role in determining the effective transport properties, including permeability, diffusivity, and water management. In the optimization, the porosity value of each region is considered as the primary design variable, as will be discussed in subsequent sections. Its value significantly influences both mass transport characteristics and the overall performance of the fuel cell.

Among the various components of a PEMFC, the GDL plays a particularly critical role in performance. It acts as a porous transport medium that facilitates the delivery of reactants to the catalyst layer, supports the removal of liquid water generated during operation, and enables electronic conduction toward the bipolar plates. The microstructure and porosity of the GDL strongly affect mass transport resistance and the overall cell efficiency. This is why, the optimization of porosity distribution within the GDL has become an active area of research [7][10][20].

## 1.4 Numerical Modeling of PEMFCs

The operation of a PEMFC involves complex interactions between several physical processes, including fluid flow, heat transfer, electrochemical reactions, and species transport. These coupled phenomena occur across several spatial scales, ranging from the microscopic structure of porous materials to the macroscopic flow channels. As a result, experimental investigation alone is often insufficient to fully understand and optimize the PEMFC performance. Instead, numerical modeling and simulation have become essential tools in fuel cell research.

Early numerical models of PEMFCs were relatively simple and relied on 1D or 2D approximations. These models provided valuable insight into fundamental processes but were limited in their ability to capture the complexity of the system. For instance, simplified isothermal and single-phase models have been used to study the influence of transport properties such as diffusivity and conductivity on current density distribution, particularly at the interface between the gas diffusion layer (GDL) and the catalyst layer (CL) [18].

More advanced models incorporate multiphase flow and detailed transport mechanisms. One of the key challenges in PEMFC modeling is the accurate representation of water transport within the porous media and the membrane. Water exists in both vapor and liquid phases, and its distribution significantly affects the performance of the cell. Two main approaches have been developed for modeling two-phase flow: the mixture model and the two-fluid model. The mixture model [10] treats the liquid and gas phases as a single effective medium with averaged properties, while the two-fluid model [22] solves separate conservation equations for each phase. Although both approaches have been successfully applied in the literature, the two-fluid model provides a more detailed description of phase interactions and is, therefore, adopted in the present work.

## 1.5 CFD Modeling and Optimization of PEMFCs

The development of Computational Fluid Dynamics (CFD) tools has significantly advanced the study of PEMFCs. CFD enables the simulation of complex geometries and detailed physical processes, allowing researchers to analyze flow distribution, species transport, and electrochemical reactions within the cell. Open-source platforms such as OpenFOAM have gained popularity due to their flexibility and extensibility. Several studies have

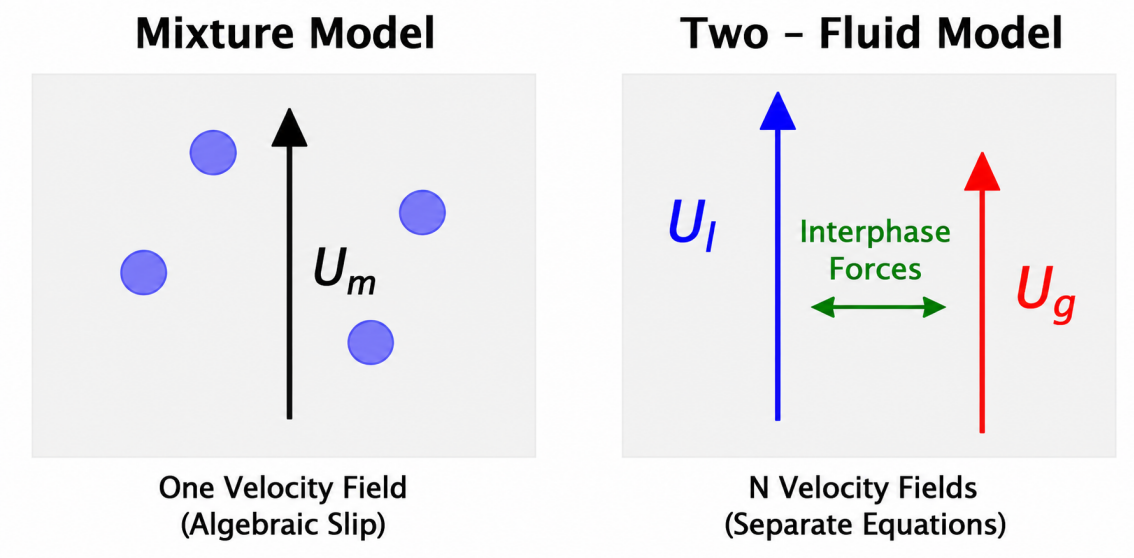


Figure 1.5: Conceptual comparison between the mixture model and the two-fluid model for two-phase flow in PEMFCs. The mixture model treats liquid water and gas as a single working fluid with averaged properties, whereas the two-fluid model solves separate conservation equations for each phase, allowing a more detailed representation of phase interactions.

utilized OpenFOAM to simulate PEMFC behavior, although many of these implementations rely on simplified assumptions, such as isothermal conditions or single-phase flow.

Beyond simulation, optimization plays a crucial role in PEMFC design. The performance of a fuel cell depends on numerous parameters, including geometric characteristics, material properties, and operating conditions. Optimization techniques aim to identify the best combination of these parameters to maximize performance metrics such as current density, power output, and efficiency. Various optimization methods have been applied in the literature, ranging from gradient-based to stochastic ones, such as evolutionary algorithms.

In the past, relevant work has been conducted within the PCOpt/NTUA group, focusing on the analysis and optimization of PEMFCs in the OpenFOAM environment. In [10], a 3D, liquid-gas mixture CFD model was adapted to simulate PEMFC operation, while optimization techniques were applied to improve performance through the design of porosity distributions in the gas diffusion and catalyst layers. The study employed evolutionary algorithms combined with surrogate models to maximize current density and reduce hydrogen consumption, demonstrating the effectiveness of advanced optimization strategies in PEMFC design. The geometry used in [10] is identical to the one adopted in the present study.

Also, in [7] the effect of the porosity distribution within the GDL of a PEMFC is investigated, aiming to improve the overall cell performance. His work focused on the development of a computational model capable of describing the complex transport phenomena occurring inside the fuel cell, including mass transfer, heat transfer, electrochemical reactions, and two-phase flow processes. The optimization process was subsequently performed using the EASY software developed at NTUA, which is based on evolutionary algorithms.

Through this optimization approach, the spatial distribution of GDL porosity was modified in order to identify improved porosity profiles compared to the conventional uniform distribution. The study demonstrated that an appropriately designed porosity distribution can enhance reactant transport and water management, resulting in improved fuel cell performance. However, the optimal porosity distribution was found to strongly depend on the operating conditions of the fuel cell. The results highlight the importance of tailoring the GDL structure through computational optimization methods to achieve higher efficiency and better electrochemical performance.

Yan et al. [20] employed the Taguchi method in combination with a 3D PEMFC model analysis to systematically investigate the influence of key structural parameters, including the thickness, porosity, and permeability of GDL, as well as the geometry of the flow channels. The geometry adopted in their study is representative of realistic industrial applications. The Taguchi approach [14], based on an orthogonal experimental design, enables the efficient exploration of the design space by reducing the number of required simulations while still capturing the dominant effects of the design parameters.

Their results demonstrated that the porosity and thickness of the GDL are among the most influential parameters governing cell performance. Increased GDL porosity enhances reactant($H_2/O_2$) diffusion and facilitates liquid water removal, thereby reducing mass transport limitations at high current densities. However, excessively high porosity may reduce the mechanical strength of the layer and decrease effective electrical conductivity, leading to increased ohmic losses. Similarly, the GDL thickness presents a trade-off: thinner layers improve reactant transport and reduce diffusion resistance, but may lead to non-uniform reactant distribution and insufficient water management.

[20] also highlighted the critical role of flow channel geometry in determining the uniformity of reactant distribution across the active area of the cell. Optimized channel configurations were shown to improve local current density distribution, reducing regions of reactant starvation and mitigating performance losses associated with concentration overpotentials.

Overall, the application of the Taguchi method allowed the identification of an optimal combination of structural parameters that significantly improved current density and overall fuel cell efficiency, while maintaining a relatively low computational cost compared to exhaustive parametric studies. Similarly, Wang et al. [17] introduced a topology–curvature optimization approach for flow-field design, achieving improved reactant distribution and enhanced power output.

## 1.6 Objectives and Scope of this Diploma Thesis

The present work focuses on the numerical simulation and optimization of PEMFCs using a CFD-based approach. A detailed single-phase model is employed to capture the essential physical processes, while a continuous adjoint-based technique is applied to compute the derivatives of the objective function w.r.t. the porosity distribution and use them in the framework of a gradient based optimization. A performance metric, namely the current

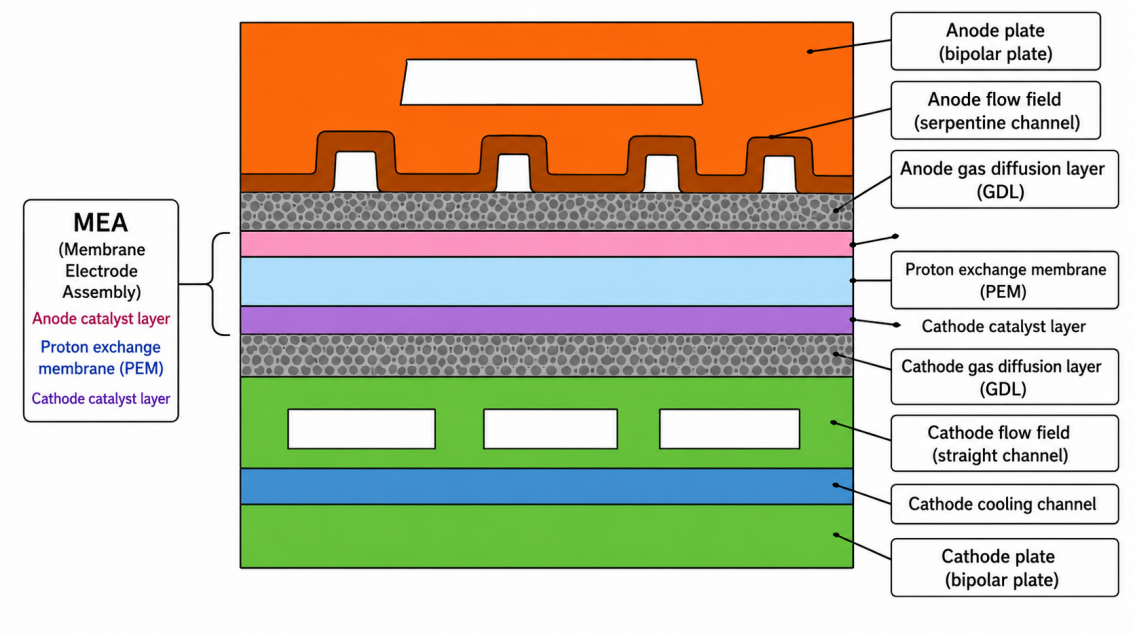


Figure 1.6: Computational domain of the PEMFC used in [20], including the anode and cathode flow channels, gas diffusion layers, catalyst layers, and membrane. Due to geometric symmetry, only half of the domain is modeled, reducing computational cost while preserving accuracy. Source: From [20]

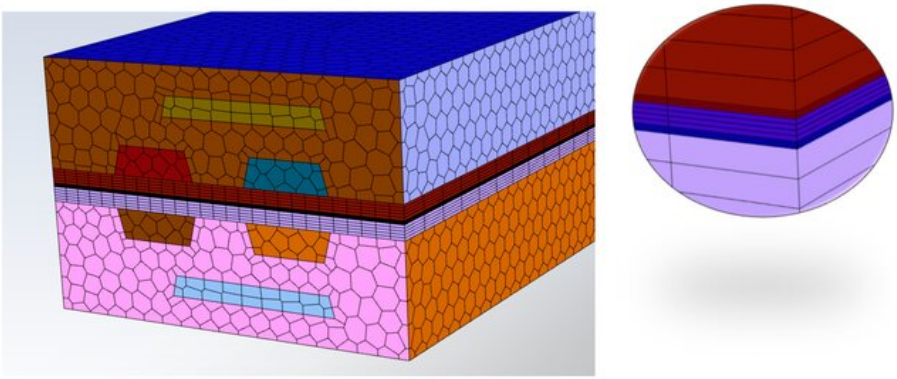


Figure 1.7: Computational mesh used for the numerical simulation of the PEMFC. The domain is discretized into control volumes to numerically solve the governing equations. Source: From [20]

density is used as the objective function to be maximized. The use of OpenFOAM as the computational environment allows for flexibility in model development and scalability of the simulations.

The remainder of this thesis is structured as follows. First, the mathematical model and governing equations of the primal problem, originally developed in [22], are presented, together with the associated modelling assumptions. An analytical Kozeny–Carman formulation is adopted to describe the porous media resistance as an explicit function of the porosity field, thereby establishing a direct relationship between permeability and porous resistance. Furthermore, an alternative numerical approach for the computation of the Nernst potential is incorporated into the formulation of the electrochemical source terms.

Then, a detailed, step-by-step derivation and implementation of the adjoint model is provided. In the initial stage, the adjoint formulation is restricted to the electrical domains, while all other physical fields are assumed to remain fixed. Comparison of the adjoint derivatives with Finite Differences (FDs) is conducted demonstrating excellent agreement.

Thereafter, the formulation is extended to incorporate the continuity and momentum equations for single-phase flow, leading to a fully coupled three-equation adjoint system.

This is followed by the presentation and discussion of verification results, which demonstrate the correctness of the developed adjoint implementation. Finally, the outcomes of an optimization run are presented and discussed, with emphasis on the influence of the design variables on the overall performance of the PEMFC system.

# Chapter 2

# Primal Model Presentation

## 2.1 Computational Domains-Regions

A PEMFC consists of several regions, each governed by different sets of equations. The main regions, as shown in Fig. 2.1, include the air region (Cathode Gas Channel-CGC, Cathode Gas Diffusion Layer- CGDL, Cathode Catalyst Layer-CCL), fuel region (Anode Gas Channel-AGC, Anode Gas Diffusion Layer-AGDL, Anode Gas Catalyst Layer-ACL), electrolyte (membrane), and interconnects (Anode Bipolar Plate-ABP, Cathode Bipolar Plate-CBP).

Initially, a global computational mesh is generated in which the heat transfer equation will be solved over the entire domain. This global mesh is decomposed into multiple adjacent local regions, each of which may belong to more than one domain. For example, the air region is treated both as a fluid domain, where momentum, continuity and species transport equations are solved, and as an electrical domain, where charge conservation is considered.

During the simulation, a coupling strategy is employed between the global and local regions. Material properties, such as density and thermal conductivity, are mapped from the local regions to the global domain, while the temperature field is transferred from the global domain back to the local regions. This bidirectional coupling ensures consistency between thermal and multiphysics solutions across the entire computational domain.

The local regions are classified into three domains : fluid, electric and global.

- Fluid Domain: This domain consists of GCs and porous zones (GDLs,CLs) as shown in Fig. 2.1 and it is where fluid flows. In this domain, the following phenomena are taking place: Fluid flow (single/two-phase), species transfer, electrochemical reaction, heat and mass transfer.

- Electric Domain: This domain represents the electrically conductive components of the system and accounts for charge transport via electrons and ions. In a PEMFC,

two distinct electric subdomains are identified. The electronic domain, where electron transport occurs, comprises the interconnects, GDLs and CLs, as shown in Fig. 2.1. The proton domain, where proton transport takes place, includes the CLs and the membrane. Within this domain, the transport of dissolved water through the membrane is also considered. The governing equations solved in this domain include the electric potential equations (Poisson's equations), as well as the equations modeling dissolved water transport, accounting for both diffusion and electro-osmotic drag.

- Global Domain: The heat source/sinks in local regions are mapped onto this global domain (consists of all the subcomponents that were referred), Heat Transfer equation is solved and, finally, the obtained temperature is mapped back onto the local regions.

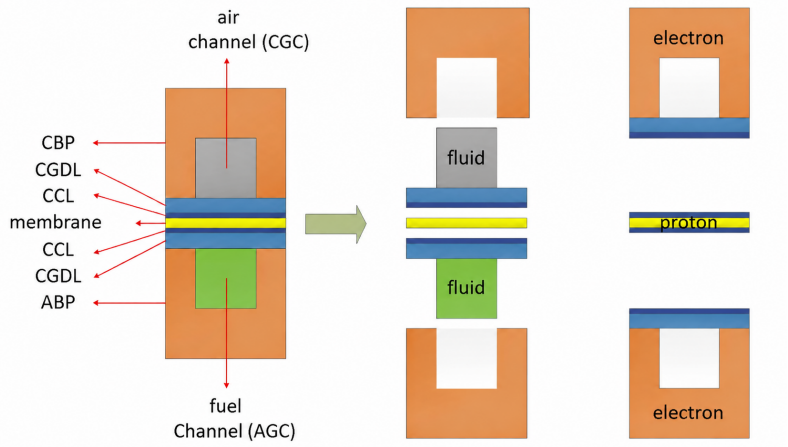


Figure 2.1: Computational Regions-Domains. Source: From [22]

## 2.2 Theoretical Model

### 2.2.1 Assumptions

The basic assumptions made are :

- All gas phase flows are laminar.
- Both phases (liquid-gas) are assumed to be incompressible and the gas mixtures obey the ideal gas law.
- Fick's law is used for multi-component species transfer.
- The properties of the porous materials are treated as homogeneous.

- The membrane is only permeable to water. No crossover of gases is considered for the membrane/electrolyte.
- Produced water is in liquid form at low operating temperatures and in vapor form if the temperature is above 100 C (ambient pressure).
- Gases dissolved in liquid water are not considered.
- Dispersed phases in the gas channels (if present) are treated as if composed of spherical droplets/bubbles.

### 2.2.2 Fluid Domain

**Definition of the Dispersed Phase and Particle Diameter**

Regarding multi-phase flow modeling, in this work, fluid dynamics are modeled using a two phase Euler-Euler framework. In these models, the phases are defined as follows:

- **Continuous Phase:** This represents the gaseous reactant stream (typically humidified air or hydrogen).
- **Dispersed Phase:** This refers to the liquid water phase. Due to the electrochemical reaction and the cooling of humidified gases, water vapor condenses into liquid droplets. These droplets are treated as the dispersed "particles" within the flow field.

The **particle diameter** ($d$) specifically represents the characteristic diameter of these liquid water droplets. In the porous media of CL or GDL, $d$ may also represent an equivalent capillary diameter or the size of water clusters. However, in the flow channels, $d$ is the spherical equivalent diameter of the water droplets transported by the gas stream.

The Reynolds number ($Re$) for the droplet is thus calculated based on the relative velocity $|\mathbf{v}_r|$ between gas (index g) and the liquid droplet (index l):

$$Re = \frac{\rho_g \, d \, |\mathbf{v}_g - \mathbf{v}_l|}{\mu_g}, \tag{2.1}$$

The Schiller–Naumann correlation [12] is subsequently used to determine the drag force exerted by the reactant gas on the liquid water, which is a critical factor in modeling water management and convective removal within the fuel cell.

**Continuity and Momentum equations (GCs,GDLs,CLs)**

In the Eulerian-Eulerian two-phase flow algorithm, the two phases (gaseous and liquid) are typically considered separately, with the gaseous phase treated as the 'continuous' one and the liquid phase as 'dispersed'. Given the assumptions, the continuity and momentum equations are as follows:

$$\frac{\partial(\rho_\phi \alpha_\phi)}{\partial t} + \nabla \cdot (\alpha_\phi \rho_\phi \mathbf{v}_\phi) = R_\phi \tag{2.2}$$

$$\frac{\partial(\rho_\phi \alpha_\phi \mathbf{v}_\phi)}{\partial t} + \nabla \cdot (\alpha_\phi \rho_\phi \mathbf{v}_\phi \mathbf{v}_\phi) + \nabla \cdot \left(\alpha_\phi \boldsymbol{\tau}^\phi\right) = -\alpha_\phi \nabla p + \alpha_\phi \rho_\phi \mathbf{g} + \mathbf{M}_\phi \tag{2.3}$$

- $\phi \in \{l, g\}$ denotes the phase
- $\alpha_\phi$ denotes the phase volume fraction. It is $\alpha_g + \alpha_l = 1$; if $\alpha_g = 1$ there is no liquid phase and the system can be treated as single-phase
- $\rho_\phi$ represents the phase density
- $\mathbf{v}_\phi$ is the phase velocity vector
- $R_\phi$ is the mass source/sink due to electrochemical reaction
- p is the shared pressure of both phases
- $\boldsymbol{\tau}^\phi$ denotes the viscous stress tensor, expressed as:

$$\boldsymbol{\tau}^\phi = \mu_\phi \nabla \mathbf{v}_\phi \tag{2.4}$$

- $\mu_\phi$ is the dynamic viscosity of phase $\phi$.

The momentum interphase exchange term is written as :

$$\mathbf{M}_\phi = \alpha_\phi \left(\mathbf{F}_d + \mathbf{F}_l + \mathbf{F}_{vm}\right) \tag{2.5}$$

This term is common to both phases but, for each phase, appears with opposite signs in the momentum equations. Here:

- $\mathbf{F}_d$ the drag force
- $\mathbf{F}_l$ the lift force
- $\mathbf{F}_{vm}$ the virtual mass force.

The interphase momentum exchange term appears in the momentum balance to account for the mechanical interaction between the phases occupying the same control volume. When relative motion exists between phases, momentum is transferred through interfacial forces such as drag, lift, and virtual mass effects. The virtual mass effect (also called added mass) occurs when a phase must accelerate not only its own mass but also some of the surrounding fluid it displaces. These forces are introduced in the averaged momentum equations as volumetric source terms, scaled by the phase volume fraction.

Therefore, term $\mathbf{M}_\phi$ represents the net rate of momentum exchanged between phase $\phi$ and the surrounding phases per unit control volume.

The drag force becomes significant when a slip velocity exists between phases, and this is expressed as:

$$\mathbf{F}_d = \tfrac{1}{2}\,\rho_\phi\,A\,C_d\,|\mathbf{v}_r|\,v_r \tag{2.6}$$

- $A$ is the projected area (for spherical droplets/bubbles $A = \frac{\pi d^2}{4}$)
- $C_d$ is the drag coefficient.

The drag coefficient can be obtained empirically, for instance, using the Schiller–Naumann model [12]:

$$C_d = \frac{24}{Re}\left(1 + 0.15\,Re^{0.687}\right), \tag{2.7}$$

**Momentum Equations in Porous Regions (CLs and GDLs)**

In porous electrode regions, such as CLs and GDLs, the fluid flow is commonly described using Darcy's law, which accounts for the additional resistance imposed by the porous structure. Therefore, the Navier–Stokes momentum equation is modified by incorporating a Darcy-based resistance term, and becomes:

$$\frac{\partial(\rho_\phi\alpha_\phi\mathbf{v}_\phi)}{\partial t} + \nabla\cdot(\alpha_\phi\rho_\phi\mathbf{v}_\phi\mathbf{v}_\phi) + \nabla\cdot\left(\alpha_\phi\boldsymbol{\tau}^\phi\right) = -\alpha_\phi\nabla p + \alpha_\phi\rho_\phi\mathbf{g} + \mathbf{M}_\phi + \alpha_\phi\mathbf{S}_{\text{Darcy},\phi}, \tag{2.8}$$

The Darcy resistance term describes the interaction between the fluid phase and the solid porous matrix, resulting in a pressure loss and attenuation of the flow velocity. It is expressed as:

$$\mathbf{S}_{\text{Darcy},\phi} = -\left(\mu_\phi\alpha + \frac{1}{2}\rho_\phi|\mathbf{v}_\phi|\beta\right)\mathbf{v}_\phi, \tag{2.9}$$

where $\alpha$ and $\beta$ correspond to the viscous (linear) and inertial (nonlinear) resistance coefficients, respectively. These coefficients are directly related to the geometrical characteristics of the porous medium, particularly its porosity.

The porous resistance coefficients ($\alpha + \beta$) are evaluated using the Carman–Kozeny correlations [1]. This formulation was developed in this diploma thesis and incorporated into the OpenFuelCell2 solver as a new add on, providing a relationship between the permeability characteristics and the structural properties of the porous material.

Eqs. 2.10-2.11 provide the explicit dependence of the viscous and inertial resistance coefficients on the porous medium morphology, by relating $\alpha$ and $\beta$ to the porosity and characteristic pore size through the Carman–Kozeny [1] formulation:

$$\alpha(\varepsilon) = \frac{150(1-\varepsilon)^2}{d_p^2\varepsilon^3}, \tag{2.10}$$

$$\beta(\varepsilon) = \frac{3.5(1-\varepsilon)}{d_p\varepsilon^3}, \tag{2.11}$$

where $d_p$ denotes the characteristic pore diameter and $\varepsilon$ represents the porosity of the porous medium. The aforementioned expressions enable the incorporation of momentum losses within the porous regions into the governing flow equations, thereby providing an accurate representation of the transport phenomena occurring within the CL and GDL. Note that the porosity field is selected as the design variable in the adjoint-based optimization. Consequently, these correlations establish the required sensitivity relationships between the porous resistance and the design variable, enabling the computation of the corresponding sensitivity derivatives within the fluid domain.

It should be noted that the phase pressure $p_\phi$ appears in Eq. 2.8, rather than the shared pressure. Water motion in the porous GDL is driven by the capillary pressure [15], which gives the following relation:

$$p_l = \begin{cases} p_g, & \text{in GCsl} \\ p_g - p_c, & \text{in GDLs and CLs} \end{cases} \tag{2.12}$$

The capillary pressure is often computed using a Leverett $J$-function [8]:

$$p_c = \sigma \cos\theta \sqrt{\frac{K}{\varepsilon}}\, J(\alpha_l), \tag{2.13}$$

- $\sigma$ is the surface tension of the liquid-gas pair
- $\theta$ is the contact angle of the porous material
- $J(\alpha_l)$ is the Leverett function.

The Leverret $J$-function [8] accounts for the non-linear relationship between saturation and capillary pressure. This can be expressed as:

$$J(\alpha_l) = \begin{cases} 1.417(1-\alpha_l) - 2.120(1-\alpha_l)^2 + 1.263(1-\alpha_l)^3, & \theta > 90^\circ \\ 1.417\alpha_l - 2.120\alpha_l^2 + 1.263\alpha_l^3, & \theta < 90^\circ \end{cases} \tag{2.14}$$

**Species Transfer(GCs, GDLs, CLs)**

The mass fraction is a dimensionless quantity defined as the ratio of the mass of species $i$ to the total mass of the mixture:

$$Y_i = \frac{m_i}{m_{total}} \tag{2.15}$$

At the anode, the primary reaction is the Hydrogen Oxidation Reaction (HOR) as shown in Fig.1.2 . The species involved in the gas phase are: $H_2$ and $H_2O$.

At the Cathode, the primary reaction is the Oxygen Reduction Reaction (ORR) as shown in Fig.1.2. The species involved in the gas phase are: $O_2$ , $H_2O$ and $N_2$.

In the modeling of the GCs and porous electrode layers, several simplifying assumptions are made regarding the multi-component transport. It is assumed that the liquid water

phase is pure; thus, the solubility of gaseous species into the liquid water is considered negligible.

Mass transfer within the gaseous phase is governed by multi-component diffusion. To ensure mass conservation, the sum of the mass fractions ($Y_i$) or molar fractions ($x_i$) of all species in each region must equal unity:

$$\sum_{i=1}^{N} Y_i = 1. \tag{2.16}$$

Consequently, for a system consisting of $N$ species, the conservation equation is solved for $N-1$ species and the Y value of the last species results from Eq. 2.16. So:

- **At the Anode:** The system is treated as a binary mixture ($H_2$ and $H_2O$), requiring the transport equation to be solved for $H_2$, while $H_2O$ is obtained as the residual species.
- **At the Cathode:** The system is treated as a ternary mixture ($O_2$, $N_2$, and $H_2O$), requiring the equation to be solved for $O_2$ and $H_2O$, while $N_2$ is obtained as the residual species.

The governing conservation equation for the $i^{th}$ species is expressed as:

$$\frac{\partial}{\partial t}\left(\rho_g\,\alpha_g\,Y_i\right) + \nabla\cdot\left(\alpha_g\,\rho_g\,\mathbf{v}_g\,Y_i\right) = \nabla\cdot\left(\alpha_g\,\rho_g\,D_i^{\text{eff}}\,\nabla Y_i\right) + \alpha_g\,R_i, \tag{2.17}$$

- Subscript $i$ denotes the species component, where $i \in \{H_2\}$ at the anode and $i \in \{H_2, H_2O\}$ at the cathode
- $R_i$ is the species mass source or sink
- $D_i^{\text{eff}}$ is the effective species diffusion coefficient.

**Heat Transfer**

Enthalpy is a global field addressed within the global domain. However, in the presence of multi-phase flow, it becomes necessary to account for the enthalpy of each phase. In this case, the enthalpy of the continuous phase is solved in the global domain, while the enthalpy of the dispersed phase is solved within its respective local fluid region. The governing equation for the enthalpy of each phase is:

$$\frac{\partial}{\partial t}\left(\alpha_\phi\,\rho_\phi\,h_\phi\right) + \nabla\cdot\left(\alpha_\phi\,\rho_\phi\,\mathbf{v}_\phi\,h_\phi\right) = \nabla\cdot\left(\alpha_\phi\,\Gamma_\phi^{\text{eff}}\,\nabla h_\phi\right) + \alpha_\phi\,Q_\phi, \tag{2.18}$$

The thermal source term $Q_\phi$ accounts for the different heat generation and consumption mechanisms occurring within the various regions of the electrochemical cell. The governing terms are defined as follows:

- $h_\phi$ is the enthalpy of phase $\phi$.

- $\Gamma_{\phi}^{\text{eff}}$ is the effective thermal diffusivity.
- $Q_{\phi}$ represents the thermal sources or sinks associated with phase change, interfacial heat transfer, and electrochemical reactions.

### 2.2.3 Electric Domain

In a closed system/circuit, ions/protons are transferred via the electrolyte/membrane, whereas electrons are conducted through the electrodes, interconnects, and the external load. Both are considered to follow Poisson (Ohm's law) type relationships:

$$\nabla \cdot (\sigma_E \nabla \Phi_E) = J_E \tag{2.19}$$

$$\nabla \cdot (\sigma_I \nabla \Phi_I) = J_I \tag{2.20}$$

- $\Phi$ is the potential
- $E$ indices the electronic domains
- $I$ indices proton domain
- $\sigma$ is the electric conductivity
- $J$ refers to the source/sink of charge, due to the electrochemical reaction.

e.g., at the cathode electrode:

$$\begin{cases} J_E = -j_{ae} \\ J_I = j_{ae} \end{cases} \tag{2.21}$$

and at the anode electrode:

$$\begin{cases} J_E = j_{fe} \\ J_I = -j_{fe} \end{cases} \tag{2.22}$$

where $j_{ae}$ is the absolute value of the electric source term at the anode and $j_{fe}$ at the cathode. Both are defined in Eq. 2.30.

#### Electric Conductivity

The electronic conductivity $\sigma_E$ is defined as:

$$\sigma_E = \begin{cases} \text{constant}, & \text{for BPPs} \\ \sigma_0(1-\varepsilon), & \text{for GDLs and CLs} \end{cases} \tag{2.23}$$

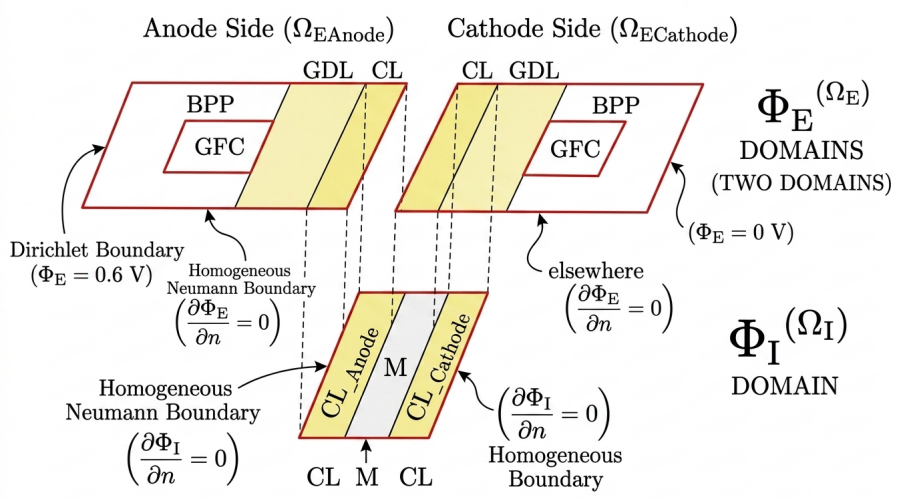


Figure 2.2: Schematic representation of the electronic ($\Phi_e$) and ionic ($\Phi_i$) potential domains. The electronic domain $\Omega_e$ is comprised of the electrically conductive BPs, GDLs, and CLs, while the ionic domain $\Omega_i$ is confined to the membrane and the CLs.

### Ionic Conductivity

The materials employed in typical fuel cells/electrolyzers exhibit much higher electronic than ionic conductivity. The ionic conductivity in the membrane/electrolyte is usually a function of temperature and water content in a low-temperature ($60^o - 90^oC$) PEMFC, or of phosphoric acid doping level in a high-temperature ($120^o - 200^oC$) PEMFC. As an example, the expression for a Nafion-based membrane is:

$$\sigma_0 = \begin{cases} (0.514\lambda - 0.326)\exp\left(1268\left(\frac{1}{303} - \frac{1}{T}\right)\right), & \lambda \geq 1 \\ 0.1879\lambda \exp\left(1268\left(\frac{1}{303} - \frac{1}{T}\right)\right), & \lambda < 1 \end{cases}$$

The ionic conductivity $\sigma_I$ is defined as:

$$\sigma_I = \begin{cases} \text{constant}, & \text{for the membrane} \\ \sigma_0 \left[(1-\varepsilon)\,\text{por}_{\text{Naf}}\right]^{1.5}, & \text{for CLs} \end{cases} \tag{2.24}$$

### Water Transport through the membrane.

The membrane is assumed to be impermeable to reactants/products. However, it selectively permits the cross-over of water. The mechanisms of water transfer include diffusion, electroosmotic drag (EOD), and hydraulic permeation. Diffusion and EOD are usually considered dominant in PEMFCs, and the hydraulic permeability coefficient is typically negligibly small. A non-equilibrium transport equation for water transfer in the membrane can be written as follows:

$$\frac{\rho_m}{EW}\frac{\partial \lambda}{\partial t} + \nabla \cdot \left(\frac{\mathbf{i}_I}{F} n_d\right) = \frac{\rho_m}{EW} \nabla \cdot \left(D_m^{\text{eff}} \nabla \lambda\right) + R_\lambda \tag{2.25}$$

- $\lambda$ represents the water content in molar concentration
- $\rho_m$ is the (dry) membrane density
- $EW$ is the Equivalent Weight, a fundamental property of the ionomer membrane, defined as the mass of the dry polymer per mole of sulfonic acid groups ($-SO_3H$). It is expressed in g $\cdot$ mol$^{-1}$
- $\mathbf{i}_I$ is the ionic current density, defined as

$$\mathbf{i}_I = -\sigma_I \nabla \Phi_I,$$

- $n_d$ is the EOD coefficient
- $D_m^{\text{eff}}$ represents the effective water diffusion coefficient in the membrane
- $R_\lambda$ is the source/sink term of water desorption/adsorption.

### 2.2.4 Global Domain

The governing energy balance for the global domain can be written as:

$$\frac{\partial}{\partial t}\left(\rho C_p T\right) + \rho C_p \mathbf{v} \cdot \nabla T = \nabla \cdot \left(k_{\text{eff}} \nabla T\right) + Q \tag{2.26}$$

- $C_p$ is the specific heat capacity
- $k_{\text{eff}}$ is the effective thermal conductivity
- $Q$ represents the heat sources or sinks transferred from all sub-regions. Depending on the considered domain, the thermal source term is expressed as:
  - BPPs:
$$Q = \frac{i_E^2}{\sigma_E}$$
  - Channels:
$$Q = 0$$
  - GDLs:
$$Q = \frac{i_E^2}{\sigma_E}$$

– CLs:

$$Q = j\left(\eta - \frac{\Delta S T}{zF}\right) + \frac{i_E^2}{\sigma_E} + \frac{i_P^2}{\sigma_P}$$

– Membrane:

$$Q = \frac{i_P^2}{\sigma_P}$$

where

- $i_E$: Electron current density (A/m$^2$), associated with electron transport in the solid conductive phase
- $i_P$: Proton current density (A/m$^2$), associated with ion (proton) transport through the electrolyte or membrane phase
- $\sigma_E$: Electrical conductivity of the electronic phase (S/m), typically associated with solid matrix materials such as catalyst layers or bipolar plates
- $\sigma_P$: Protonic (ionic) conductivity of the polymer electrolyte or membrane (S/m)
- $j$: Volumetric reaction current density (A/m$^3$)
- $\eta$: Activation overpotential (V)
- $\Delta S$: Entropy change of the electrochemical reaction (J/mol·K), defined as:

$$dS_i = C_{p,i}\frac{dT}{T} - R_g\frac{dp_i}{p_i} \tag{2.27}$$

- $z$: Number of electrons transferred per reaction event (dimensionless)
- $F$: Faraday constant ($96485$ Coulomb/mol).

In porous regions, the effective thermal conductivity is given by

$$k_{\text{eff}} = \varepsilon\alpha_l k_l + \varepsilon\alpha_g k_g + (1-\varepsilon)k_s \tag{2.28}$$

where $k_l$, $k_g$, $k_s$ denote the thermal conductivities of the liquid, gas, and solid phases.

### 2.2.5 Electrochemistry

The membrane proton domain is electrochemically active and consists of an ion/proton conducting electrolyte/membrane sandwiched between two adjacent active layers. Oxidation and reduction reactions occur at the anode and cathode electronic domains, respectively. The relationship between the electronic and ionic (protonic) potentials is governed by electrochemical kinetic models such as the Butler–Volmer [3] or Tafel [13] equations. For

instance, at the cathode electronic domain (with similar formulas applicable at the anode electronic domain), the current density can be written as

$$j_{ae} = i_{ae,0}(1-\alpha_l)^{\gamma} \prod_i \left(\frac{C_i}{C_{\text{ref}}}\right)^{\xi} \left[\exp\left(-\frac{\alpha_{ae} z F \eta_{ae}}{R_g T}\right) - \exp\left(\frac{(1-\alpha_{ae}) z F \eta_{ae}}{R_g T}\right)\right] \tag{2.29}$$

or, equivalently,

$$j_{ae} = i_{ae,0}(1-\alpha_l)^{\gamma} \left[\prod_{\text{reac},i} \left(\frac{C_i}{C_{\text{ref}}}\right)^{\xi} \exp\left(-\frac{\alpha_{ae} z F \eta_{ae}}{R_g T}\right) - \prod_{\text{prod},i} \left(\frac{C_i}{C_{\text{ref}}}\right)^{\xi} \exp\left(\frac{(1-\alpha_{ae}) z F \eta_{ae}}{R_g T}\right)\right] \tag{2.30}$$

- $i_0$ is the reference current density
- $z$ is the number of electrons transferred
- $F$ is the Faraday's constant
- $C_i$ is the concentration of species $i$
- $C_{\text{ref}}$ is the corresponding reference concentration (typically the inlet concentration)
- $\alpha_{ae}$ is the charge transfer coefficient
- $\beta$ is the power-law exponent
- $\gamma$ is the reaction order
- $\eta_{ae}$ is the activation overpotential, given by:

$$\eta_{ae} = \Phi_E - \Phi_I - E_{\text{Nernst},ae} \tag{2.31}$$

where $E_{\text{Nernst},ae}$ denotes the Nernst potential, calculated as :

$$E_{\text{Nernst},ae} = \frac{1}{zF} \sum_i \left[-\left(H_i - T S_i\right) \omega - R_g T \, \omega \ln p_i\right] \tag{2.32}$$

where:

- $p_i$ is the partial pressure of species $i$
- $H_i$ is the enthalpy
- $S_i$ is the entropy, defined in Eq. 2.27

- $\omega$ is the stoichiometric coefficient (negative for consumption and positive for production) corresponding to the transfer of $z$ electrons.

Eq. (2.37) is adapted from [6].

| **Physics** | **Governing Equations** | **Domain** |
|---|---|---|
| Continuity | $\frac{\partial(\alpha_\phi \rho_\phi)}{\partial t} + \nabla \cdot (\alpha_\phi \rho_\phi \mathbf{v}_\phi) = R_\phi$ | Fluid(GCs, GDLs, CLs) |
| Momentum (Eulerian-Eulerian) | $\frac{\partial(\alpha_\phi \rho_\phi \mathbf{v}_\phi)}{\partial t} + \nabla \cdot (\alpha_\phi \rho_\phi \mathbf{v}_\phi \mathbf{v}_\phi) = -\alpha_\phi \nabla p + \alpha_\phi \rho_\phi \mathbf{g} + \mathbf{M}_\phi + \mathbf{S}_{\text{Darcy},\phi}$ | Fluid(GCs, GDLs, CLs) |
| Species transport | $\frac{\partial(\rho_g \alpha_g Y_i)}{\partial t} + \nabla \cdot (\rho_g \alpha_g \mathbf{v}_g Y_i) = \nabla \cdot (\rho_g \alpha_g D_i^{\text{eff}} \nabla Y_i) + \alpha_g R_i$ | Fluid(GCs, GDLs, CLs) |
| Charge conservation | $\nabla \cdot (\sigma_E \nabla \Phi_E) = J_E, \quad \nabla \cdot (\sigma_I \nabla \Phi_I) = J_I$ | Electric(Electronic,Proton) |
| Water transport (membrane) | $\frac{\rho_m}{EW}\frac{\partial \lambda}{\partial t} + \nabla \cdot \left(\frac{n_d \mathbf{i}_I}{F}\right) = \nabla \cdot \left(\frac{\rho_m}{EW} D_m^{\text{eff}} \nabla \lambda\right) + R_\lambda$ | Membrane |
| Energy equation | $\frac{\partial(\rho C_p T)}{\partial t} + \rho C_p \mathbf{v} \cdot \nabla T = \nabla \cdot (k_{\text{eff}} \nabla T) + Q$ | Global domain |
| Electrochemistry (Butler–Volmer) | $j = i_0 \prod_i \left(\frac{C_i}{C_{\text{ref}}}\right)^\xi \left[e^{-\frac{\alpha z F \eta}{RT}} - e^{\frac{(1-\alpha) z F \eta}{RT}}\right]$ | CLs |

Table 2.1: Summary of governing equations and their computational domains in the PEMFC model. It is important to distinguish the coupling between the different computational domains. The global, fluid and electric domains share the same source term structure, differing only in the corresponding stoichiometric coefficients. Furthermore, the global and fluid domains share also the same phase velocity, $\mathbf{v}_\phi$.

## 2.3 Boundary Conditions

Appropriate boundary conditions are imposed in each computational domain in order to accurately represent the physical operation of the PEMFC.

### 2.3.1 Fluid Domain

For the fluid-flow problem, Dirichlet boundary conditions are imposed on the velocity field **v** at the GC inlets, where the inlet velocity is fixed. No-slip conditions are imposed at all solid walls, resulting in zero velocity at the corresponding boundaries. For the

pressure field $p$, a Dirichlet condition is applied at the outlet of the gas channels, while homogeneous Neumann conditions are imposed on all remaining boundaries.

The fluid-domain boundary is divided into three distinct patches, namely $S_I$, $S_W$, and $S_O$:

- $S_I$: Inlet boundaries of the gas channels (both anode and cathode). A fixed-value (Dirichlet) condition is imposed on the velocity field, while a zero Neumann condition is imposed on pressure.

- $S_W$: Solid-wall boundaries, including the interfaces between the BPs and the GCs, the lateral surfaces of the GDLs and CLs, as well as the membrane interfaces. A no-slip condition is imposed for velocity ($\mathbf{v} = 0$), while pressure satisfies a homogeneous Neumann condition.

- $S_O$: Outlet boundaries of the gas channels (both anode and cathode). A zero Neumann condition is imposed on the velocity, while the pressure is prescribed through a Dirichlet condition.

Table 2.2: Boundary conditions applied in the fluid domain.

| **Boundary Patch** | **Location** | **Velocity v** | **Pressure** $p$ |
|---|---|---|---|
| $S_I$ | GCs inlets | Dirichlet (fixed value) | Neumann $(\partial p/\partial n = 0)$ |
| $S_W$ | Solid walls/interfaces | No-slip $(\mathbf{v} = 0)$ | Neumann $(\partial p/\partial n = 0)$ |
| $S_O$ | GCs outlets | Neumann $(\partial \mathbf{v}/\partial n = 0)$ | Dirichlet (fixed value) |

### 2.3.2 Electric Domain

Dirichlet boundary conditions are imposed at the outer surfaces of the BPs in the electronic domains, prescribing the operating potential difference of the PEMFC. Zero Neumann boundary conditions are imposed at all remaining boundaries of the electronic domains, corresponding to zero normal current flux. For the proton-conducting domain, zero Neumann conditions are imposed over the entire boundary.

The boundary conditions corresponding to the electric formulation adopted in the present work are illustrated in Fig. 2.3.

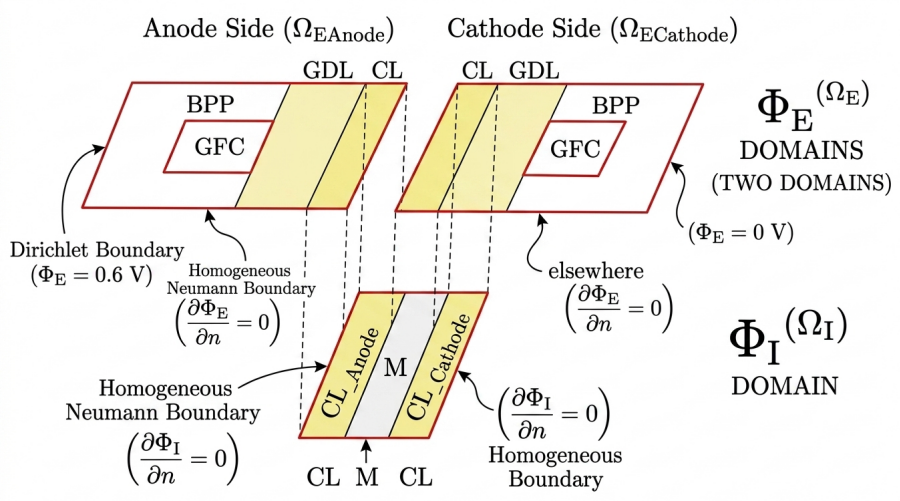


Figure 2.3: Boundary conditions imposed at the electric domain for the formulation (Method 1), illustrating Dirichlet (prescribed potential) and zero Neumann boundaries (zero normal current flux).

Table 2.3: Boundary conditions applied in the electric domain.

| Boundary Patch | Boundary Condition Type | Description |
|---|---|---|
| Anode Outer BP Patch | Dirichlet | Prescribed electric potential |
| Cathode Outer BP Patch | Dirichlet | Prescribed electric potential |
| Remaining electronic boundaries | Zero Neumann | Zero normal current flux |
| Proton domain | Zero Neumann | Zero normal proton flux |

### 2.3.3 Implementation of the Nernst Potential in the Electric Domain

Two different approaches have been employed for the incorporation of the Nernst potential in the PEMFC electric formulation [5]. These approaches differ in the definition of the imposed electric potentials at the BPs and, consequently, in the formulation of the activation overpotential within the CLs.

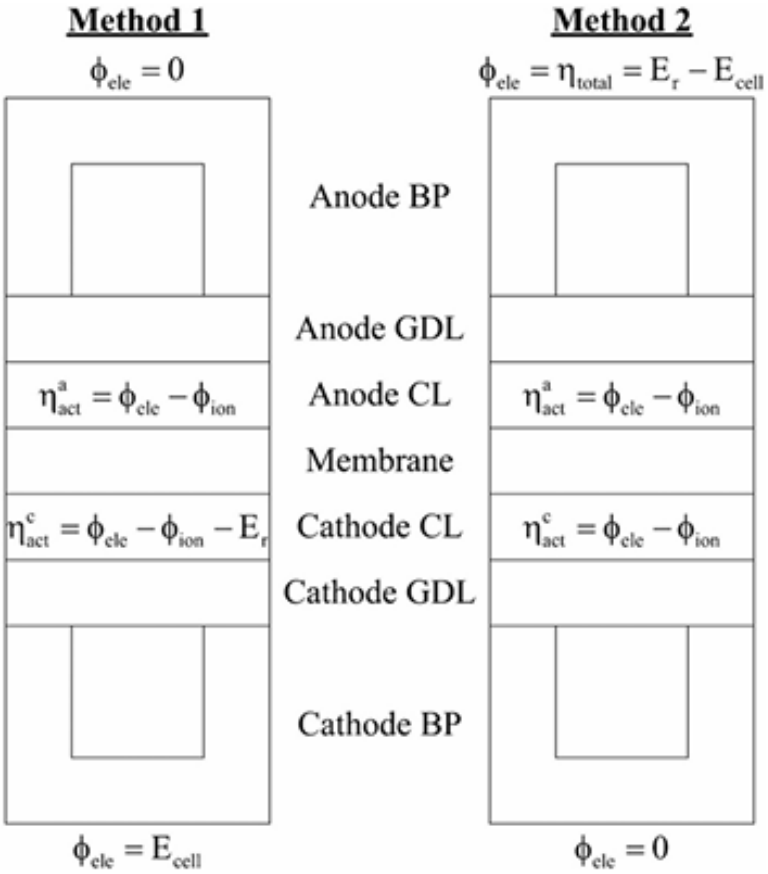


Figure 2.4: Comparison of the two approaches used for the implementation of the Nernst potential in the electric domain.

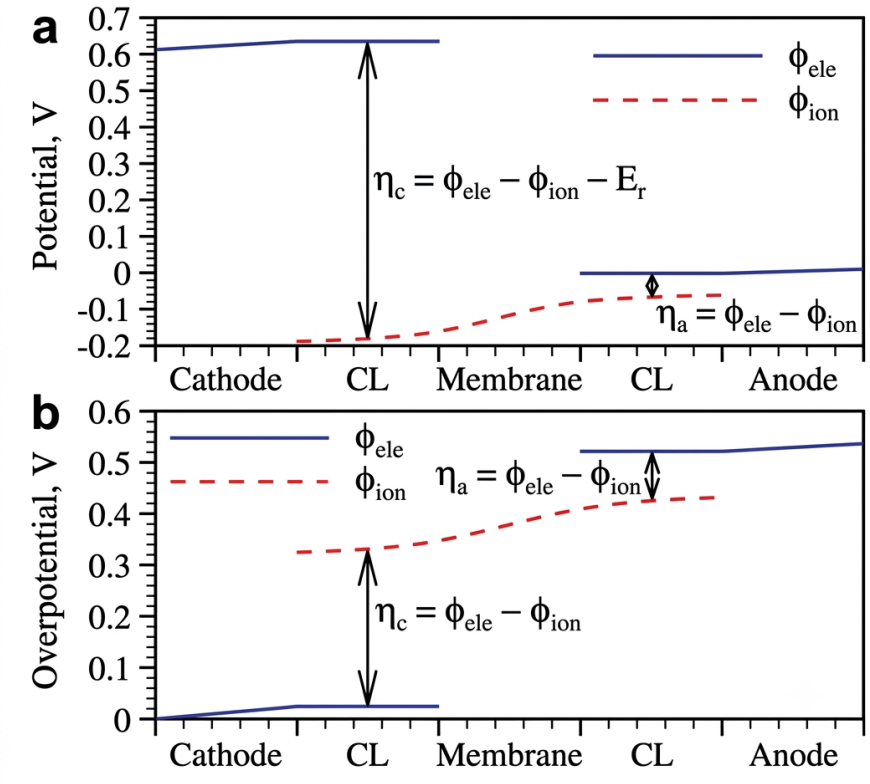


Figure 2.5: Indicative potential distribution across the PEMFC for Method 1 and 2. The reversible potential contribution appears explicitly in the cathode activation overpotential expression.

In **Method 1**, corresponding to the boundary conditions presented in Fig. 2.3, the electronic potential is prescribed directly through the applied cell voltage. The anode BP boundary face takes on the value

$$\phi_{\text{ele}} = 0,$$

while, at the cathode BP boundary face,

$$\phi_{\text{ele}} = E_{\text{cell}}.$$

Under this formulation, the activation overpotentials are expressed as

$$\eta^{a}_{\text{act}} = \phi_{\text{ele}} - \phi_{\text{ion}}$$

for the ACL, and

$$\eta^{c}_{\text{act}} = \phi_{\text{ele}} - \phi_{\text{ion}} - E_r$$

for the CCL, where $E_r$ denotes the reversible (Nernst) potential.

In **Method 2**, the reversible potential is incorporated directly into the imposed boundary conditions of the electronic phase. In this case, the CBP boundary face potential is, similarly to Method 1, set to

$$\phi_{\text{ele}} = 0,$$

while the ABP boundary face potential is prescribed as

$$\phi_{\text{ele}} = E_r - E_{\text{cell}}.$$

As a result, the activation overpotential in both CLs can be written in the unified form

$$\eta_{\text{act}}^{a,c} = \phi_{\text{ele}} - \phi_{\text{ion}},$$

without explicitly introducing the reversible potential term in the source expressions.

The corresponding distributions of the electronic and ionic potentials across the membrane-electrode assembly are illustrated in Fig. 2.5 for Methods 1 and 2. Although the two formulations differ mathematically, they are physically equivalent and yield the same electrochemical behavior and total cell voltage. Both methods will be presented and implemented in the following chapters.

## 2.4 Software and Comparison with Previous Work at PCOpt NTUA

The detailed software architecture and implementation of the primal solver are beyond the scope of the present study. Nevertheless, the implementation of the adjoint methodology required an extensive understanding of the existing source code, together with the modification and extension of several software components. Readers interested in the implementation details of the original numerical framework are referred to the *openFuelCell2* repository, where the software architecture is comprehensively documented [22].

Among the previous research efforts conducted at the Parallel CFD & Optimization (PCOpt) Unit of the National Technical University of Athens (NTUA), the work presented in [10, 7] is particularly relevant to the present study. The same computational domain and geometric configuration are adopted, thereby allowing a direct comparison between the numerical formulations. The principal difference lies in the treatment of the multiphase flow within the porous media. In [10], a mixture model was employed, in which the gas and liquid phases are represented as a single effective continuum governed by a common set of mass and momentum conservation equations. In contrast, the present work adopts a two-fluid Eulerian–Eulerian formulation. This formulation provides a more detailed representation of liquid water transport and its interaction with the gaseous phase, allowing

water accumulation and flooding phenomena to be captured more realistically.

The electrochemical performance, predicted by both numerical formulations, is compared through the polarization curves shown in Fig. 2.6. The figure also includes the experimental measurements reported in [21], which were originally used to validate the mixture-model formulation. Both numerical models reproduce the characteristic nonlinear behavior of the polarization curve and exhibit good agreement with the experimental measurements over the entire operating range. The mixture model provides a slightly closer agreement with the experimental data, particularly at intermediate and high current densities. The two-fluid Eulerian–Eulerian model consistently predicts lower current densities for the same cell voltage, with the discrepancy becoming more pronounced as the operating voltage decreases. Despite these differences, the overall agreement between the two numerical approaches confirms that the implementation of the two-fluid model produces physically realistic predictions while providing a more detailed representation of multi-phase transport phenomena.

The principal physical and electrochemical parameters employed in the two-fluid model are summarized in Table 2.4. These parameters include electrochemical reaction constants, transport properties, porous-medium characteristics, and dissolved-water transport coefficients adopted in the present implementation.

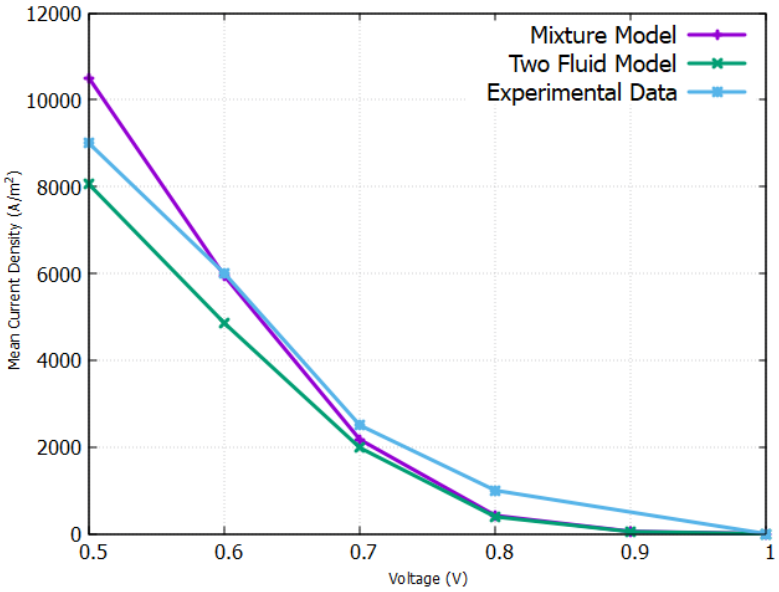


Figure 2.6: Comparison of the polarization curves predicted by the mixture model [10], the experimental measurements reported in [21], and the present two-fluid Eulerian–Eulerian model.

| Parameter Description | Symbol | Anode Side | Cathode Side | Unit |
|---|---|---|---|---|
| Exponential coefficient | $\xi$ | 1.2 | 2 | – |
| Reference molar concentration | $C^{ref}$ | 56.4 | 3.39 | $\mathrm{mol/m^3}$ |
| Exchange current density | $j_0$ | $1.0 \times 10^4$ | 120 | $\mathrm{A/m^3}$ |
| Charge transfer coefficient | $\alpha$ | 0.5 | 0.5 | – |
| Bruggeman exponent parameter | $\gamma$ | 1.5 | 1.5 | – |
| Reference pressure (Nernst model) | $p_{ref}$ | 101325 | 101325 | Pa |
| Diffusivity coefficient (GDL and CL) | $D_0$ | $11 \times 10^{-5}$ | $3.2 \times 10^{-5}$ | $\mathrm{m^2/s}$ |
| GDL porosity | $\varepsilon_{\mathrm{GDL}}$ | 0.5 | 0.5 | – |
| CL porosity | $\varepsilon_{\mathrm{CL}}$ | 0.5 | 0.5 | – |
| GDL and CL Darcy resistance coefficient | $d_{\mathrm{GDL-CL}}$ | $1.0 \times 10^{12}$ | $1.0 \times 10^{12}$ | $\mathrm{m^{-2}}$ |
| GDL and CL specific heat capacity | $C_{p,\mathrm{GDL-CL}}$ | 2062.74 | 1108.85 | $\mathrm{J/(kg \cdot K)}$ |
| GDL and CL thermal conductivity | $k_{\mathrm{GDL-CL}}$ | 0.08396 | 0.02867 | $\mathrm{W/(m \cdot K)}$ |
| Gas phase Schmidt number | $Sc$ | 0.7 | – | – |
| Electro-osmotic drag coefficient | $n_d$ | 0.12 | 0.12 | – |
| Ionomer density/equivalent weight | $\rho/\mathrm{EW}$ | 1964 | 1964 | $\mathrm{mol/m^3}$ |
| Water adsorption/desorption coefficient | $\xi_{\mathrm{ads}}$ | 1.3 | 1.3 | – |
| Constant liquid water pore/droplet diameter | $d_{\mathrm{water}}$ | $1.5 \times 10^{-4}$ | $1.5 \times 10^{-4}$ | m |
| Molar weight ($H_2O$) | $M_{\mathrm{H_2O}}$ | 18.0153 | 18.0153 | g/mol |
| Molar weight ($H_2$) | $M_{\mathrm{H_2}}$ | 2.01594 | – | g/mol |
| Molar weight ($O_2$) | – | – | 31.9988 | g/mol |

Table 2.4: Baseline physical, structural, electrochemical, and dissolved-water transport parameters used in the Eulerian-Eulerian Model.

# Chapter 3

# Electric Adjoint Model Development

## 3.1 Assumptions

The adjoint method is developed and assessed incrementally. So, the first approach adopted for the adjoint implementation is restricted to the electric domain, while the remaining fields of the fluid and global domains are considered frozen. This assumption is motivated by the nature of the objective function, which is directly related to the current density. As will be demonstrated in the following sections, the highest sensitivity with respect to (w.r.t.) the design variable is obtained within the electric domain. Consequently, the electric potential field, $\Phi$, is the only physical quantity differentiated w.r.t. the design variable which will be the porosity value $\varepsilon$ of each region.

The analysis is conducted under potentiostatic operating conditions, meaning that the cell voltage is prescribed while the resulting current density is computed as part of the solution procedure.

All remaining physical fields, including temperature, membrane water content, species mass fractions, velocity, and pressure, are assumed to be known and independent of the design variable. Accordingly, the continuous adjoint formulation is derived exclusively from the governing equation of charge conservation.

## 3.2 Objective Function

The objective of the optimization process is to maximize the total current density within a selected CL—specifically, either the ACL or the CCL—under a specified steady-state voltage constraint. As demonstrated in subsequent sections, the choice of the target CL does not affect the optimization results, as the derived adjoint derivatives remain mathematically independent of this selection. The objective function is therefore defined as the volume integral of the absolute value of the volumetric current source term within the catalyst

layer:

$$F = \int_{\Omega_{CL}} |J| \, d\Omega \tag{3.1}$$

where $\Omega_{CL}$ denotes the volume of the selected catalyst layer.

To incorporate the governing equation as constraint, an augmented functional is defined as:

$$F_{\text{aug}} = F + \int_{\Omega} \phi R^{\Phi} \, d\Omega \tag{3.2}$$

where $\phi$ is the adjoint variable associated with charge conservation.

The residual of the governing equation is given by:

$$R^{\Phi} = \frac{\partial}{\partial x_j} \left( \sigma_k \frac{\partial \Phi_k}{\partial x_j} \right) - J_k = 0 \tag{3.3}$$

Index $k \in \{E, I\}$ denotes the electronic and proton regions, respectively.

## 3.3 Design Variables

The design variables correspond to the porosity value of each porous region of the fuel cell:

$$b_n, \quad n = 1, \ldots, 6 \tag{3.4}$$

Specifically, these correspond to:

$$b_1 = \varepsilon_{\text{AGDL}},\ b_2 = \varepsilon_{\text{AMPL}},\ b_3 = \varepsilon_{\text{ACL}},\ b_4 = \varepsilon_{\text{CGDL}},\ b_5 = \varepsilon_{\text{CMPL}},\ b_6 = \varepsilon_{\text{CCL}}$$

The optimization loop utilizes these six porosity values as design variables to maximize the objective function, which corresponds to achieving the peak total current density. The microporous layer (MPL) regions, situated between the GDL and the CL, are incorporated to introduce an additional degree of freedom, thereby ensuring a smoother transition for the design variables during the optimization process. The treatment of MPLs is identical to GDLs.

## 3.4 Electric Domain

### 3.4.1 Electronic and Proton Charge Conservation

Eqs. 2.19 and 2.20 can be expressed in indicial notation using the Einstein summation convention as follows:

$$\frac{\partial}{\partial x_j}\left(\sigma_E \frac{\partial \Phi_E}{\partial x_j}\right) = J_E \tag{3.5}$$

$$\frac{\partial}{\partial x_j}\left(\sigma_I \frac{\partial \Phi_I}{\partial x_j}\right) = J_I \tag{3.6}$$

The source terms are non-zero only within the CLs, where electrochemical reactions occur.

#### Differentiation of the Objective Function

As discussed previously, the optimization objective is defined so as to maximize the current density generated within one of the catalyst layers, namely either ACL or CCL.

Let $J$ denote the volumetric current source term obtained from the governing electrochemical equations. The objective functional is constructed through integration over the relevant catalyst-layer subdomains. For a selected catalyst layer $\Omega_{\text{CL}}$, the total objective can be written as

$$\mathcal{F} = \int_{\Omega_{\text{CL}}^{\text{el}}} |J| \, d\Omega. \tag{3.7}$$

However, the sign convention of the electronic current source differs between anode and cathode regions. In particular:

- within the anode electronic region, $J > 0$,
- within the cathode electronic region, $J < 0$.

Accordingly, for the electronic conducting phase, the objective functional is defined differently for the anode and cathode cases.

**Anode Catalyst Layer (ACL)** Since $J > 0$ in the electronic region of the anode, maximizing the current magnitude is equivalent to maximizing $J$:

$$\mathcal{F}_{\text{ACL}}^{\text{el}} = \int_{\Omega_{\text{ACL}}^{\text{el}}} J \, d\Omega. \tag{3.8}$$

**Cathode Catalyst Layer (CCL)** Since $J < 0$ in the electronic region of the cathode, maximizing the current magnitude is equivalent to maximizing $-J$:

$$\mathcal{F}_{\text{CCL}}^{\text{el}} = \int_{\Omega_{\text{CCL}}^{\text{el}}} (-J)\, d\Omega. \tag{3.9}$$

The volumetric source terms in the conservation equations for electronic and ionic charges (Eqs. 2.19–2.20) are governed by the Butler–Volmer macroscopic kinetic relation (Eq. 2.30).

Let $j_{ae}$ and $j_{fe}$ represent the absolute localized current densities generated within the anode and cathode catalyst layers, respectively (Eqs. 2.22–2.21). The signs of these source terms are mapped dynamically to the electronic and ionic phase conservation equations based on the charge-transfer mechanisms described in Section 2.2.3. Under these conventions, the source terms are expressed as functions of the local overpotential:

$$j_{ae} = C_1 \left( e^{A_1 \Delta\Phi} - e^{-A_2 \Delta\Phi} \right) \tag{3.10}$$

$$j_{fe} = C_2 \left( e^{-B_1 \Delta\Phi} - e^{B_2 \Delta\Phi} \right) \tag{3.11}$$

$\Delta\Phi$ denotes the local activation overpotential, defined as the potential difference between the primal electronic ($\Phi_E$) and ionic ($\Phi_I$) phases:

$$\Delta\Phi = \Phi_E - \Phi_I \tag{3.12}$$

To implement the adjoint sensitivity analysis, the variation of these transcendental source terms must be derived w.r.t. the design variable vector $\mathbf{b}$. Defining the variational operator as $\delta = \frac{\partial}{\partial b_n}$, the differentiation of a general exponential component via the chain rule yields:

$$\delta \left( e^{\Gamma \Delta\Phi} \right) = \delta \left( e^{\Gamma (\Phi_E - \Phi_I)} \right) = e^{\Gamma \Delta\Phi} \Gamma \left( \delta\Phi_E - \delta\Phi_I \right) \tag{3.13}$$

where $\Gamma$ represents an arbitrary kinetic scaling exponent (e.g., $A_1, -A_2, -B_1, B_2$). This form effectively decouples the sensitivity of the electrochemical reactions into variations of the primal state fields, $\delta\Phi_E$ and $\delta\Phi_I$.

$$\delta j_{ae} = C_1 e^{A_1 \Delta\Phi} A_1 (\delta\Phi_E - \delta\Phi_I) - C_1 e^{A_2 \Delta\Phi} A_2 (\delta\Phi_E - \delta\Phi_I) \tag{3.14}$$

$$\delta j_{fe} = -C_2 e^{B_1 \Delta\Phi} B_1 (\delta\Phi_E - \delta\Phi_I) + C_2 e^{B_2 \Delta\Phi} B_2 (\delta\Phi_E - \delta\Phi_I) \tag{3.15}$$

$$\delta j_{ae} = C_1 [A_1 e^{A_1 \Delta\Phi} - A_2 e^{A_2 \Delta\Phi}] \delta\Phi_E + [C_1 A_2 e^{A_2 \Delta\Phi} - A_1 e^{A_1 \Delta\Phi}] \delta\Phi_I \tag{3.16}$$

$$\delta j_{fe} = C_2[B_2 e^{B_2 \Delta\Phi} - B_1 e^{B_1 \Delta\Phi}]\delta\Phi_E + C_2[B_1 e^{B_1 \Delta\Phi} - B_2 e^{B_2 \Delta\Phi}]\delta\Phi_I \tag{3.17}$$

Or :

$$\delta j_{ae} = C_A \delta\Phi_E - C_A \delta\Phi_I \tag{3.18}$$

$$\delta j_{fe} = -C_C \delta\Phi_e + C_C \delta\Phi_I \tag{3.19}$$

where:

$$C_A = C_1[A_1 e^{A_1 \Delta\Phi} - A_2 e^{A_2 \Delta\Phi}] \tag{3.20}$$

$$C_C = C_2[B_1 e^{B_1 \Delta\Phi} - B_2 e^{B_2 \Delta\Phi}] \tag{3.21}$$

and :

$$C_1 = (1-s) J_o^r [\frac{C_{H_2}}{C_{H_2 ref}}]^{0.5} \tag{3.22}$$

$$C_2 = (1-s) J_o^r [\frac{C_{O_2}}{C_{O_2 ref}}]^{0.5} \tag{3.23}$$

So, from the objective function:

$$F = \int_{\Omega_k} j_k d\Omega \tag{3.24}$$

$$\delta F = \int_{\Omega_k} C_k \delta\Phi_E d\Omega - \int_{\Omega_k} C_k \delta\Phi_I d\Omega \tag{3.25}$$

where index k stands for A for the ACL or C for the CCL.

**Differentiation of the Laplacian Term**

To evaluate the sensitivity of the governing equations w.r.t. the design variables, the variation of the Laplacian term must be derived. Applying the principles of calculus of variations, integration by parts, and the divergence theorem, the variation of the diffusion term is expressed as:

$$\begin{aligned}\delta \int_\Omega \phi_k \frac{\partial}{\partial x_j}\left(\sigma_k \frac{\partial \Phi_k}{\partial x_j}\right) d\Omega = &\int_S \phi_k \delta\left(\sigma_k \frac{\partial \Phi_k}{\partial x_j}\right) n_j dS \\ &- \int_\Omega \frac{\partial \phi_k}{\partial x_j}\frac{\partial \Phi_k}{\partial x_j}\delta\sigma_k d\Omega - \int_S \frac{\partial \phi_k}{\partial x_j}\sigma_k \delta\Phi_k n_j dS + \int_\Omega \frac{\partial^2 \phi_k}{\partial x_j^2}\sigma_k \delta\Phi_k d\Omega\end{aligned} \tag{3.26}$$

**Differentiation of the Non-Linear Source Term**

The non-linear source term can be analyzed in the two CL zones respectively:

For the anode electronic domain $J_E = j_{ae}$:

$$\int_{\Omega_{ACL}} \phi_E \delta J_E d\Omega = \int_{\Omega_{ACL}} \phi_E \delta j_{ae} d\Omega = \int_{\Omega_{ACL}} \phi_E [C_A \delta\Phi_E - C_A \delta\Phi_I] d\Omega \tag{3.27}$$

For the cathode electronic domain, $J_E = -j_{fe}$:

$$\int_{\Omega_{CCL}} \phi_E \delta J_E d\Omega = -\int_{\Omega_{CCL}} \phi_E \delta j_{fe} d\Omega = \int_{\Omega_{CCL}} \phi_E [C_C \delta\Phi_E - C_C \delta\Phi_I] d\Omega \tag{3.28}$$

For the anode proton domain, $J_I = -j_{ae}$:

$$\int_{\Omega_{ACL}} \phi_I \delta J_I d\Omega = -\int_{\Omega_{ACL}} \phi_I \delta j_{ae} d\Omega = \int_{\Omega_{ACL}} \phi_I [C_A \delta\Phi_I - C_A \delta\Phi_E] d\Omega \tag{3.29}$$

For the cathode proton domain, $J_I = j_{fe}$:

$$\int_{\Omega_{CCL}} \phi_I \delta J_I d\Omega = -\int_{\Omega_{CCL}} \phi_I \delta j_{fe} d\Omega = \int_{\Omega_{CCL}} \phi_I [C_C \delta\Phi_I - C_C \delta\Phi_E] d\Omega \tag{3.30}$$

So, the final expressions of the source terms at the CLs that correspond to : $-\phi_E \delta J_E - \phi_I \delta J_I$

.

For the $\phi_E$-FAE eq in ACL(coefficient of $\delta\Phi_E$): $-C_A\phi_E + C_A\phi_I$
For the $\phi_E$-FAE eq in CCL(coefficient of $\delta\Phi_E$): $-C_C\phi_E + C_C\phi_I$
For the $\phi_I$-FAE eq in CCL(coefficient of $\delta\Phi_I$): $C_A\phi_E - C_A\phi_I$
For the $\phi_I$-FAE eq in CCL(coefficient of $\delta\Phi_I$): $C_C\phi_E - C_C\phi_I$

### 3.4.2 Porosity-dependent effective conductivities

The effective electronic and proton conductivities $\sigma$ in the porous media are modeled as functions of the local porosity $\varepsilon$, depending on the material region. This formulation accounts for the reduction in available conductive pathways due to the presence of void space.

**Electronic conductivity** According to Eq. 2.23, its sensitivity with respect to porosity is given by:

$$\frac{d\sigma_E}{d\varepsilon} = \begin{cases} 0, & \text{for the BPs} \\ -\sigma_0, & \text{for the GDLs and CLs} \end{cases} \tag{3.31}$$

**Proton conductivity** The corresponding derivative w.r.t. porosity, according to Eq. 2.24, is:

$$\frac{d\sigma_I}{d\varepsilon} = \begin{cases} 0, & \text{for the membrane} \\ -1.5\,\sigma_0\,\mathrm{por}_{\mathrm{Naf}}^{1.5}(1-\varepsilon)^{0.5}, & \text{for the CLs} \end{cases} \tag{3.32}$$

These expressions are used in the adjoint-based sensitivity analysis, where variations in the porosity field directly influence the effective transport properties of both electronic and proton phases.

## 3.5 Derivative of the Augmented Objective Function

By combinig all the derived terms, the variation $\delta F_{Aug}$ is obtained:

$$\begin{aligned} \delta F_{Aug} = &\int_\Omega \left( \frac{\partial}{\partial x_j}\left(\sigma_k \frac{\partial \Phi_k}{\partial x_j}\right) + C_t - \Phi_k \delta J_k \right) \delta\Phi_k \, d\Omega \\ &- \int_S \phi_k n_j \delta\left(\sigma_k \frac{\partial \Phi_k}{\partial x_j}\right) dS - \int_S \frac{\partial \phi_k}{\partial x_j} \sigma_k n_j \delta\Phi_k \, dS - \int_\Omega \frac{\partial \phi_k}{\partial x_j}\frac{\partial \Phi_k}{\partial x_j}\delta\sigma_k \, d\Omega \end{aligned} \tag{3.33}$$

where the index $k \in \{\mathrm{E}, \mathrm{I}\}$ denotes the electronic and proton domains and the index $t \in \{\mathrm{A}, \mathrm{C}\}$ denotes the anode or cathode domain, depending on the CL the objective function is applied to.

## 3.6 Field Adjoint Equations

To eliminate the dependency of the total derivative on primal field variations, the coefficients corresponding to $\delta\Phi_E$ and $\delta\Phi_I$ in the first term of Eq. 3.33 are set to zero. Vanishing these coefficients yields the system of partial differential equations that define the field adjoint problem.

For the electronic domain:

$$\frac{\partial}{\partial x_j}(\sigma_E \frac{\phi_E}{\partial x_j}) + C_k - \phi_E \delta J_E - \phi_I \delta J_I = 0 \tag{3.34}$$

For the proton domain:

$$\frac{\partial}{\partial x_j}(\sigma_I \frac{\phi_I}{\partial x_j}) + C_k - \phi_I \delta J_I - \phi_E \delta J_E = 0 \tag{3.35}$$

## 3.7 Adjoint Boundary Conditions

The adjoint boundary conditions are derived from setting the surface integrals that arise after applying the Green-Gauss Theorem to the variation of the augmented functional to zero.

From the variational formulation of $F_{Aug}$, Eq. 3.2, the boundary integrals associated with the electronic domain are:

$$\int_{S_E} \phi_E \, \sigma_E \, \delta\left(\frac{\partial \Phi_E}{\partial n}\right) dS - \int_{S_E} \frac{\partial \phi_E}{\partial n} \sigma_E \, \delta\Phi_E \, dS \tag{3.36}$$

Similarly, for the proton domain:

$$\int_{S_I} \phi_I \, \sigma_I \, \delta\left(\frac{\partial \Phi_I}{\partial n}\right) dS - \int_{S_I} \frac{\partial \phi_I}{\partial n} \sigma_I \, \delta\Phi_I \, dS \tag{3.37}$$

**Dirichlet Boundary (Prescribed Potential)** If the electric potential is prescribed:

$$\Phi_i = \bar{\Phi}_i \tag{3.38}$$

then:

$$\delta\Phi_i = 0 \tag{3.39}$$

and the remaining boundary term vanishes if:

$$\phi_i = 0 \tag{3.40}$$

Thus, along the Dirichlet boundaries of the primal problem:

$$\phi_i = 0 \tag{3.41}$$

**Neumann Boundary (Prescribed Current Flux)** If the current flux is prescribed:

$$\sigma_i \frac{\partial \Phi_i}{\partial n} = \bar{q}_i \tag{3.42}$$

then:

$$\delta\left(\frac{\partial \Phi_i}{\partial n}\right) = 0 \tag{3.43}$$

and the adjoint boundary condition becomes:

$$\sigma_i \frac{\partial \phi_i}{\partial n} = 0 \tag{3.44}$$

Thus, along the Neumann boundaries of the primal problem:

$$\sigma_i \frac{\partial \phi_i}{\partial n} = 0 \tag{3.45}$$

**Summary of Adjoint Boundary Conditions**

For both electronic and ionic domains:

- Along the Dirichlet boundaries of the primal problem (i.e., the two vertical patches shown in Fig. 2.3):

$$\phi = 0$$

- Along the Neumann boundaries of the primal problem (i.e., all remaining patches of the electronic domain and the entire boundary of the ionic domain):

$$\sigma \frac{\partial \phi}{\partial n} = 0$$

## 3.8 Sensitivity Derivatives

The sensitivity of the objective function w.r.t. each design variable is obtained. The resulting gradients provide the necessary information for gradient-based optimization of the porous structure.

$$\frac{\delta F}{\delta b_{\text{ACL}}} = -\int_{\Omega_{\text{ACL}}} \frac{\partial \phi_E}{\partial x_j} \frac{\partial \Phi_E}{\partial x_j} \frac{\delta \sigma_E}{\delta b_{\text{ACL}}} \, d\Omega_{\text{ACL}} - \int_{\Omega_{\text{ACL}}} \frac{\partial \phi_I}{\partial x_j} \frac{\partial \Phi_I}{\partial x_j} \frac{\delta \sigma_I}{\delta b_{\text{ACL}}} \, d\Omega_{\text{ACL}} \tag{3.46}$$

$$\frac{\delta F}{\delta b_{\text{AMPL}}} = -\int_{\Omega_{\text{AMPL}}} \frac{\partial \phi_E}{\partial x_j} \frac{\partial \Phi_E}{\partial x_j} \frac{\delta \sigma_E}{\delta b_{\text{AMPL}}} \, d\Omega_{\text{AMPL}} \tag{3.47}$$

$$\frac{\delta F}{\delta b_{\text{AGDL}}} = -\int_{\Omega_{\text{AGDL}}} \frac{\partial \phi_E}{\partial x_j} \frac{\partial \Phi_E}{\partial x_j} \frac{\delta \sigma_E}{\delta b_{\text{AGDL}}} \, d\Omega_{\text{AGDL}} \tag{3.48}$$

$$\frac{\delta F}{\delta b_{\text{CCL}}} = -\int_{\Omega_{\text{CCL}}} \frac{\partial \phi_E}{\partial x_j} \frac{\partial \Phi_E}{\partial x_j} \frac{\delta \sigma_E}{\delta b_{\text{CCL}}} \, d\Omega_{\text{CCL}} - \int_{\Omega_{\text{CCL}}} \frac{\partial \phi_I}{\partial x_j} \frac{\partial \Phi_I}{\partial x_j} \frac{\delta \sigma_I}{\delta b_{\text{CCL}}} \, d\Omega_{\text{CCL}} \tag{3.49}$$

$$\frac{\delta F}{\delta b_{\text{CMPL}}} = -\int_{\Omega_{\text{CMPL}}} \frac{\partial \phi_E}{\partial x_j} \frac{\partial \Phi_E}{\partial x_j} \frac{\delta \sigma_E}{\delta b_{\text{CMPL}}} \, d\Omega_{\text{CMPL}} \tag{3.50}$$

$$\frac{\delta F}{\delta b_{\text{CGDL}}} = -\int_{\Omega_{\text{CGDL}}} \frac{\partial \phi_E}{\partial x_j} \frac{\partial \Phi_E}{\partial x_j} \frac{\delta \sigma_E}{\delta b_{\text{CGDL}}} \, d\Omega_{\text{CGDL}} \tag{3.51}$$

where each design variable $b_*$ corresponds to the porosity value of each specific region, namely the ACL, AMPL, AGDL, CGDL, CCL, and CMPL regions.

## 3.9 Simulation Results

### 3.9.1 Geometry of the model

The geometry of the PEMFC contains the BPs, the GCs.the porous zones and the membrane. The channel length is 30 mm.

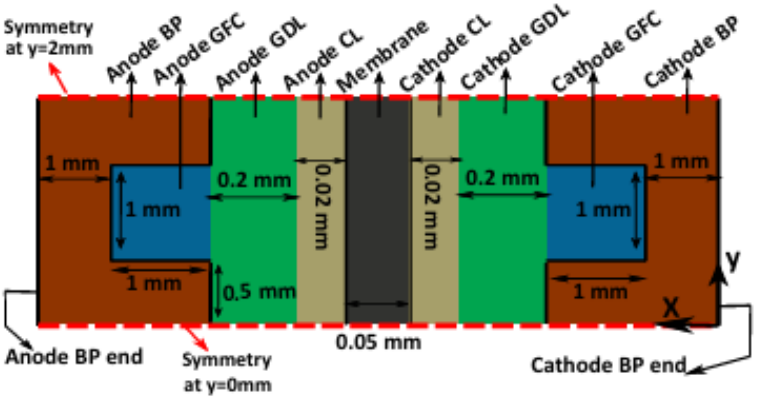


Figure 3.1: 2D schematic of the PEMFC (not to scale), with dimensions.

### 3.9.2 Mesh Statistics

Two different structured, hexagonal, orthogonal 3D meshes were generated using `blockMesh`.

Fine mesh represents the simplified layered configuration with the following characteristics shown in Tab. 3.1.

Coarse mesh represents the coarse configuration with significantly reduced computational cost. It contains approximately 19% of the cells of the fine mesh (189,720 vs 999,648) while maintaining identical geometry and mesh quality (max aspect ratio 400, perfect orthogonality). The characteristics are shown in Tab. 3.2.

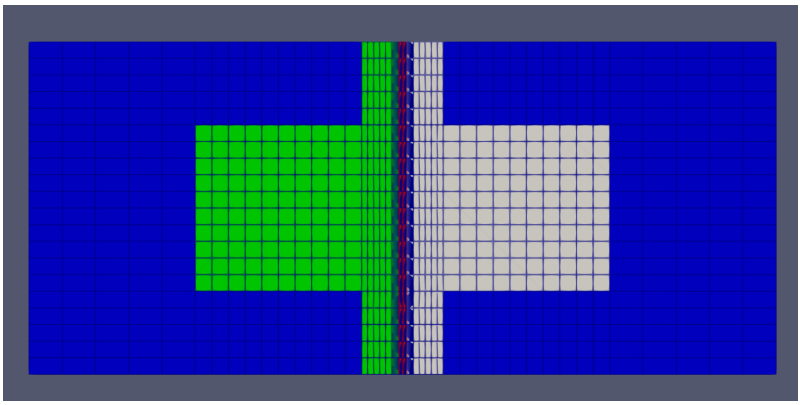

Figure 3.2: Computational mesh, each region shown with different color.

| CellZone | Cells | Avg. Volume (m³) | Total Volume (m³) |
|---|---|---|---|
| BPs | 308,672 | $5.83 \times 10^{-13}$ | $1.8 \times 10^{-7}$ |
| CGC | 70,304 | $4.27 \times 10^{-13}$ | $3.0 \times 10^{-8}$ |
| CGDL | 78,624 | $1.53 \times 10^{-13}$ | $1.2 \times 10^{-8}$ |
| CMPL | 78,624 | $7.63 \times 10^{-15}$ | $6.0 \times 10^{-10}$ |
| CCL | 78,624 | $7.63 \times 10^{-15}$ | $6.0 \times 10^{-10}$ |
| Membrane | 78,624 | $3.82 \times 10^{-14}$ | $3.0 \times 10^{-9}$ |
| ACL | 78,624 | $7.63 \times 10^{-15}$ | $6.0 \times 10^{-10}$ |
| AMPL | 78,624 | $7.63 \times 10^{-15}$ | $6.0 \times 10^{-10}$ |
| AGDL | 78,624 | $1.53 \times 10^{-13}$ | $1.2 \times 10^{-8}$ |
| AGC | 70,304 | $4.27 \times 10^{-13}$ | $3.0 \times 10^{-8}$ |

Table 3.1: Cell zone statistics for Fine mesh (average volume = total volume / cells).

### 3.9.3 Verification of the Anode Electric Potential Adjoint Model

In this section, the adjoint formulation is verified for the anode electric potential domain. For this purpose, only the electric potential $\phi_E$ is solved as a primal variable only in anode electronic domain. This approach allows an isolated verification of the adjoint implementation associated with the electric potential equation.

#### Model Parameters

The parameters of the Butler–Volmer model used in this verification study are summarized in Tab. 3.3.

The electric conductivity values employed in both electrodes are listed in Tab. 3.4.

The temperature is assumed constant at $T = 343.15$ K (70°C). Furthermore, Faraday's constant is taken as $F = 96485.33212$ C/mol and the universal gas constant as $R = 8.32$ J/(mol K). The porosity in all zones is initially set to $\varepsilon_0 = 0.5$.

| CellZone | Cells | Avg. Volume (m³) | Total Volume (m³) |
|---|---|---|---|
| BPS | 58,560 | $3.07 \times 10^{-12}$ | $1.8 \times 10^{-7}$ |
| CGC | 13,500 | $2.22 \times 10^{-12}$ | $3.0 \times 10^{-8}$ |
| CGDL | 14,880 | $8.06 \times 10^{-13}$ | $1.2 \times 10^{-8}$ |
| CMPL | 14,880 | $4.03 \times 10^{-14}$ | $6.0 \times 10^{-10}$ |
| CCL | 14,880 | $4.03 \times 10^{-14}$ | $6.0 \times 10^{-10}$ |
| Membrane | 14,880 | $2.02 \times 10^{-13}$ | $3.0 \times 10^{-9}$ |
| ACL | 14,880 | $4.03 \times 10^{-14}$ | $6.0 \times 10^{-10}$ |
| AMPL | 14,880 | $4.03 \times 10^{-14}$ | $6.0 \times 10^{-10}$ |
| AGDL | 14,880 | $8.06 \times 10^{-13}$ | $1.2 \times 10^{-8}$ |
| AGC | 13,500 | $2.22 \times 10^{-12}$ | $3.0 \times 10^{-8}$ |

Table 3.2: Cell zone statistics for Coarse mesh.

| Parameter | Unit | Value |
|---|---|---|
| $i_0$ (Anode) | $\mathrm{A\,m^{-3}}$ | 1000 |
| $i_0$ (Cathode) | $\mathrm{A\,m^{-3}}$ | 120 |
| $\alpha$ | – | 0.5 |
| $\left(\frac{C_i}{C_{\text{ref}}}\right)^{\xi}$ | – | 1 |

Table 3.3: Parameters of the Butler–Volmer model.

| Parameter | Unit | Value |
|---|---|---|
| $\sigma_0$ at BPs, CLs, GDLs | $\mathrm{S\,m^{-1}}$ | 750 |
| Porosity of Nafion (porNaf) | – | 0.3 |

Table 3.4: Steady-state electric conductivity parameters.

**Adjoint Verification Procedure**

To verify the correctness of the adjoint implementation, the adjoint derivative $dJ/db_{\text{ACL}}$ is compared with a finite-difference approximation. Only the porosity of the anode catalyst layer (ACL), $\varepsilon_{\text{ACL}}$, is perturbed, while all other regions remain fixed.

For perturbation $\Delta\varepsilon$, around the porosity value $\varepsilon_0$, the central finite-difference approximation is given by

$$\left.\frac{\partial F}{\partial \varepsilon_{\text{ACL}}}\right|_{\varepsilon_0} \approx \frac{F(\varepsilon_0 + \Delta\varepsilon) - F(\varepsilon_0 - \Delta\varepsilon)}{2\,\Delta\varepsilon}.$$

In contrast to the finite-difference approach, which requires two primal evaluations for each design variable, the adjoint method provides the sensitivity $dJ/db_{\text{ACL}}$ through a single adjoint solve, independent of the number of design parameters. This represents a significant computational advantage in large-scale optimization problems.

**Results and Discussion**

Tab. 3.5 summarizes the comparison between finite-difference and adjoint sensitivities for different mesh resolutions and discretization schemes (upwind, backward, and central).

| Mesh | $\Delta\epsilon$ | Scheme | Finite diff. $\partial F/db_{\text{ACL}}$ | Adjoint $\partial F/db_{\text{ACL}}$ | Deviation (%) |
|---|---|---|---|---|---|
| Fine | 0.01 | Upwind | -4.7032E-05 | -4.6715E-05 | 0.68 |
| | | Backward | -4.6987E-05 | -4.6712E-05 | 0.59 |
| | | Central | -4.7011E-05 | -4.6709E-05 | 0.65 |
| | 0.1 | Upwind | -5.0124E-05 | -4.6715E-05 | 7.29 |
| | | Backward | -4.5036E-05 | -4.6715E-05 | 3.59 |
| | | Central | -4.7028E-05 | -4.6715E-05 | 0.67 |
| Coarse | 0.01 | Upwind | -4.8126E-05 | -4.7523E-05 | 1.27 |
| | | Backward | -4.8054E-05 | -4.7519E-05 | 1.13 |
| | | Central | -4.7988E-05 | -4.7521E-05 | 0.98 |

Table 3.5: Comparison between finite-difference and adjoint sensitivities for perturbations of $\varepsilon_{\text{ACL}}$ ($\varepsilon_0 = 0.5$).

The results demonstrate excelent agreement between the adjoint sensitivities and the finite-differences approximations. For the smaller perturbation $\Delta\varepsilon = 0.01$, the deviation remains below approximately 1% for all discretization schemes and mesh resolutions. This confirms both the consistency of the adjoint formulation and its correct numerical implementation.

For the larger perturbation $\Delta\varepsilon = 0.1$, the relative deviation increases, particularly for the upwind scheme. This behavior was expected, since finite-difference approximations become less accurate for larger perturbations due to truncation errors and nonlinear effects. The central scheme shows the best agreement, which is consistent with its second-order accuracy.

Overall, the study verifies that the adjoint model correctly computes the derivative of the objective function w.r.t. ACL porosity. The observed mesh independence of the adjoint sensitivities further strengthens confidence in the robustness of the implementation.

**AGDL and AMPL Sensitivity Verification**

In addition to the ACL porosity perturbation test, further verification was performed for the derivatives associated with the AMPL and anode parameters. A central perturbation $\delta\varepsilon = 0.01$ around $\varepsilon_0 = 0.5$ was applied.

Tab. 3.6 summarizes the finite-difference sensitivities obtained using different schemes and compares them with the adjoint results.

The results show excellent agreement between the adjoint sensitivities and finite-differences. For the AMPL parameter, the relative error is below 1%, indicating an excellent consistency between both approaches.

| Scheme | $\partial F/\partial b_{\text{AMPL}}$ | $\partial F/\partial b_{\text{ANODE}}$ |
|---|---|---|
| Upwind | -7.3042E-05 | -1.9836E-03 |
| Central | -7.2988E-05 | -1.9467E-03 |
| Backward | -7.3051E-05 | -1.9134E-03 |
| Adjoint | -7.2526E-05 | -1.8429E-03 |
| Deviation (%) | 0.71 | 5.50 |

Table 3.6: Comparison between finite-difference and adjoint sensitivities for AMPL and anode derivatives on a mesh with $10^5$ cells.

For the anode derivative, the discrepancy is slightly larger (approximately 5%), which can be attributed to stronger nonlinearity of the sensitivity w.r.t. this parameter. Nevertheless, the magnitude and sign of the derivative are correctly reproduced by the adjoint method.

### 3.9.4 Verification of the Three-Electric Domain Model

This verification study focuses on the coupled three-domain formulation involving the electronic potentials at the anode ($\Phi_{e,A}$), cathode ($\Phi_{e,C}$), and the ionic potential ($\Phi_i$).

Simulations were performed on both coarse and fine computational meshes to verify the consistency of the full-domain adjoint PEMFC model. The analysis was conducted for both implementations of the Nernst potential 2.3.3 (Method 1 and Method 2 ) under potentiostatic operation at a fixed cell voltage of $E_{\text{cell}} = 0.6$ V.

#### Model Parameters: Method 1

The electrochemical parameters employed in the Butler–Volmer formulation are summarized in Tab. 3.7. The electrical conductivities used in the simulations are given in Tab. 3.8. The temperature is assumed constant at $T = 343.15$ K. The physical constants are taken as $F = 96485.33\,\text{C/mol}$ and $R = 8.314\,\text{J/(mol K)}$. The initial porosity in all porous regions is set to $\varepsilon_0 = 0.5$. The Nernst potential is imposed, with values $E_{\text{Nernst}} = 1.5558$ V at the cathode catalyst layer (CCL) and $E_{\text{Nernst}} = 0.3029$ V at the anode catalyst layer (ACL).

| Parameter | Unit | Value |
|---|---|---|
| $i_0$ (Anode) | $\text{A m}^{-3}$ | $1 \times 10^8$ |
| $i_0$ (Cathode) | $\text{A m}^{-3}$ | 120 |
| $\alpha$ | – | 0.5 |
| $\left(\frac{C_i}{C_{\text{ref}}}\right)^{\xi}$ | – | 1.0617 |

Table 3.7: Butler–Volmer parameters for Method 1.

| Parameter | Unit | Value |
|---|---|---|
| Electronic conductivity $\sigma_e$ (all electronic regions) | $\mathrm{S\,m^{-1}}$ | 2000 |
| Ionic conductivity $\sigma_i$ (all ionic regions) | $\mathrm{S\,m^{-1}}$ | 10 |

Table 3.8: Electrical conductivity parameters for Method 1.

### Model Parameters: Method 2

The corresponding Butler–Volmer parameters for Method 2 are presented in Tab. 3.9. The electrical conductivity values are listed in Tab. 3.10. The temperature, physical constants, and porosity are identical to those used in Method 1. In this formulation, a constant Nernst potential of $E_{\text{Nernst}} = 1.23$ V is assumed throughout the domain.

| Parameter | Unit | Value |
|---|---|---|
| $i_0$ (Anode) | $\mathrm{A\,m^{-3}}$ | $6 \times 10^5$ |
| $i_0$ (Cathode) | $\mathrm{A\,m^{-3}}$ | 120 |
| $\alpha$ | – | 0.5 |
| $\left(\frac{C_i}{C_{\text{ref}}}\right)^{\xi}$ | – | 0.6940 |

Table 3.9: Butler–Volmer parameters for Method 2.

| Parameter | Unit | Value |
|---|---|---|
| Electronic conductivity $\sigma_e$ (all electronic regions) | $\mathrm{S\,m^{-1}}$ | 1500 |
| Ionic conductivity $\sigma_i$ (all ionic regions) | $\mathrm{S\,m^{-1}}$ | 10 |

Table 3.10: Electrical conductivity parameters for Method 2.

### Results and Discussion

A key observation is that the sensitivity derivatives, obtained through both adjoint and finite-difference approaches, are strongly influenced by the volumetric contribution of each region. Since the adjoint formulation involves volume integrals, the GDLs, being significantly larger than the CLs and membrane, exhibit dominant contributions to the total sensitivity.

To ensure a consistent deviation assessment, the entire porous domain is also treated as a unified region, and the total sensitivity is evaluated accordingly. This serves as an initial verification step before extending the model to more complex configurations, such as spatially varying (e.g., polynomial) porosity distributions.

The derivatives computed using central finite differences show excellent agreement between the anode and cathode domains, with discrepancies of the order of $10^{-4}$ to $10^{-5}$ as the mesh is refined.

Similarly, the adjoint-derived sensitivities for the anode and cathode domains are nearly identical, with agreement up to five significant digits. Therefore, in the following analysis, results are presented for only one side (either anode or cathode), as the differences fall well below the desired tolerance.

Furthermore, it is observed that applying the objective function at either the ACL or the CCL yields nearly identical sensitivity distributions across both electrodes. When the objective function is applied simultaneously to both layers, the resulting sensitivities correspond to a simultaneous perturbation of porosity in the respective regions of both electrodes.

Based on these observations, the verification results are presented for both coarse and fine meshes, for the two Nernst implementations, and for both sensitivity evaluation approaches (central finite differences and adjoint method), considering the objective function applied at a single catalyst layer (ACL or CCL).

| **Region** | **Central FD** | **Adjoint** | **Deviation (%)** |
|---|---|---|---|
| *Coarse Mesh* | | | |
| AGDL | -0.007929183 | -0.007501527 | 5.393 |
| ACL | -0.000195090 | -0.000192667 | 1.242 |
| AMPL | -0.000296728 | -0.000294846 | 0.634 |
| *Fine Mesh* | | | |
| AGDL | -0.007799778 | -0.007560392 | 3.069 |
| ACL | -0.000191860 | -0.000189925 | 1.008 |
| AMPL | -0.000296018 | -0.000293141 | 0.326 |

Table 3.11: Comparison between central finite difference ($\delta\epsilon = 0.01$) and adjoint-derived sensitivities for Method 1.

| **Region** | **Central FD** | **Adjoint** | **Deviation (%)** |
|---|---|---|---|
| *Coarse Mesh* | | | |
| AGDL | -0.004777719 | -0.004700378 | 1.619 |
| ACL | -0.000121849 | -0.000120401 | 1.188 |
| AMPL | -0.000182312 | -0.000181186 | 0.617 |
| *Fine Mesh* | | | |
| AGDL | -0.004715906 | -0.004680907 | 0.742 |
| ACL | -0.000120493 | -0.000119321 | 0.973 |
| AMPL | -0.000180590 | -0.000180201 | 0.215 |

Table 3.12: Comparison between central finite difference ($\delta\epsilon = 0.01$) and adjoint sensitivities for the $\phi_{\text{all}}$ case using Method 2.

The verification results presented in Tabs. 3.11 and 3.12 demonstrate an excellent agreement between the derivatives obtained using the adjoint method and those computed by finite differences for both Nernst implementations. In all cases, the deviations remain below approximately $5.4\%$, with the largest discrepancies occurring in the GDL region

for the coarse mesh, while ACL and AMPL exhibit deviations close to or below 1%. As the mesh is refined, the agreement improves consistently, indicating the convergence of the adjoint method toward the finite-difference solution. The larger derivative magnitude observed in the GDL is expected since the adjoint method involves volume integrals, and the significantly larger volume of the GDL leads to a proportionally greater contribution to the objective function gradient. Overall, the close agreement between the two derivatives evaluation methods confirms the correctness of the adjoint method and provides confidence for its application to more complex optimization problems involving spatially varying porosity distributions.

# Chapter 4

# Three Equation Adjoint Model Development

## 4.1 Assumptions

After succesfuly developing the electric adjoint, the adjoint method is expanded by adding the two fluid equations, momentum and continuity, creating a three equation adjoint model solver. The objective function and the design variables are the same as described in sections 3.2 and 3.3. The flow is assumed to be single-phase and laminar, serving as an initial stage for the development and verification of the adjoint method. This assumption is consistent with high-temperature operating conditions, under which liquid water formation is neglected and only gaseous species are considered.

All other physical fields, including temperature, membrane water content, and species mass fractions, are assumed to be known and constant w.r.t. the design variable. For the adjoint formulation, the derivation is restricted to the governing equations of continuity, momentum, and charge conservation.

## 4.2 Augmented Objective Function

To incorporate the governing equations as constraints, an augmented functional is defined as:

$$F_{\text{aug}} = F + \int_{\Omega} u_i R_i^v \, d\Omega + \int_{\Omega} q R^p \, d\Omega + \int_{\Omega} \phi R^{\Phi} \, d\Omega \tag{4.1}$$

where $u_i$, $q$, and $\phi$ are the adjoint variables associated with momentum, continuity, and charge conservation, respectively. The residuals of the governing equations (Eqs. 2.2, 2.8,

2.19, 2.20) are given as:

$$R_i^v = \frac{\partial(\rho v_i v_j)}{\partial x_j} - \frac{\partial}{\partial x_j}\left(\mu(\frac{\partial v_i}{\partial x_j} + \frac{\partial v_j}{\partial x_i})\right) + \frac{\partial p}{\partial x_i} - \rho g + S_{Dacrcy}0 \tag{4.2}$$

$$R^p = -\frac{\partial(\rho v_j)}{\partial x_j} + R_k = 0 \tag{4.3}$$

$$R^\Phi = \frac{\partial}{\partial x_j}\left(\sigma_k \frac{\partial \Phi_k}{\partial x_j}\right) - J_k = 0 \tag{4.4}$$

Index $k \in \{E, I\}$ denotes the electronic and ionic phases, respectively.

## 4.3 Fluid Region

The primary variables in this region are pressure $p$ and velocity field **v**.

### 4.3.1 Continuity Equation

$$-\frac{\partial(\rho v_j)}{\partial x_j} + R_k = 0 \tag{4.5}$$

The variation $\delta$ of the continuity equation, multiplied by the adjoint variable $q$, yields:

$$-\int_\Omega q\frac{\partial}{\partial x_j}\delta(\rho v_j)\, d\Omega = -\int_S q(v_j\delta\rho + \rho\delta v_j)n_j\, dS + \int_\Omega \frac{\partial q}{\partial x_j} v_j \delta\rho\, d\Omega + \int_\Omega \frac{\partial q}{\partial x_j}\rho\delta v_j\, d\Omega \tag{4.6}$$

The contribution from the source term is:

$$\int_\Omega q\, \delta R_k\, d\Omega = \int_\Omega q \frac{J_{adj}\, \omega \sum M_i}{zF}\, \delta\Phi_k d\Omega \tag{4.7}$$

### 4.3.2 Momentum Equations

The momentum equations are applied over the entire fluid domain:

$$\frac{\partial(\rho v_i v_j)}{\partial x_j} - \frac{\partial}{\partial x_j}\left(\mu\frac{\partial v_i}{\partial x_j}\right) + \frac{\partial p}{\partial x_i} - \rho g = 0 \tag{4.8}$$

**Differentiation of the Convection Term**

$$\begin{aligned}\int_\Omega u_i\,\delta\left(\frac{\partial}{\partial x_j}(\rho v_i v_j)\right)d\Omega = &\int_S u_i\,\delta(\rho v_i v_j)n_j\,dS\\ &-\int_\Omega \frac{\partial u_i}{\partial x_j}\rho v_i\delta v_j\,d\Omega - \int_\Omega \frac{\partial u_i}{\partial x_j}\rho v_j\delta v_i\,d\Omega\\ &-\int_\Omega \frac{\partial u_i}{\partial x_j}v_j v_i\delta\rho\,d\Omega\end{aligned} \tag{4.9}$$

By reindexing terms involving $\delta v_j$:

$$-\int_\Omega \frac{\partial u_i}{\partial x_j}\rho v_i\delta v_j\,d\Omega - \int_\Omega \frac{\partial u_i}{\partial x_j}\rho v_j\delta v_i\,d\Omega = -\int_\Omega\left(\frac{\partial u_j}{\partial x_i}\rho v_j + \frac{\partial u_i}{\partial x_j}\rho v_j\right)\delta v_i\,d\Omega \tag{4.10}$$

**Differentiation of the Diffusion Term**

$$\begin{aligned}-\int_\Omega u_i\frac{\partial}{\partial x_j}\left(\delta\left(\mu(\frac{\partial v_i}{\partial x_j}+\frac{\partial v_j}{\partial x_i})\right)\right)d\Omega =\\ -\int_S u_i\left(\delta\left(\mu\frac{\partial v_i}{\partial x_j}\right)\right)n_j dS + \int_\Omega \frac{\partial u_i}{\partial x_j}\left(\delta\left(\mu\frac{\partial v_i}{\partial x_j}\right)\right)d\Omega\\ -\int_S u_i\left(\delta\left(\mu\frac{\partial v_j}{\partial x_i}\right)\right)n_j dS + \int_\Omega \frac{\partial u_i}{\partial x_j}\left(\delta\left(\mu\frac{\partial v_j}{\partial x_i}\right)\right)d\Omega\end{aligned} \tag{4.11}$$

Applying the Green–Gauss theorem:

$$\int_\Omega \frac{\partial u_i}{\partial x_j}\left(\delta\left(\mu\frac{\partial v_i}{\partial x_j}\right)\right)d\Omega = \int_S \frac{\partial u_i}{\partial x_j}\mu\delta v_i n_j dS - \int_\Omega \frac{\partial^2 u_i}{\partial x_j^2}\mu\delta v_i d\Omega \tag{4.12}$$

$$\int_\Omega \frac{\partial u_i}{\partial x_j}\left(\delta\left(\mu\frac{\partial v_j}{\partial x_i}\right)\right)d\Omega = \int_S \frac{\partial u_i}{\partial x_j}\mu\delta v_j n_i dS - \int_\Omega \frac{\partial^2 u_i}{\partial x_j\partial x_i}\mu\delta v_j d\Omega \tag{4.13}$$

Thus, the diffusion term produces three surface integrals and two volume integral:

$$\begin{aligned}-\int_\Omega u_i\frac{\partial}{\partial x_j}\left[\mu\delta\left(\frac{\partial v_i}{\partial x_j}+\frac{\partial v_j}{\partial x_i}\right)\right]d\Omega = &-\int_S u_i\,\delta\mu\left(\frac{\partial v_i}{\partial x_j}+\frac{\partial v_j}{\partial x_i}\right)n_j\,dS\\ &+\int_S \frac{\partial u_i}{\partial x_j}\,\mu\,\delta v_i\,n_j\,dS + \int_S \frac{\partial u_j}{\partial x_i}\,\mu\,\delta v_i\,n_j\,dS\\ &-\int_\Omega \frac{\partial^2 u_i}{\partial x_j^2}\,\mu\,\delta v_i\,d\Omega - \int_\Omega \frac{\partial^2 u_j}{\partial x_j\partial x_i}\,\mu\,\delta v_i\,d\Omega.\end{aligned} \tag{4.14}$$

**Differentiation of the Pressure Gradient Term**

The contribution of the pressure gradient term to the variation of the objective function is considered by:

$$\int_{\Omega} u_i \frac{\partial}{\partial x_i}(\delta p)\, d\Omega = \int_{S} u_i(\delta p) n_i\, dS - \int_{\Omega} \frac{\partial u_i}{\partial x_i} \delta p\, d\Omega \tag{4.15}$$

**Differentiation of the Darcy Porous Resistance Term**

The Darcy porous resistance term given in Eq.2.9. As referred to previously, the system is treated as single-phase; hence, the primal velocity corresponds to the velocity of the continuous phase and is differentiated as follows:

$$\begin{aligned} \delta S_{Darcy} = &- \int_{\Omega} u_i(\mu\alpha + 0.5 * \rho|\mathbf{v}|\beta)\delta v_i\, d\Omega - \int_{\Omega} u_j v_j (0.5 * \rho\beta)\frac{v_i}{|\mathbf{v}|}\delta v_i\, d\Omega \\ &- \int_{\Omega} u_i(\mu\delta\alpha + 0.5 * \rho|\mathbf{v}|\delta\beta) v_i\, d\Omega \end{aligned} \tag{4.16}$$

### 4.3.3 Mixture Ideal Gas Law

The mixture is assumed to obey the ideal gas law:

$$p = \rho T \sum_k Y_k R_k, \qquad R_k = \frac{R_u}{M_k} \tag{4.17}$$

Since the species mass fractions are constant, p variations simplify to:

$$\delta p = \delta\rho\, T \sum_k Y_k R_k \tag{4.18}$$

### 4.3.4 Porosity Sensitivity of the Porous Resistance

Their derivatives w.r.t. porosity are:

$$\frac{\partial \alpha}{\partial \varepsilon} = \frac{150}{d_p^2}\left[-2(1-\varepsilon)\varepsilon^{-3} - 3(1-\varepsilon)^2\varepsilon^{-4}\right], \tag{4.19}$$

$$\frac{\partial \beta}{\partial \varepsilon} = \frac{3.5}{d_p}\left[-\varepsilon^{-3} - 3(1-\varepsilon)\varepsilon^{-4}\right]. \tag{4.20}$$

The porous resistance tensor is

$$C_{ij} = \mu\alpha_{ij} + \frac{1}{2}\rho\beta_{ij}|\mathbf{v}|, \tag{4.21}$$

yielding the momentum sink

$$R_i = C_{ij} u_j. \tag{4.22}$$

Differentiation w.r.t. porosity gives

$$\frac{\partial R_i}{\partial \varepsilon} = \left( \mu \frac{\partial \alpha_{ij}}{\partial \varepsilon} + \frac{1}{2} \rho |\mathbf{v}| \frac{\partial \beta_{ij}}{\partial \varepsilon} \right) u_j. \tag{4.23}$$

The adjoint-based sensitivity is then obtained as

$$\delta F = \int_\Omega u_i \left( \mu \delta \alpha_{ij} + \frac{1}{2} \rho |\mathbf{v}| \delta \beta_{ij} \right) v_i d\Omega \tag{4.24}$$

where $u_i$ denotes the adjoint velocity field. This expression is evaluated locally in each control volume and accumulated to form the total gradient w.r.t. porosity.

## 4.4 Differentiation of the Objective Function

The objective function is influenced by not only by the primal electric potentials $\Phi_E$ and $\Phi_I$, but also by the dependence of the Nernst potential on the pressure field. According to Eq. 2.32, the pressure dependence of the Nernst potential introduces an additional contribution to the adjoint pressure equation through the variation of the objective function. The corresponding variation can be written as

$$\delta E_{\text{Nernst},ae} = \frac{1}{zF} \sum_i \left[ -R_g T \, \omega \frac{1}{p_i} \right] \tag{4.25}$$

Furthermore, by differentiating the Butler–Volmer equation (Eq. 2.30), the contribution of the objective function within the fluid domain can be derived. This contributes to the continuity equation through the coefficient associated with $\delta p$. The resulting sensitivity term is expressed as

$$\begin{aligned} \delta j_{\text{Nernst}} = i_{ae,0} (1 - \alpha_l)^\gamma \prod_{\text{reac},i} \left( \frac{C_i}{C_{\text{ref}}} \right)^\xi \delta E_{\text{Nernst},ae} \\ \times \left[ \frac{\alpha_{ae} z F}{R_g T} \exp\left( -\frac{\alpha_{ae} z F \eta_{ae}}{R_g T} \right) + \frac{(1 - \alpha_{ae}) z F \eta_{ae}}{R_g T} \exp\left( \frac{(1 - \alpha_{ae}) z F \eta_{ae}}{R_g T} \right) \right] \end{aligned} \tag{4.26}$$

An analogous procedure is applied to the source terms appearing in the continuity and potential equations. Consequently, the total contribution of the objective function to the continuity equation can be written as follows:

$$\delta J_{\text{Nernst}} = (1 - \Phi_E + \Phi_I)\delta j_{Nenrst} + q\frac{\omega \Sigma M_i}{zF}\delta j_{Nernst} \tag{4.27}$$

## 4.5 Total Derivative of the Augmented Objective Function

By combining all the derived terms , the total vriation of $F_{Aug}$, $\delta F_{Aug}$ is obtained.

$$\begin{aligned}
\delta F_{\text{aug}} = & \int_\Omega \left( \frac{\partial q}{\partial x_j} v_j - \frac{\partial u_i}{\partial x_j} v_j v_i - (\frac{\partial u_i}{\partial x_i} - \delta J_{Nernst}) \frac{p}{\rho} \right) \delta\rho \, d\Omega \\
& + \int_\Omega \left( +\rho \frac{\partial q}{\partial x_i} - \rho v_j \left( \frac{\partial u_j}{\partial x_i} + \frac{\partial u_i}{\partial x_j} \right) - \mu \frac{\partial}{\partial x_j} (\frac{\partial u_i}{\partial x_j} + \frac{\partial u_j}{\partial x_i} + \delta S_{Darcy} \right) \delta v_i \, d\Omega \\
& + \int_\Omega \left( \frac{\partial}{\partial x_j} \left( \sigma_k \frac{\partial \phi_k}{\partial x_j} \right) + C_t - \phi_k \delta S_k - \phi_k \delta S_k + C_t q \frac{\omega \sum M_i}{zF} \right) \delta\Phi_k \, d\Omega \\
& \int_S (-q v_j n_j + u_i v_i v_j n_j + u_i n_i \frac{p}{\rho}) \delta\rho \, dS \\
& \int_S (-\rho q n_i + u_i \rho v_j n_j + u_j \rho v_j n_i + \mu (\frac{\partial u_i}{\partial x_j} + \frac{\partial u_j}{\partial x_i}) n_j) \delta v_i \, dS \\
& - \int_S u_i n_j \left( \mu\delta \left( \frac{\partial v_i}{\partial x_j} + \frac{\partial v_j}{\partial x_i} \right) \right) dS - \int_S \phi n_j \delta (\sigma_k \frac{\partial \Phi_k}{\partial x_j}) dS \\
& - \int_S \frac{\partial \phi_k}{\partial x_j} \sigma_k n_j \delta\Phi_k dS - \int_\Omega \frac{\partial \phi_k}{\partial x_j} \frac{\partial \Phi_k}{\partial x_j} \delta\sigma_k d\Omega - \int_\Omega u_i \left( \mu\delta\alpha_{ij} + \frac{1}{2}\rho |\mathbf{v}| \delta\beta_{ij} \right) v_i d\Omega
\end{aligned} \tag{4.28}$$

where index $k \in \{\text{E}, \text{I}\}$ denotes the electronic and proton domains and index $t \in \{\text{a}, \text{c}\}$ denotes the anode and cathode domains, respectively.

## 4.6 Field Adjoint Equations

In order to avoid the explicit computation of the sensitivities of the objective function with respect to the primary variables, the field adjoint equations (FAEs) are formulated such that the coefficients $\delta p$ and $\delta v_i$ vanish. This leads to a system of adjoint equations for continuity, momentum, and electric potentials, which are driven by the corresponding sensitivity source terms.

### Adjoint Continuity Equation

$$\frac{\partial q}{\partial x_j} v_j - \frac{\partial u_i}{\partial x_j} v_j v_i - \left( \frac{\partial u_i}{\partial x_i} - \delta J_{\text{Nernst}} \right) \frac{p}{\rho} = 0 \tag{4.29}$$

### Adjoint Momentum Equation

$$\begin{aligned} &\frac{\partial q}{\partial x_i}\rho - \frac{\partial u_j}{\partial x_i}\rho v_j - \frac{\partial u_i}{\partial x_j}\rho v_j \\ &\quad - \mu \frac{\partial}{\partial x_j}\left( \frac{\partial u_i}{\partial x_j} + \frac{\partial u_j}{\partial x_i} \right) - u_i(\mu\alpha + 0.5 * \rho|\mathbf{v}|\beta) - u_j v_j (0.5 * \rho\beta)\frac{v_i}{|\mathbf{v}|} = 0 \end{aligned} \tag{4.30}$$

### Adjoint Potential Equations

**Electronic domain:**

$$\frac{\partial}{\partial x_j}\left( \sigma_E \frac{\partial \phi_E}{\partial x_j} \right) + C_k - \phi_E \delta S_E - \phi_I \delta S_I + C_k q \frac{\omega \sum M_i}{zF} = 0 \tag{4.31}$$

**Proton domain:**

$$\frac{\partial}{\partial x_j}\left( \sigma_I \frac{\partial \phi_I}{\partial x_j} \right) + C_k - \phi_I \delta S_I - \phi_E \delta S_E - C_k q \frac{\omega \sum M_i}{zF} = 0 \tag{4.32}$$

## 4.7 Adjoint Boundary Conditions

The adjoint boundary conditions are derived from the surface integrals in Eq. 4.28 that arise after applying the Green-Gauss theorem to the variation of the augmented functional. These surface integrals must vanish for arbitrary variations, leading to the appropriate adjoint boundary conditions (ABCs).

For the primal velocity field **v**, Dirichlet boundary conditions are imposed along the GC inlets (prescribed velocity), while no-slip conditions are applied along the solid walls. For the pressure, Dirichlet conditions are imposed at the outlet of the fluid channels and zero Neumann conditions are applied everywhere else.

### 4.7.1 Adjoint Fluid Boundary Conditions

For the fluid domain, three surface integrals must vanish. The fluid boundary domain is divided into three patches: $S_I$, $S_W$, and $S_O$. These are explained below:

- $S_I$ is the inlet domain of the GCs (both anode and cathode); there, the boundary conditions are zero Neumann for the pressure and fixed-value for the velocity.

- $S_W$ is the ensemble of solid walls, where the velocity is set to zero and the pressure follows a zero Neumann condition.
- $S_O$ is the outlet patch of the GCs (both anode and cathode), where zero Neumann for the velocity and zero Dirichlet for the pressure are imposed.

The surface terms $\delta\rho$ and $\delta p$ are grouped together via Eq. 4.18.

$$\int_S \left( -qv_j n_j + u_i v_i v_j n_j + u_i n_i \frac{p}{\rho} \right) \delta\rho \, dS = 0 \tag{4.33}$$

The surface terms $\delta v_i$ and $\delta \left( \frac{\partial v_i}{\partial x_j} \right)$ are grouped separately:

$$\int_S \left( -\rho q n_i + (u_j v_j \rho n_i + u_i v_j \rho n_j) + (\frac{\partial u_i}{\partial x_j} + \frac{\partial u_j}{\partial x_i})\mu n_j \right) (\delta v_i) \, dS = 0 \tag{4.34}$$

$$\int_S (u_i n_j)\mu\delta \left( \frac{\partial v_i}{\partial x_j} + \frac{\partial v_j}{\partial x_i} \right) dS = 0 \tag{4.35}$$

**Inlet Boundaries** $S_I$ For Eq. 4.35, the primal velocity field has zero Neumann boundary conditions at the outlet and Dirichlet boundary conditions elsewhere. Therefore, this term must vanish at the walls and the inlet. The term $u_i n_j$ is expanded into the normal component $(n_i)$ and the tangential components $(t_i^I, t_i^{II})$ projected onto the inlet surface as:

$$u_i = u_{<n>} n_i + u^I_{<t>} t^I_i + u^{II}_{<t>} t^{II}_i \tag{4.36}$$

Thus, Eq. 4.35 becomes:

$$\int_S \left( u_{<n>} n_i + u^I_{<t>} t^I_i + u^{II}_{<t>} t^{II}_i \right) n_j \delta \left( \mu \frac{\partial v_i}{\partial x_j} + \mu \frac{\partial v_j}{\partial x_i} \right) dS = \int_S \left( u_{<n>} \delta \left( 2\mu \frac{\partial v_n}{\partial n} \right) + u^I_{<t>} \delta \left( \mu \left( \frac{\partial v^I_t}{\partial n} + \frac{\partial v_n}{\partial t^I} \right) \right) + u^{II}_{<t>} \delta \left( \mu \left( \frac{\partial v^{II}_t}{\partial n} + \frac{\partial v_n}{\partial t^{II}} \right) \right) \right) dS \tag{4.37}$$

Taking the continuity equation evaluated at $S_I$ into account:

$$\frac{\partial v_i}{\partial x_i} = \frac{\partial}{\partial x_i} \left( v_{<n>} n_i + v^I_{<t>} t^I_i + v^{II}_{<t>} t^{II}_i \right) = \frac{\partial v_n}{\partial n} + \frac{\partial v^I_t}{\partial t^I} + \frac{\partial v^{II}_t}{\partial t^{II}} = 0 \tag{4.38}$$

Term $\frac{\partial v_n}{\partial n}$ vanishes automatically for flows with a uniform tangential velocity profile at the inlet, because

$$\frac{\partial v_n}{\partial n} = -\frac{\partial v^I_t}{\partial t^I} - \frac{\partial v^{II}_t}{\partial t^{II}}$$

For the surface integral in Eq. 4.37 to vanish, the tangential adjoint velocities must be zero at the inlet:

$$u^I_{<t>}, u^{II}_{<t>} = 0 \tag{4.39}$$

At the inlet, and taking into account that $p$ has a zero Neumann condition, the term $\delta p$ (equivalently $\delta\rho$) must vanish. Multiplying Eq. 4.33 by $n_i^2$ yields:

$$\int_S \left( -q v_{<n>} + u_{<n>} v_{<n>} v_{<n>} + u_{<n>} \frac{p}{\rho} \right) \delta\rho \, dS = 0 \tag{4.40}$$

Hence, at the inlet, the following boundary conditions are applied:

$$q, u_{<n>} = 0 \tag{4.41}$$

**Walls** Using the same procedure, and because $v_n = 0$ at the walls, no adjoint pressure derivative condition is required; therefore, a zero Neumann condition is applied. In addition, $u_{<n>} = 0$ is needed for the surface integral in Eq. 4.33 to vanish. For Eq. 4.35, the adjoint velocity components must be zero following the same reasoning as in the inlet domain.

Therefore, the following boundary conditions are applied at the walls $S_w$:

$$\frac{\partial q}{\partial n}, u_{<n>}, u^I_{<t>}, u^{II}_{<t>} = 0 \tag{4.42}$$

**Outlet** At the outlet, a zero Dirichlet boundary condition is imposed on the pressure, so the surface integral in Eq. 4.33 vanishes because $\delta p = 0$. Also, a zero Neumann boundary condition exists for velocity, so the surface integral in Eq. 4.35 vanishes because $\delta\left(\mu \frac{\partial v_i}{\partial x_j}\right) = 0$. Consequently, only the surface integral in Eq. 4.34 remains.

Multiplying Eq. 4.34 by $n_i n_j^2$ gives:

$$\int_S \left( -\rho q + (u_{<n>} v_{<n>} \rho + u_{<n>} v_{<n>} \rho) + 2 \frac{\partial u_n}{\partial n} \mu \right) \delta v_i \, dS = 0 \tag{4.43}$$

Multiplying Eq. 4.34 by $t_i^I$ yields:

$$\int_S \left( u^I_{<t>} v_{<n>} \rho + \mu \left( \frac{\partial u_t^I}{\partial n} + \frac{\partial u_n}{\partial t^I} \right) \right) \delta v_i \, dS = 0 \tag{4.44}$$

Multiplying Eq. 4.34 by $t_i^{II}$ yields:

$$\int_S \left( u^{II}_{<t>} v_{<n>} \rho + \mu \left( \frac{\partial u_t^{II}}{\partial n} + \frac{\partial u_n}{\partial t^{II}} \right) \right) (\delta v_i) \, dS = 0 \tag{4.45}$$

Thus, there are three equations for four unknown values. In this work, $q = 0$ is set at the outlet, which yields a Robin-type boundary condition Eqs. 4.45, 4.43, 4.44 for the adjoint velocity components.

Table 4.1: Summary of adjoint fluid boundary conditions. The notation $u_{<n>}$ refers to the normal component of the adjoint velocity, $u^I_{<t>}, u^{II}_{<t>}$ to its tangential components, and $q$ to the adjoint pressure adjoint variable.

| **Boundary region** | **Primal BC** (for velocity $v_i$ and pressure $p$) | **Adjoint BC** (for $u_i$, $q$) |
|---|---|---|
| Inlet $S_I$ | • $\frac{\partial p}{\partial n} = 0$<br>• $v_i$: fixed value (Dirichlet) | • $q = 0$<br>• $u_{<n>} = 0$<br>• $u^I_{<t>} = u^{II}_{<t>} = 0$ |
| Walls $S_W$ | • $\frac{\partial p}{\partial n} = 0$<br>• $v_i$: fixed value (Dirichlet) | • $\frac{\partial q}{\partial n} = 0$<br>• $u_{<n>} = 0$<br>• $u^I_{<t>} = u^{II}_{<t>} = 0$ |
| Outlet $S_O$ | • $p = 0$ (Dirichlet)<br>• $\frac{\partial v_i}{\partial n} = 0$ | • $q = 0$<br>• $u_{<n>}$, $u^I_{<t>}$, $u^{II}_{<t>}$ satisfy Robin-type conditions derived from Eqs. (4.43)–(4.45) |

The boundary conditions for the adjoint potential equations are identical to those derived in Chapter 3.

## 4.8 Sensitivity Derivatives

The variation of the objective function is given by:

$$\delta F = -\int_{\Omega_E} \frac{\partial \phi_E}{\partial x_j}\frac{\partial \Phi_E}{\partial x_j}\delta\sigma_E \, d\Omega - \int_{\Omega_I} \frac{\partial \phi_I}{\partial x_j}\frac{\partial \Phi_I}{\partial x_j}\delta\sigma_I \, d\Omega + \int_{\Omega_{Fluid}} u_i \left(\mu\delta\alpha_{ij} + \frac{1}{2}\rho|v|\delta\beta_{ij}\right) v_i d\Omega \tag{4.46}$$

From Eq. 4.46, the adjoint derivatives w.r.t. the porosity of each porous layer are obtained by restricting the variation to the corresponding region. Consequently, the derivative

of the objective function w.r.t. porosity of each region is given by:

$$\frac{\delta F}{\delta b_{\text{AGDL}}} = -\int_{\Omega_{\text{AGDL}}} \frac{\partial \phi_E}{\partial x_j}\frac{\partial \Phi_E}{\partial x_j}\frac{\partial \sigma_E}{\partial b_{\text{AGDL}}}\, d\Omega + \int_{\Omega_{\text{AGDL}}} u_i \left(\mu \frac{\partial \alpha_{ij}}{\partial b_{\text{AGDL}}} + \frac{1}{2}\rho|\mathbf{v}|\frac{\partial \beta_{ij}}{\partial b_{\text{AGDL}}}\right) v_i\, d\Omega, \tag{4.47}$$

$$\frac{\delta F}{\delta b_{\text{ACL}}} = -\int_{\Omega_{\text{ACL}}} \frac{\partial \phi_E}{\partial x_j}\frac{\partial \Phi_E}{\partial x_j}\frac{\partial \sigma_E}{\partial b_{\text{ACL}}}\, d\Omega - \int_{\Omega_{\text{ACL}}} \frac{\partial \phi_I}{\partial x_j}\frac{\partial \Phi_I}{\partial x_j}\frac{\partial \sigma_I}{\partial b_{\text{ACL}}}\, d\Omega + \int_{\Omega_{\text{ACL}}} u_i \left(\mu \frac{\partial \alpha_{ij}}{\partial b_{\text{ACL}}} + \frac{1}{2}\rho|\mathbf{v}|\frac{\partial \beta_{ij}}{\partial b_{\text{ACL}}}\right) v_i\, d\Omega, \tag{4.48}$$

$$\frac{\delta F}{\delta b_{\text{AMPL}}} = -\int_{\Omega_{\text{AMPL}}} \frac{\partial \phi_E}{\partial x_j}\frac{\partial \Phi_E}{\partial x_j}\frac{\partial \sigma_E}{\partial b_{\text{AMPL}}}\, d\Omega + \int_{\Omega_{\text{AMPL}}} u_i \left(\mu \frac{\partial \alpha_{ij}}{\partial b_{\text{AMPL}}} + \frac{1}{2}\rho|\mathbf{v}|\frac{\partial \beta_{ij}}{\partial b_{\text{AMPL}}}\right) v_i\, d\Omega, \tag{4.49}$$

$$\frac{\delta F}{\delta b_{\text{CCL}}} = -\int_{\Omega_{\text{CCL}}} \frac{\partial \phi_E}{\partial x_j}\frac{\partial \Phi_E}{\partial x_j}\frac{\partial \sigma_E}{\partial b_{\text{CCL}}}\, d\Omega - \int_{\Omega_{\text{CCL}}} \frac{\partial \phi_I}{\partial x_j}\frac{\partial \Phi_I}{\partial x_j}\frac{\partial \sigma_I}{\partial b_{\text{CCL}}}\, d\Omega + \int_{\Omega_{\text{CCL}}} u_i \left(\mu \frac{\partial \alpha_{ij}}{\partial b_{\text{CCL}}} + \frac{1}{2}\rho|\mathbf{v}|\frac{\partial \beta_{ij}}{\partial b_{\text{CCL}}}\right) v_i\, d\Omega, \tag{4.50}$$

$$\frac{\delta F}{\delta b_{\text{CMPL}}} = -\int_{\Omega_{\text{CMPL}}} \frac{\partial \phi_E}{\partial x_j}\frac{\partial \Phi_E}{\partial x_j}\frac{\partial \sigma_E}{\partial b_{\text{CMPL}}}\, d\Omega + \int_{\Omega_{\text{CMPL}}} u_i \left(\mu \frac{\partial \alpha_{ij}}{\partial b_{\text{CMPL}}} + \frac{1}{2}\rho|\mathbf{v}|\frac{\partial \beta_{ij}}{\partial b_{\text{CMPL}}}\right) v_i\, d\Omega, \tag{4.51}$$

$$\frac{\delta F}{\delta b_{\text{CGDL}}} = -\int_{\Omega_{\text{CGDL}}} \frac{\partial \phi_E}{\partial x_j}\frac{\partial \Phi_E}{\partial x_j}\frac{\partial \sigma_E}{\partial b_{\text{CGDL}}}\, d\Omega + \int_{\Omega_{\text{CGDL}}} u_i \left(\mu \frac{\partial \alpha_{ij}}{\partial b_{\text{CGDL}}} + \frac{1}{2}\rho|\mathbf{v}|\frac{\partial \beta_{ij}}{\partial b_{\text{CGDL}}}\right) v_i\, d\Omega. \tag{4.52}$$

## 4.9 Verification of the Three-Equation Domain Model

The model parameters for the electric domain are those utilized for the electric adjoint model in Chapter 3, under Method 1. Furthermore, the geometry remains the same as described in Section 3.9.1.

To verify the accuracy of the computed adjoint derivatives, the same procedure established in Chapter 3 is followed, validating the results against central finite differences. The fluid domain model parameters used during this verification process are summarized in Tab. 4.2.

Table 4.2: Fluid domain model parameters.

| **Parameter** | **SI Unit** | **Value** |
|---|---|---|
| Reference Pressure ($P_{\text{ref}}$) | Pa | 101 325 |
| Pore Diameter ($d_{\text{pore}}$) | m | 1.333333e-06 |
| Specific Heat Capacity ($C_p$) | $\text{J}/(\text{kg} \cdot \text{K})$ | 568 |
| Thermal Conductivity ($k$) | $\text{W}/(\text{m} \cdot \text{K})$ | 1.7 |
| $H_2O$ Molecular Weight | $\text{kg mol}^{-1}$ | 18.0153e-03 |
| $H_2$ Molecular Weight | $\text{kg mol}^{-1}$ | 2.01594e-03 |
| $O_2$ Molecular Weight | $\text{kg mol}^{-1}$ | 31.9988e-03 |
| $N_2$ Molecular Weight | $\text{kg mol}^{-1}$ | 28.0134e-03 |
| Temperature (T) | K | 434.15K |

Table 4.3: Comparison of central finite difference and adjoint sensitivities for the AGDL parameter. The percentage deviation between both approaches is presented, too.

| Voltage | Mesh | $e_0$ | $\Delta e$ | Central FD | Adjoint | Deviation (%) |
|---|---|---|---|---|---|---|
| 0.6 V | Fine | 0.5 | 0.001 | 0.005948924 | 0.006002257 | -0.896517 |
| 0.6 V | Coarse | 0.5 | 0.001 | 0.005853548 | 0.005949379 | -1.637138 |
| 0.8 V | Coarse | 0.3 | 0.001 | 0.074164382 | 0.073196540 | 1.304996 |

Table 4.4: Comparison of central finite difference and adjoint sensitivities for the CGDL parameter. Percentage deviations are also presented.

| Voltage | Mesh | $e_0$ | $\Delta e$ | Central FD | Adjoint | Deviation (%) |
|---|---|---|---|---|---|---|
| 0.6 V | Fine | 0.5 | 0.001 | -0.000609529 | -0.000621632 | -1.985624 |
| 0.6 V | Coarse | 0.5 | 0.001 | -0.000619043 | -0.000633346 | -2.310494 |
| 0.8 V | Coarse | 0.3 | 0.001 | -0.006786682 | -0.007057185 | -3.985793 |

As shown in Tabs. 4.3 and 4.4, the adjoint derivatives deviate less from the central finite differences results decreases as the mesh is refined. This behavior confirms the expected mesh convergence of the adjoint formulation.

Furthermore, it can be observed that, for different initial porosity values $\epsilon_0$, the deviation increases as the porosity approaches its limiting value of zero. This trend can be attributed to the nonlinear behavior introduced by the Carman–Kozeny relations (Eqs. 2.10 and 2.11), where the porous resistance increases significantly at low porosity values. As a consequence, the governing equations become increasingly stiff, which negatively affects the convergence behavior of the numerical solver and reduces the accuracy of the primal solution.

In comparison with the electric adjoint model presented in Chapter 3, a smaller perturbation value of $\Delta\varepsilon = 0.001$ was employed in the present study, whereas $\Delta\varepsilon = 0.01$ was used in the purely electric case. This adjustment is justified by the reduced nonlinearity of the present coupled electro-fluid formulation. The inclusion of the Navier–Stokes equations introduces additional physical coupling; however, the overall system exhibits a more linear response w.r.t. the considered perturbation, allowing for a smaller finite-difference step

size while maintaining numerical stability and accuracy.

## 4.10 Optimization Loop

Following the excellent agreement obtained between the finite difference approximations and the adjoint-based derivatives, an optimization procedure was implemented to evaluate the capability of the developed software to improve the porous transport properties. Two independent optimization loops were performed at different operating conditions, namely at $0.6$ V and $0.8$ V, in order to investigate the influence of the operating voltage on the optimal porosity distribution. The design variables are those described in 3.3.

For the first optimization case ($0.6$ V), the initial values of all design variables were uniformly initialized to a porosity value of $0.5$. In the second case ($0.8$ V), a lower initial porosity value of $0.3$ was selected.

The optimization process is guided by the gradient computed from the adjoint method. Using the current three-equation model, the sensitivities associated with the electrical transport phenomena dominate over those related to the fluid transport mechanisms. In particular, the cathode-side electrical contribution presents significantly larger derivatives compared with the fluid contribution.

As a consequence, the optimization algorithm tends to decrease the porosity values in the cathode-side layers. This reduction increases the effective electrical conductivity by improving the solid-phase connectivity, which results in an overall improvement of the objective function. Although the reduction in porosity increases the porous resistance, this negative contribution remains smaller than the electrical benefit within the current physical model. Therefore, the optimization converges towards lower porosity values, reaching the imposed minimum porosity bound for the cathode regions.

As observed in Tab. 4.5, the optimized porosity values within the anode regions (AMPL and ACL) exhibit remarkable similarity regardless of the operating voltage. Specifically, despite starting from different initial states ($0.500$ at 0.6 V versus $0.300$ at 0.8 V), the optimization algorithm converges to approximately $0.46$ for the AMPL and $0.40$ for the ACL in both operating conditions. This behavior indicates that the mass transport and electrochemical requirements on the anode side remain relatively insensitive to the cell voltage variations within this range, guiding the design toward a unified optimal porosity distribution.

The optimized porosity distributions indicate a clear difference between the anode and cathode sides. The CGDL porosity reaches the lower imposed bound in both operating conditions, confirming that the electrical contribution dominates the optimization direction. On the other hand, the AGDL porosity converges to intermediate values, indicating a balance between electrical conductivity enhancement and the resistance associated with reduced permeability.

For the $0.6$ V optimization case, the cathode sensitivity remains negative and increases in magnitude throughout the optimization process, driving the CGDL porosity towards its minimum value 0.15. The AGDL sensitivity oscillates around zero, indicating that the

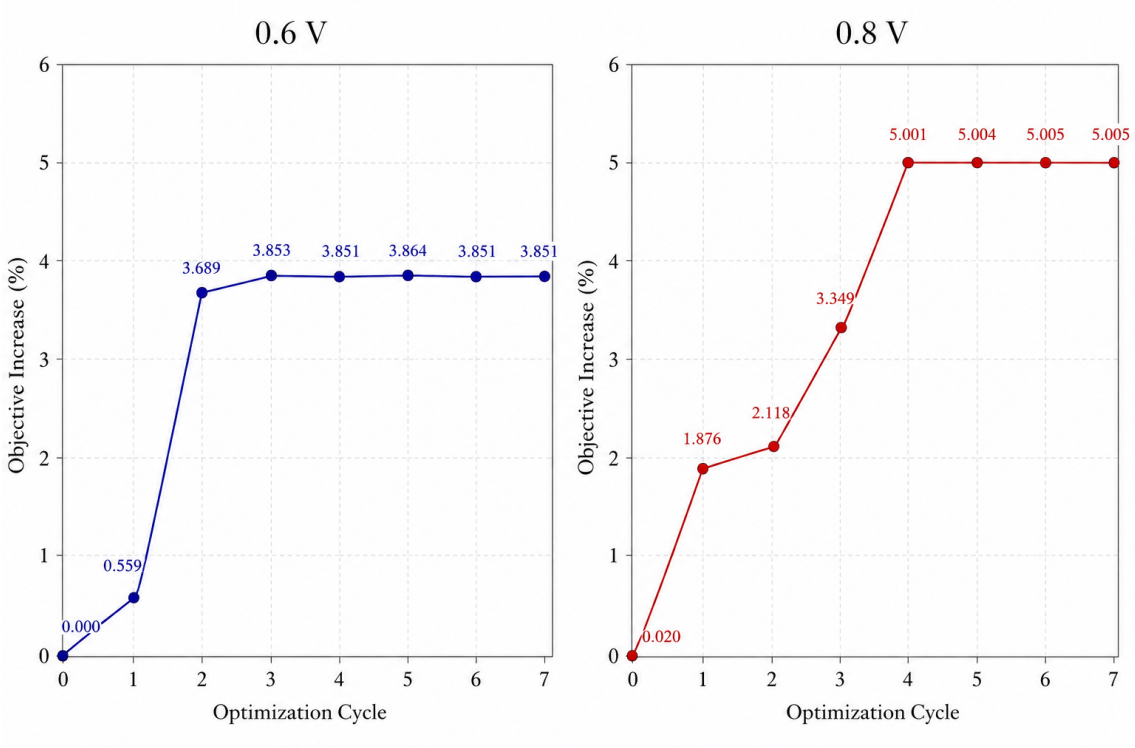


Figure 4.1: Evolution of percentage increase in the objective function value during the optimization loops at 0.6 V (left) and 0.8 V (right).

algorithm approaches an optimum.

For the $0.8$ V case, the optimization demonstrates a faster improvement of the objective function. The AGDL porosity increases during the first iterations before reaching a plateau, while the CGDL again decreases rapidly towards the lower porosity bound.

## 4.11 Evaluation Using the Full Two-Phase Model

Following the completion of the optimization procedure based on the reduced three-equation single-phase adjoint model, the obtained optimal design was evaluated using the full two-phase primal solver. This verification step is necessary to assess the performance of the optimized configuration under the complete physical model, which accounts for all relevant two-phase transport phenomena.

The current obtained from the initial design was

$$I_0 = 0.1046 \text{ A}. \tag{4.53}$$

After applying the optimized design to the full two-phase model, the resulting current became

Table 4.5: Initial and optimized porosity values for the optimized AMPL, ACL, CMPL and CCL regions.

| Region | Initial Porosity | Optimized Porosity |
|---|---|---|
| | 0.6 V | |
| AGDL | 0.500 | 0.493 |
| AMPL | 0.500 | 0.459 |
| ACL | 0.500 | 0.413 |
| CGDL | 0.500 | 0.15 |
| CMPL | 0.500 | 0.150 |
| CCL | 0.500 | 0.150 |
| | 0.8 V | |
| AGDL | 0.300 | 0.489 |
| AMPL | 0.300 | 0.464 |
| ACL | 0.300 | 0.397 |
| CGDL | 0.300 | 0.150 |
| CMPL | 0.300 | 0.150 |
| CCL | 0.300 | 0.150 |

Table 4.6: Optimization history and $\frac{dF}{db}$ evolution for the 0.6 V operating condition.

| Iteration | $\varepsilon_{AGDL}$ | $\varepsilon_{CGDL}$ | $dF/db_{AGDL}$ | $dF/db_{CGDL}$ |
|---|---|---|---|---|
| 0 | 0.500 | 0.500 | -0.0138 | -0.801 |
| 1 | 0.472 | 0.340 | 0.0113 | -0.783 |
| 2 | 0.495 | 0.183 | -0.0105 | -4.167 |
| 3 | 0.465 | 0.150 | 0.0201 | -5.886 |
| 4 | 0.475 | 0.150 | 0.0092 | -6.352 |
| 5 | 0.493 | 0.150 | -0.0090 | -6.357 |
| 6 | 0.475 | 0.150 | 0.0087 | -6.352 |
| 7 | 0.493 | 0.150 | -0.0085 | -6.352 |

$$I = 0.1145 \text{ A}. \tag{4.54}$$

The corresponding improvement in the current is

$$\text{Objective Increase (\%)} = 9.44. \tag{4.55}$$

These results demonstrate that the optimized design obtained using the reduced adjoint model also leads to a significant improvement when evaluated with the full two-phase model, yielding an increase of approximately $9.4\%$ in the output current. The numerical simulations were performed using the same set of physical and transport parameters as listed in Tab. 4.8.

Table 4.7: Optimization history and $\frac{dF}{db}$ evolution for the 0.8 V case.

| Iteration | $\varepsilon_{AGDL}$ | $\varepsilon_{CGDL}$ | $dF/db_{AGDL}$ | $dF/db_{CGDL}$ |
|---|---|---|---|---|
| 0 | 0.300 | 0.300 | 5.7746 | -0.9217 |
| 1 | 0.415 | 0.281 | 0.8774 | -1.1402 |
| 2 | 0.433 | 0.258 | 0.6066 | -1.4850 |
| 3 | 0.463 | 0.184 | 0.2489 | -4.9431 |
| 4 | 0.476 | 0.150 | 0.1351 | -5.2509 |
| 5 | 0.483 | 0.150 | 0.0687 | -5.2537 |
| 6 | 0.486 | 0.150 | 0.0357 | -5.2550 |
| 7 | 0.489 | 0.150 | 0.0116 | -5.2559 |

| **Parameter** | **Symbol** | **Value / Units** |
|---|---|---|
| Faraday's constant | $F$ | $96485.34\ \mathrm{C/mol}$ |
| Universal gas constant | $R$ | $8.314\ \mathrm{J/(mol \cdot K)}$ |
| Condensation rate | $\gamma_{\mathrm{cond}}$ | $1\ \mathrm{s^{-1}}$ |
| Evaporation rate | $\gamma_{\mathrm{evap}}$ | $5 \times 10^{-5}\ \mathrm{Pa^{-1}\,s^{-1}}$ |
| Absolute permeability | $K_0$ | $3 \times 10^{-12}\ \mathrm{m^2}$ |
| Reference temperature | $T_{ref}$ | $343.15\ \mathrm{K}$ |
| $O_2$ diffusivity in $H_2O$ vapor | $D_{O_2-H_2O}$ | $2.82 \times 10^{-5}\ \mathrm{m^2/s}$ |
| $O_2$ diffusivity in $N_2$ | $D_{O_2-N_2}$ | $2.2 \times 10^{-5}\ \mathrm{m^2/s}$ |
| $H_2O$ diffusivity in $N_2$ | $D_{H_2O-N_2}$ | $2.56 \times 10^{-5}\ \mathrm{m^2/s}$ |
| $H_2$ diffusivity in $H_2O$ vapor | $D_{H_2-H_2O}$ | $9.15 \times 10^{-5}\ \mathrm{m^2/s}$ |
| Reference pressure | $p_{ref}$ | $1\ \mathrm{atm}$ |
| Surface tension | $\sigma$ | $0.0625\ \mathrm{N/m}$ |
| Nafion volume fraction (CL) | $\varepsilon_{pell}^{Naf}$ | $0.3$ |
| Cathode exchange current density | $i_{fe,0}^{ref}$ | $120\ \mathrm{A/m^3}$ |
| Anode exchange current density | $j_{ae,0}^{ref}$ | $1 \times 10^{8}\ \mathrm{A/m^3}$ |
| Reference concentration $O_2$ | $C_{O_2}^{ref}$ | $5.4\ \mathrm{mol/m^3}$ |
| Reference concentration $H_2$ | $C_{H_2}^{ref}$ | $26.3\ \mathrm{mol/m^3}$ |
| Anode transfer coefficient | $\alpha_{a,e}$ | $0.5$ |
| Cathode transfer coefficient | $\alpha_{c,e}$ | $0.5$ |
| Reference current density | $I_{ref}$ | $6000\ \mathrm{A/m^2}$ |
| Cathode stoichiometry | $\xi_c$ | $1$ |
| Anode stoichiometry | $\xi_a$ | $1$ |
| Cathode electrons | $z_c$ | $2$ |
| Anode electrons | $z_a$ | $2$ |

Table 4.8: Physical and electrochemical parameters used in the full two-phase PEMFC simulations.

# Chapter 5

# Conclusions

In this diploma thesis, the baseline two-phase OpenFuelCell2 [22] framework was adopted and extended for fully 3D simulations of PEMFCs systems. The main objective was the development of an adjoint-based optimization software capable of providing accurate gradients for the optimization of the porous media properties. To achieve this, the original porous resistance formulation was upgraded through the incorporation of an analytical Kozeny–Carman [1] correlation, introducing an explicit dependency of the porous media resistance on the local porosity field. This modification enabled a physically consistent sensitivity pathway between the design variables ($\varepsilon$) and the resulting flow resistance, which was essential for the subsequent optimization procedure.

Furthermore, two different approaches for the treatment of the Nernst potential within the electrochemical source terms were implemented and evaluated. The first approach demonstrated higher adjoint derivatives and larger deviations; however, these deviations decreased with mesh refinement. In contrast, the second approach resulted in smaller deviations and lower adjoint derivatives, providing improved agreement with the finite-difference sensitivity evaluation.

The continuous adjoint formulation was developed incrementally, initially for the electric domain and subsequently extended to the single-phase representation of the fluid-flow equations within the adopted two-phase primal framework. The final formulation resulted in a complete three-equation adjoint system consisting of the continuity, momentum, and charge transport equations. The accuracy and consistency of the developed adjoint implementation were rigorously validated through comparison with finite-differences. The adjoint-derived gradients showed excellent agreement with the finite-difference results, with all deviations remaining below $5\%$ for both the coarse and fine 3D meshes.

Following the verification stage, the developed adjoint model was integrated into an optimization loop for the iterative update of the porosity distribution under two different operating conditions ($0.6$ V and $0.8$ V). The optimization procedure exhibited stable convergence behaviour and achieved a measurable improvement of the objective functional. Specifically, increases of approximately $3.9\%$ and $5\%$ in the generated current density were obtained for the respective operating conditions, demonstrating the effectiveness of the proposed

adjoint-based optimization methodology.

Overall, the obtained results confirm the capability of continuous adjoint methods, when integrated into advanced multiphysics fuel cell solvers, to provide accurate sensitivity information and enable meaningful performance improvements. The developed software establishes a robust foundation for future extensions, in which the incorporation of additional models simulating physical phenomena such as heat transfer, species transport, water dissolution, and more advanced two-phase flow effects within the adjoint formulation. These developments will enable the investigation of more complex degradation mechanisms, water management strategies, and long-term durability aspects in 3D industrial-scale fuel cell configurations.

# Bibliography


[1] Bear, J.: Dynamics of Fluids in Porous Media. American Elsevier Publishing Company, New York (1972)

[2] Breeze, P.: Fuel Cells. Academic Press (2018)

[3] Dreyer, W., Guhlke, C., Müller, R.: A new perspective on the electron transfer: recovering the butler–volmer equation in non-equilibrium thermodynamics. Physical Chemistry Chemical Physics **18**, 24966–24983 (2016). https://doi.org/10.1039/c6cp04142f

[4] Eikerling, M., Kornyshev, A.A.: Electrochemical impedance of polymer electrolyte fuel cells. Journal of Electroanalytical Chemistry (2002)

[5] Jiao, K., Li, X.: Water transport in polymer electrolyte membrane fuel cells. Progress in Energy and Combustion Science **37**(3), 221–291 (2011). https://doi.org/10.1016/j.pecs.2010.06.002

[6] Khotseng, L.: Fuel Cell Thermodynamics. IntechOpen (2020). https://doi.org/10.5772/intechopen.90141

[7] Lamprinidis, P.: Modeling and Optimization of Gas Diffusion Layer in Fuel Cells, in the OpenFOAM environment. Diploma thesis, NTUA, Athens, Greece (2021)

[8] Leverett, M.C.: Capillary behavior in porous solids. Transactions of the AIME **142**, 152–169 (1941)

[9] Linden, F.V.D.: Methodology and tools for the optimization of the pem fuel cell break-in proce-dure. HAL Open Science (2022)

[10] Monfaredi, M., Papoutsis-Kiachagias, E., Asouti, V., Giannakoglou, K.: Analysis and optimization of pem fuel cells using openfoam. In: Gauger, N., Giannakoglou, K., Papadrakakis, M., Périaux, J. (eds.) Proceedings of EUROGEN / ECCOMAS. Chania, Crete, Greece (Jun 2023)

[11] Qi, P., Wu, Z., Mou, J., Wu, D., Gu, Y., Xu, M., Li, Z., Luo, Y.: A review of water management in proton exchange membrane fuel cell systems. Sustainable Energy Fuels **9**, 72–97 (2025). https://doi.org/10.1039/D4SE01020E

[12] Schiller, L., Naumann, A.: A drag coefficient correlation. Zeitschrift des Vereins Deutscher Ingenieure **77**, 318–320 (1935)

[13] Shinagawa, T., Garcia-Esparza, A.T., Takanabe, K.: Insight on tafel slopes from a microkinetic analysis of aqueous electrocatalysis for energy conversion. Scientific Reports **5** (2015). https://doi.org/10.1038/srep13801

[14] Taguchi, G.: Introduction to Quality Engineering. Asian Productivity Organization, Tokyo (1986)

[15] Tranter, T.G., et al.: Capillary hysteresis in neutrally wettable fibrous media. Transport in Porous Media **121**(3), 597–620 (2017)

[16] Valle, F.: Electrocatalyst degradation in high temperature PEM fuel cells. Ph.D. thesis, Universita Degli Studi Di Trieste (2014)

[17] Wang, N., Cheng, Y., Fan, X., Ding, R., Zhou, H., Xin, C., Shi, R.: Progressive topology-curvature optimization of flow channel for pemfc and performance assessment. Frontiers in Energy **19**, 395–412 (2025). https://doi.org/10.1007/s11708-025-0978-4

[18] Weber, A.Z., Newman, J.: Modeling transport in polymer-electrolyte fuel cells. Chemical Reviews **104**(10), 4679–4726 (2004). https://doi.org/10.1021/cr020711e

[19] Xu, H., Liu, Z.: Multiphysics coupling of electrochemistry and heat/mass transfer in pem electrolyzer and synergistic optimization for novel flow fields and graded gdl. International Journal of Hydrogen Energy **220**, 154087 (2026). https://doi.org/https://doi.org/10.1016/j.ijhydene.2026.154087, https://www.sciencedirect.com/science/article/pii/S036031992600724X

[20] Yan, W., Wang, J., Li, J., Wang, G.: Optimizing structural parameters of pemfc based on taguchi method. World Electric Vehicle Journal **14**(3), 76 (2023). https://doi.org/10.3390/wevj14030076

[21] Yuan, W., Tang, Y., Pan, M., Li, Z., Tang, B.: Model prediction of effects of operating parameters on proton exchange membrane fuel cell performance. Renewable Energy **35**(3), 656–666 (2010). https://doi.org/10.1016/j.renene.2009.09.021

[22] Zhang, S., Hess, S., Marschall, H., Reimer, U., Beale, S., Lehnert, W.: openfuelcell2: A new computational tool for fuel cells, electrolyzers, and other electrochemical devices and processes. Computer Physics Communications (2023), forthcoming

**Εθνικό Μετσόβιο Πολυτεχνείο**
Σχολή Μηχανολόγων Μηχανικών
Τομέας Ρευστών
Μονάδα Παράλληλης Υπολογιστικής Ρευστοδυναμικής
& Βελτιστοποίησης

**Διατύπωση, Προγραμματισμός και Χρήση της Συνεχούς Συζυγούς Μεθόδου για Κυψέλες Καυσίμου με Μεμβράνη Ανταλλαγής Πρωτονίων**

Διπλωματική Εργασία

**Όθων Γ. Φρέσκος**

Επιβλέπων Καθηγητής:
Κυριάκος Χ. Γιαννάκογλου, Καθηγητής ΕΜΠ

Αθήνα, 2026

**Εκτενής Περίληψη**

# Αντικείμενο και Στόχος της Διπλωματικής Εργασίας

Η διπλωματική εργασία επικεντρώνεται στην ανάπτυξη της μαθηματικής διατύπωσης της συνεχούς συζυγούς μεθόδου και στην υλοποίηση ενός υπολογιστικού εργαλείου για τη βελτιστοποίηση κυψελών καυσίμου με μεμβράνη ανταλλαγής πρωτονίων (PEMFCs), μέσω των υπολογιζόμενων παραγώγων, στο υπολογιστικό περιβάλλον του OpenFOAM. Ο βασικός στόχος της μελέτης είναι η ενίσχυση της απόδοσης της κυψέλης, με κριτήριο την αύξηση της παραγόμενης πυκνότητας ρεύματος, μέσω της βελτιστοποίησης της χωρικής κατανομής του πορώδους στις πορώδεις περιοχές της κυψέλης. Η επιλογή του πορώδους ως μεταβλητής σχεδιασμού δεν είναι τυχαία, καθώς επηρεάζει άμεσα κρίσιμες φυσικές διεργασίες, όπως η μεταφορά μάζας, η διαπερατότητα, η αποτελεσματική διάχυση, η ηλεκτρική αγωγιμότητα και, κατ' επέκταση, τη συνολική απόδοση του συστήματος.

# Σημασία και Φυσική των PEMFCs

Οι κυψέλες καυσίμου τύπου PEMFCs αποτελούν μία από τις πιο υποσχόμενες τεχνολογίες ηλεκτροχημικής μετατροπής ενέργειας, καθώς μετατρέπουν απευθείας τη χημική ενέργεια

του καυσίμου($H_2$) σε ηλεκτρική ενέργεια χωρίς διαδικασία καύσης. Η λειτουργία τους βασίζεται στη διάσπαση του υδρογόνου στο άνοδο, στη μεταφορά των πρωτονίων μέσω της μεμβράνης και στη ροή των ηλεκτρονίων μέσω εξωτερικού ηλεκτρικού κυκλώματος, παράγοντας ηλεκτρικό ρεύμα.

Στην κάθοδο πραγματοποιείται η αντίδραση αναγωγής του οξυγόνου, όπου τα πρωτόνια και τα ηλεκτρόνια αντιδρούν σχηματίζοντας νερό ως τελικό παραπροϊόν. Παρά τα σημαντικά πλεονεκτήματα της τεχνολογίας, η μοντελοποίηση της συνοδεύεται από έντονη φυσική πολυπλοκότητα, καθώς εμπλέκονται ταυτόχρονα φαινόμενα ροής ρευστού, μεταφοράς μάζας, μεταφοράς θερμότητας, διαχείρισης ύδατος και ηλεκτροχημικών αντιδράσεων.

# Υπολογιστικό Μοντέλο και Δομή του Πεδίου

Η εργασία βασίζεται στην ανάπτυξη ενός υπολογιστικού μοντέλου πολλών περιοχών, το οποίο περιλαμβάνει τις περιοχές ροής αερίων, τα στρώματα διάχυσης αερίων (GDLs), τα καταλυτικά στρώματα (CLs), τη μεμβράνη και τα ηλεκτρικά αγώγιμα στερεά.

Η ανάπτυξη του λογισμικού είχε ως αφετηρία ανοικτό κώδικα με όνομα "OpenFuelCell2" [22] ο οποίος ελέγχθηκε, εμπλουτίσθηκε και, στη συνέχεια, δημιουργήθηκε ο αντίστοιχος συζυγής κώδικας για επιλεγείσες συναρτήσεις στόχους. Το πρωτεύον μοντέλο είναι πολυσυστατικό, πολυφασικό και πολυπεριοχικό και περιλαμβάνει εξισώσεις διατήρησης μάζας και ορμής, μεταφοράς ειδών, ηλεκτρικού δυναμικού, μεταφοράς θερμότητας, καθώς και διάχυσης νερού στη μεμβράνη.

# Υπολογιστικές Περιοχές και Σύζευξη Φυσικών Πεδδίων

Στο Σχ. 5.1 παρουσιάζονται οι επιμέρους περιοχές και οι υπολογιστικοί τομείς του μοντέλου. Είναι σημαντικό να σημειωθεί ότι μία φυσική περιοχή μπορεί να ανήκει σε περισσότερους από έναν τομείς, ανάλογα με το είδος των εξισώσεων που επιλύονται.

Οι υπολογιστικοί τομείς διακρίνονται ως εξής:

- δύο τομείς ρευστού (ανόδου και καθόδου), που περιλαμβάνουν τα κανάλια αερίου (GCs) και τις πορώδεις στρώσεις (GDLs και CLs),
- τρείς ηλεκτρικοί τομείς (ηλεκτρονικός ανόδου και καθόδου), που περιλαμβάνουν τις διπολικές πλάκες (BPs), τις πορώδεις στρώσεις και τα καταλυτικά στρώματα, ένας πρωτονικός τομέας, ο οποίος περιλαμβάνει τη μεμβράνη και τα καταλυτικά στρώματα.

# Γενικές Εξισώσεις και Φυσική Μοντελοποίηση

Στον Πίν. 5.1 παρουσιάζονται οι κύριες εξισώσεις που επιλύονται σε κάθε φυσικό τομέα. Το μοντέλο περιλαμβάνει εξισώσεις συνέχειας και ορμής για το ρευστό, μεταφοράς ειδών, αγωγής ηλεκτρικού φορτίου, μεταφοράς νερού στη μεμβράνη και εξίσωση ενέργειας.

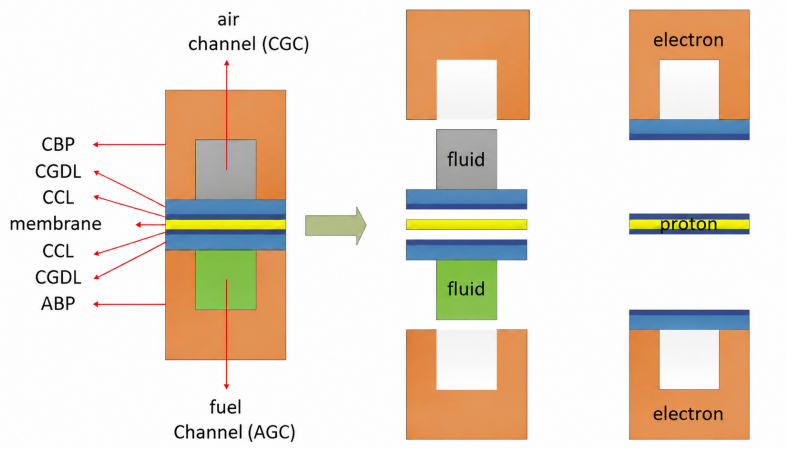


Figure 5.1: Υπολογιστικές περιοχές και τομείς του μοντέλου. Πηγή: [22]

Ιδιαίτερη σημασία έχει η σύζευξη μεταξύ των τομέων, καθώς το ηλεκτρικό πεδίο συνδέεται τόσο με το ρευστό όσο και με το συνολικό πεδίο μέσω των ηλεκτροχημικών όρων πηγής, ενώ το ρευστό και το θερμικό πεδίο συζευγνύονται μέσω της ταχύτητας, της μεταφοράς ενέργειας και των όρων πηγής.

# Μοντελοποίηση Πορωδών Μέσων

Ιδιαίτερη έμφαση δόθηκε στη μοντελοποίηση των πορωδών περιοχών της κυψέλης καυσίμου, καθώς τα συγκεκριμένα στρώματα παρουσιάζουν έντονη αλληλεπίδραση μεταξύ φαινομένων μεταφοράς μάζας, ροής ρευστού, ηλεκτρικής αγωγιμότητας και ηλεκτροχημικών αντιδράσεων. Ειδικότερα, τα στρώματα διάχυσης αερίων (Gas Diffusion Layers – GDL) και τα καταλυτικά στρώματα χαρακτηρίζονται από σύνθετη μικροδομή, η οποία επηρεάζει σημαντικά τη μεταφορά των αντιδρώντων προς τις ενεργές περιοχές της κυψέλης.

Για την ποσοτική περιγραφή της επίδρασης της μικροδομής, το πορώδες $\varepsilon$ επιλέχθηκε ως βασική μεταβλητή σχεδιασμού. Η μεταβολή του πορώδους επηρεάζει άμεσα την αντίσταση που παρουσιάζει το πορώδες μέσο στη διέλευση του ρευστού, μέσω της μεταβολής της διαπερατότητας και των αδρανειακών φαινομένων. Η συσχέτιση αυτή περιγράφηκε μέσω των σχέσεων Kozeny–Carma [1], οι οποίες συνδέουν τη μικροδομική παράμετρο του πορώδους με τους συντελεστές αντίστασης του μέσου:

$$\alpha(\varepsilon) = \frac{150(1-\varepsilon)^2}{d_p^2 \varepsilon^3}, \beta(\varepsilon) = \frac{3.5(1-\varepsilon)}{d_p \varepsilon^3}. \tag{5.1}$$

όπου $d_p$ αποτελεί το χαρακτηριστικό μέγεθος των πόρων. Ο συντελεστής $\alpha$ σχετίζεται με τις ιξώδεις απώλειες του ρευστού λόγω τριβής στα τοιχώματα των πόρων, ενώ ο συντελεστής $\beta$ περιγράφει τις αδρανειακές απώλειες που εμφανίζονται για αυξημένες ταχύτητες ροής. Συνεπώς, η αύξηση ή η μείωση του πορώδους μεταβάλλει την αντίσταση του πορώδους μέσου και κατ' επέκταση την κατανομή της ροής και τη μεταφορά των αντιδρώντων μέσα στην κυψέλη. Οι παραπάνω σχέσεις εισάγονται απευθείας στον όρο πηγής της

| **Πρωτεύουσες Εξισώσεις** | | **Περιοχές** |
|---|---|---|
| Διατήρηση Μάζας | $\frac{\partial(\alpha_\phi \rho_\phi)}{\partial t} + \nabla \cdot (\alpha_\phi \rho_\phi \mathbf{v}_\phi) = R_\phi$ | Τομέας Ρευστού(GCs, GDLs, CLs) |
| Διατήρηση Ορμής(Eulerian-Eulerian) | $\frac{\partial(\alpha_\phi \rho_\phi \mathbf{v}_\phi)}{\partial t} + \nabla \cdot (\alpha_\phi \rho_\phi \mathbf{v}_\phi \mathbf{v}_\phi) = -\alpha_\phi \nabla p + \alpha_\phi \rho_\phi \mathbf{g} + \mathbf{M}_\phi + \mathbf{S}_{\text{Darcy},\phi}$ | Τομέας Ρευστού(GCs, GDLs, CLs) |
| Μεταφορά Χημικών Ειδών | $\frac{\partial(\rho_g \alpha_g Y_i)}{\partial t} + \nabla \cdot (\rho_g \alpha_g \mathbf{v}_g Y_i) = \nabla \cdot (\rho_g \alpha_g D_i^{\text{eff}} \nabla Y_i) + \alpha_g R_i$ | Τομέας Ρευστού(GCs, GDLs, CLs) |
| Μεταφορά Ρεύματος | $\nabla \cdot (\sigma_E \nabla \Phi_E) = J_E, \quad \nabla \cdot (\sigma_I \nabla \Phi_I) = J_I$ | Τομέας Ρεύματος(Ηλεκτρονικός, Πρωτονικός) |
| Διάχυση Νερού | $\frac{\rho_m}{EW}\frac{\partial \lambda}{\partial t} + \nabla \cdot \left(\frac{n_d \mathbf{i}_I}{F}\right) = \nabla \cdot \left(\frac{\rho_m}{EW} D_m^{\text{eff}} \nabla \lambda\right) + R_\lambda$ | Μεμβράνη |
| Διατήρηση Ενέργειας | $\frac{\partial(\rho C_p T)}{\partial t} + \rho C_p \mathbf{v} \cdot \nabla T = \nabla \cdot (k_{\text{eff}} \nabla T) + Q$ | Ολικός Τομέας |
| Ηλεκτροχημικοί Όροι Πηγής (Butler–Volmer) | $j = i_0 \prod_i \left(\frac{C_i}{C_{\text{ref}}}\right)^\xi \left[e^{-\frac{\alpha z F \eta}{RT}} - e^{\frac{(1-\alpha) z F \eta}{RT}}\right]$ | CLs |

Table 5.1: Σύνοψη των πρωτεύουσων εξισώσεων στους αντίστοιχους υπολογιστικούς τομείς.

εξίσωσης ορμής, ο οποίος περιγράφει την αντίσταση που ασκεί το πορώδες υλικό στη ροή. Συγκεκριμένα, χρησιμοποιήθηκε η διατύπωση Darcy–Forchheimer, σύμφωνα με την οποία ο όρος αντίστασης $\mathbf{S}_{\text{Darcy},\phi}$ δίνεται από:

$$\mathbf{S}_{\text{Darcy},\phi} = -\left(\mu_\phi \alpha + \frac{1}{2}\rho_\phi |\mathbf{v}_\phi| \beta\right) \mathbf{v}_\phi, \tag{5.2}$$

όπου $\mu_\phi$ και $\rho_\phi$ είναι το δυναμικό ιξώδες και η πυκνότητα του ρευστού αντίστοιχα, ενώ $\mathbf{v}_\phi$ αποτελεί την ταχύτητα του ρευστού μέσα στο πορώδες μέσο. Ο πρώτος όρος της παρένθεσης αντιστοιχεί στην ιξώδη συνιστώσα της αντίστασης (Darcy term), ενώ ο δεύτερος όρος αντιπροσωπεύει την αδρανειακή συνιστώσα (Forchheimer term).

Με τον τρόπο αυτό, η επίδραση της μικροδομής του πορώδους υλικού ενσωματώνεται στην εξίσωση διατήρησης της ορμής μέσω των συντελεστών $\alpha(\varepsilon)$ και $\beta(\varepsilon)$, επιτρέποντας την προσομοίωση της επίδρασης διαφορετικών κατανομών πορώδους στη ροή των αερίων και στη συνολική απόδοση της κυψέλης καυσίμου. Το συγκεκριμένο μοντέλο πορωδών μέσων ενσωματώθηκε στον πρωτεύοντα επιλύτη που αναπτύχθηκε στην εργασία αυτή.

# Οριακές Συνθήκες

Στον ρευστοδυναμικό τομέα εφαρμόζονται οι οριακές συνθήκες που συνοψίζονται στον Πίν. 5.2, περιλαμβάνοντας συνθήκες εισόδου, εξόδου και τοιχωμάτων.

Table 5.2: Οριακές συνθήκες του ρευστοδυναμικού τομέα.

| **Συνοριακή Επιφάνεια** | **Θέση** | **Ταχύτητα v** | **Πίεση** $p$ |
|---|---|---|---|
| $S_I$ | Είσοδοι GCs | Fixed value | $\partial p/\partial n = 0$ |
| $S_W$ | Στερεά Όρια | $v_i = 0$ | $\partial p/\partial n = 0$ |
| $S_O$ | Έξοδοι CGs | $\partial v_i/\partial n = 0$ | Fixed value |

Αντίστοιχα, οι οριακές συνθήκες του ηλεκτρικού τομέα παρουσιάζονται στο Σχ. 5.2, όπου εφαρμόζονται συνθήκες Dirichlet για το ηλεκτρικό δυναμικό και συνθήκες μηδενικής Neumann.

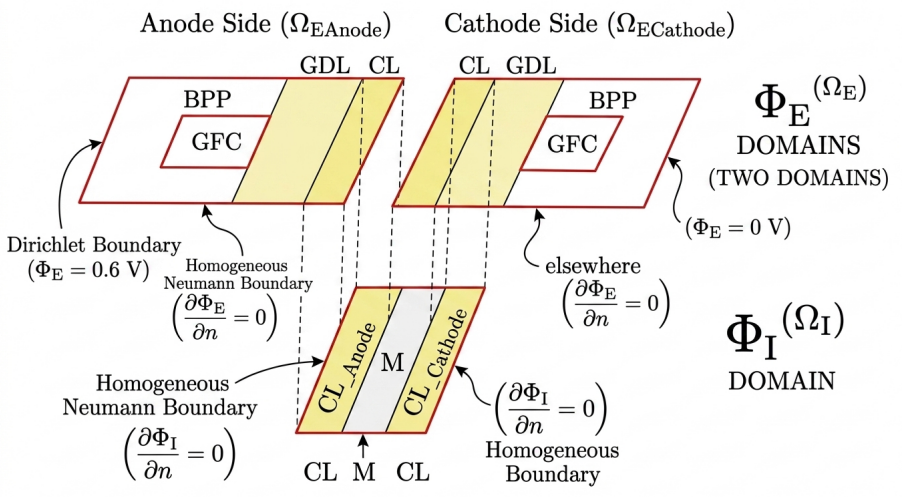


Figure 5.2: Οριακές συνθήκες του ηλεκτρικού τομέα.

# Ενσωμάτωση Δυναμικού Nernst

Ιδιαίτερη προσοχή δόθηκε στη σωστή ενσωμάτωση του δυναμικού Nernst στη διατύπωση του ηλεκτρικού μοντέλου. Το δυναμικό Nernst αντιπροσωπεύει το αντιστρέψιμο ηλεκτροχημικό δυναμικό της αντίδρασης και μπορεί να εισαχθεί είτε ρητά μέσω των υπερτάσεων ενεργοποίησης είτε έμμεσα μέσω των οριακών συνθηκών του ηλεκτρικού δυναμικού.

Εδώ αναπτύχθηκαν δύο μαθηματικά ισοδύναμες διατυπώσεις, οι οποίες οδηγούν στην ίδια φυσική περιγραφή αλλά διαφοροποιούνται στη μαθηματική τους υλοποίηση. Η επιλογή της κατάλληλης προσέγγισης επηρεάζει τον ορισμό των υπερτάσεων στα καταλυτικά στρώματα και, κατά συνέπεια, τη διαμόρφωση των όρων πηγής στις εξισώσεις Butler–Volmer.

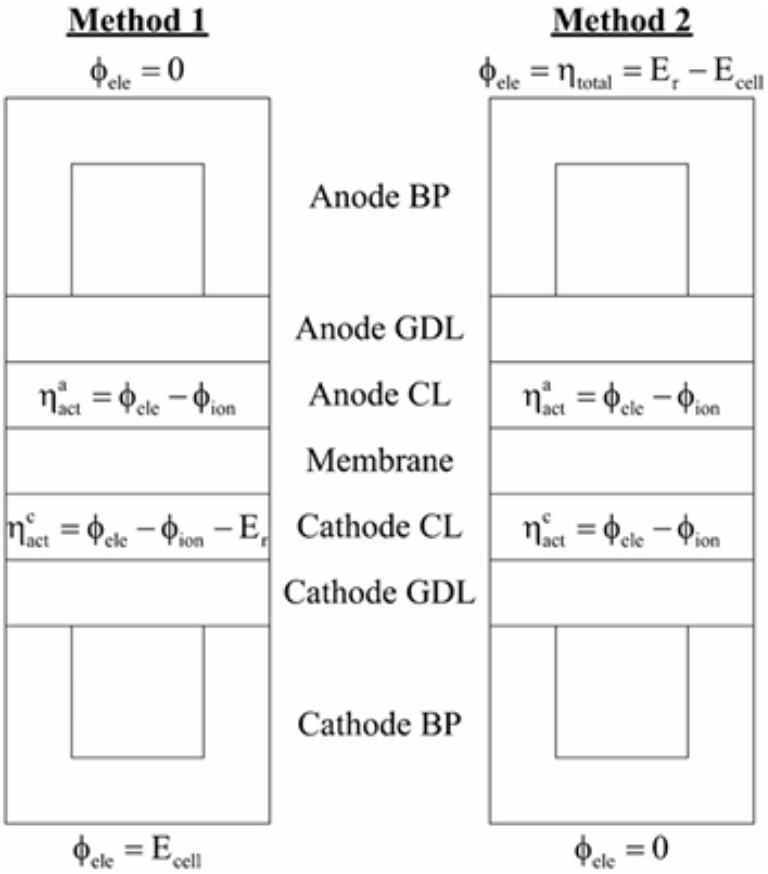


Figure 5.3: Σύγκριση δύο προσεγγίσεων για την ενσωμάτωση του δυναμικού Nernst.

# Γεωμετρία και Υπολογιστικό Πλέγμα

Η γεωμετρία της υπό μελέτη κυψέλης καυσίμου PEMFC περιλαμβάνει τις διπολικές πλάκες, τα κανάλια ροής αερίων, τις πορώδεις περιοχές (GDLs και CLs) και τη μεμβράνη ανταλλαγής πρωτονίων. Το συνολικό μήκος των καναλιών είναι 30 mm, όπως παρουσιάζεται στο Σχ. 5.4.

Η αριθμητική διακριτοποίηση του πεδίου πραγματοποιήθηκε με 3Δ δομημένα πλέγματα (`blockMesh`). Η τελική μορφή του υπολογιστικού πλέγματος και ο διαχωρισμός των επιμέρους φυσικών περιοχών παρουσιάζεται στο Σχ. 5.5. Για την αριθμητική επίλυση χρησιμοποιήθηκαν δύο πλέγματα διαφορετικής ανάλυσης, με στόχο τη διερεύνηση της επίδρασης της διακριτοποίησης στα αποτελέσματα και την αξιολόγηση της αριθμητικής σύγκλισης του μοντέλου.

Το πυκνό πλέγμα αντιστοιχεί σε υψηλής ανάλυσης διακριτοποίηση με αυξημένο όμως υπολογιστικό κόστος. Αντίθετα, το αραιό πλέγμα μειώνει σημαντικά το υπολογιστικό φορτίο και χρησιμοποιείται κυρίως για συγκριτικούς και επιβεβαιωτικούς υπολογισμούς. Η χρήση των δύο πλεγμάτων επιτρέπει την ποιοτική και ποσοτική αξιολόγηση της ευαισθησίας των αποτελεσμάτων ως προς την ανάλυση του πλέγματος.

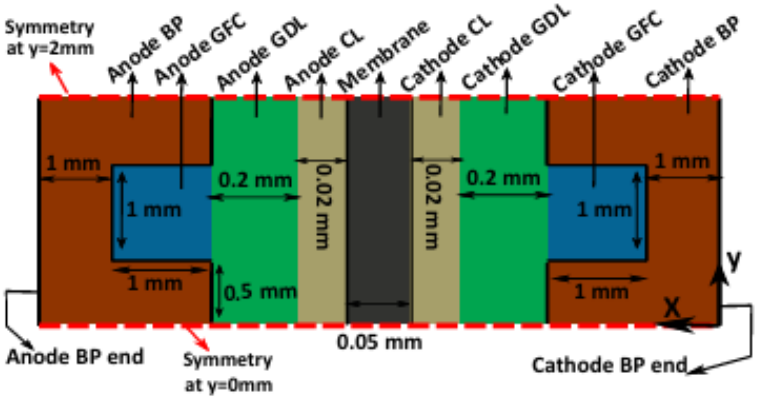


Figure 5.4: Διδιάστατη γεωμετρία της PEMFC (χωρίς κλίμακα).

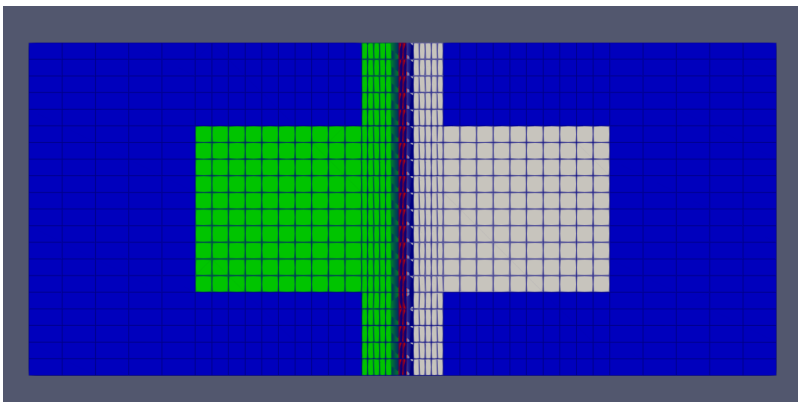

Figure 5.5: Υπολογιστικό πλέγμα και διαχωρισμός φυσικών περιοχών.

# Μαθηματική Διατύπωση και Ανάπτυξη της Συζυγούς Μεθόδου στον Ηλεκτρικό Τομέα

Η ανάπτυξη της συζυγούς (adjoint) μεθόδου αποτελεί το κεντρικό θεωρητικό και υπολογιστικό σκέλος της παρούσας εργασίας. Στο αρχικό στάδιο, η συζυγής διατύπωση περιορίζεται αποκλειστικά στον ηλεκτρικό τομέα δηλαδή διαφορίζεται μόνο η εξίσωση μεταφοράς ρεύματος Πίν. 5.1, ενώ τα υπόλοιπα φυσικά πεδία πλήν του ηλεκτρικού δυναμικού $\Phi$ θεωρούνται γνωστά και ανεξάρτητα από τη μεταβλητή σχεδιασμού.

Το πρόβλημα διατυπώνεται υπό ποτενσιοστατικές συνθήκες λειτουργίας, όπως παρουσιάζεται και στο Σχ. 5.2, όπου το επιβαλλόμενο δυναμικό θεωρείται δεδομένο και το ρεύμα προκύπτει από τη λύση του συστήματος. Η αντικειμενική συνάρτηση ορίζεται ως το ολοκλήρωμα της ογκομετρικής πυκνότητας ρεύματος σε επιλεγμένο καταλυτικό στρώμα (ACL ή CCL), ανάλογα με το εξεταζόμενο σενάριο.

Οι μεταβλητές σχεδιασμού του προβλήματος βελτιστοποίησης ορίζονται μέσω της κατανομής του πορώδους στις επιμέρους πορώδεις περιοχές της κυψέλης καυσίμου. Συγκεκριμένα, θεωρείται ότι το πορώδες παραμένει σταθερό εντός κάθε διακριτής περιοχής, με αποτέλεσμα

κάθε περιοχή να περιγράφεται από μία ανεξάρτητη μεταβλητή σχεδιασμού.

Με τη χρήση της μεθόδου πολλαπλασιαστών Lagrange σχηματίζεται η επαυξημένη συνάρτηση κόστους, στην οποία ενσωματώνεται ο περιορισμός της εξίσωσης ηλεκτικού φορτίου. Από την απαίτηση μηδενισμού των όρων της επαυξημένης συνάρτησης προκύπτει η συζυγής διατύπωση, καθώς και οι αντίστοιχες συζυγείς οριακές συνθήκες (βλ. Πίν. 5.3).

Στο αρχικό μοντέλο λαμβάνονταν υπόψη τα στρώματα διάχυσης αερίων (GDL) και τα καταλυτικά στρώματα (CL). Στο πλαίσιο της παρούσας εργασίας, το μοντέλο επεκτάθηκε με την εισαγωγή ενός επιπλέον μικροπορώδους στρώματος (MPL) μεταξύ του GDL και του καταλυτικού στρώματος.

Ως αποτέλεσμα, η άνοδος και η κάθοδος της κυψέλης περιγράφονται πλέον από τρεις ανεξάρτητες μεταβλητές σχεδιασμού η καθεμία, οι οποίες αντιστοιχούν στο πορώδες του GDL, του MPL και του CL. Συνολικά, το πρόβλημα βελτιστοποίησης περιλαμβάνει έξι μεταβλητές σχεδιασμού, οι οποίες επιτρέπουν τη διερεύνηση της επίδρασης διαφορετικών κατανομών πορώδους στην ηλεκτροχημική απόδοση της κυψέλης.

Η συζυγής μέθοδος επιτρέπει τον υπολογισμό των παραγώγων της αντικειμενικής συνάρτησης ως προς τις μεταβλητές σχεδιασμού με υπολογιστικό κόστος που δεν εξαρτάται από τον αριθμό των σχεδιαστικών παραμέτρων. Το γεγονός αυτό αποτελεί σημαντικό πλεονέκτημα έναντι των πεπερασμένων διαφορών.

Η εγκυρότητα της συζυγούς διατύπωσης αξιολογήθηκε μέσω σύγκρισης των παραγώγων που προκύπτουν από τη συζυγή μέθοδο με εκείνες που υπολογίζονται αριθμητικά μέσω κεντρικών πεπερασμένων διαφορών. Τα αποτελέσματα παρουσιάζονται στους Πίν. 5.4 και 5.5. Παρατηρείται πολύ καλή συμφωνία μεταξύ των δύο μεθόδων, ιδιαίτερα για μικρά βήματα διαταραχής της πορώδους τιμής.

## Η συζυγής μέθοδος του συζευγμένου μοντέλου τριών εξισώσεων

Σε επόμενο στάδιο η συζυγής διατύπωση επεκτάθηκε ώστε να συμπεριλάβει και το ρευστοδυναμικό πεδίο, με αποτέλεσμα τη δημιουργία ενός συζευγμένου συζυγούς μοντέλου τριών εξισώσεων (Διατήρηση Μάζας-Όρμης / Μεταφορά Ρεύματος Πίν. 5.1). Η επέκταση αυτή είναι σημαντική, διότι το πορώδες δεν επηρεάζει μόνο τις ηλεκτρικές ιδιότητες (ηλεκτρική αγωγιμότητα), αλλά και τη ροή του αερίου μέσα στην κυψέλη, άρα και τη μεταφορά των αντιδρώντων προς τα ενεργά σημεία των καταλυτικών στρωμάτων. Η συζυγής ανάλυση του πεδίου ροής παρέχει πρόσθετες παραγώγους, οι οποίες ενσωματώνονται στην τελική κατεύθυνση βελτιστοποίησης. Και σε αυτήν την περίπτωση, η συζυγής διατύπωση επαληθεύτηκε μέσω σύγκρισης με πεπερασμένες διαφορές, επιβεβαιώνοντας ότι το λογισμικό παραμένει ακριβές και για το πλήρες συζευγμένο πρόβλημα.

Η αντικειμενική συνάρτηση καθώς και οι μεταβλητές σχεδιασμού ορίζονται όπως περιγράφηκαν στον Πίν. 5.3.

Η βελτιστοποίηση πραγματοποιείται με επαναληπτικό αλγόριθμο τύπου απότομης καθόδου. Σε κάθε κύκλο, οι συζυγείς μεταβλητές προσφέρουν τις παραγώγους της συνάρτησης στόχου ως προς το πορώδες των επιμέρους περιοχών, και οι τιμές αυτές χρησιμοποιούνται για την ενημέρωση του σχεδιαστικού πεδίου. Η διαδικασία αυτή στοχεύει στη σταδιακή ανακατανομή του πορώδους με τέτοιο τρόπο ώστε να αυξάνεται η παραγόμενη πυκνότητα

| Στοιχείο | Συζυγής Διατύπωση |
|---|---|
| **Αντικειμενική Συνάρτηση** | $$J = \int_{\Omega_{CL}} j \, d\Omega$$ Μέγιστο συνολικό ρεύμα στο επιλεγμένο καταλυτικό στρώμα (ACL ή CCL). |
| **Μεταβλητές Σχεδιασμού** | $\varepsilon_{\text{AGDL}}, \varepsilon_{\text{AMPL}}, \varepsilon_{\text{ACL}}$ $\varepsilon_{\text{CGDL}}, \varepsilon_{\text{CMPL}}, \varepsilon_{\text{CCL}}$ Το πρόβλημα βελτιστοποίησης ανάγεται σε έξι ανεξάρτητες μεταβλητές σχεδιασμού. |
| **Επαυξημένη Συνάρτηση** | $$J_{\text{aug}} = \int_{\Omega_{CL}} j \, d\Omega + \int_{\Omega} \phi \, R^{\Phi} \, d\Omega$$ |
| **Εξίσωση Συζυγούς (Ηλεκτρονικός Τομέας)** | $$\nabla \cdot (\sigma_E \nabla \phi_E) + C_k - \phi_E \delta S_E - \phi_I \delta S_I = 0$$ |
| **Εξίσωση Συζυγούς (Πρωτονικός Τομέας)** | $$\nabla \cdot (\sigma_I \nabla \phi_I) + C_k - \phi_I \delta S_I - \phi_E \delta S_E = 0$$ |
| **Οριακές Συνθήκες Συζυγούς Προβλήματος** | **Dirichlet (γνωστό δυναμικό):** $$\phi = 0$$ **Neumann (γνωστή ροή ρεύματος):** $$\sigma \frac{\partial \phi}{\partial n} = 0$$ Ισχύουν αντίστοιχα για τον ηλεκτρονικό και ιοντικό τομέα. |
| **Συνάρτηση Ευαισθησίας** | $$\delta J = -\int_{\Omega_E} \nabla \phi_E \cdot \nabla \Phi_E \, \delta\sigma_E \, d\Omega - \int_{\Omega_I} \nabla \phi_I \cdot \nabla \Phi_I \, \delta\sigma_I \, d\Omega$$ Τελική μορφή συζυγών παραγώγων ευαισθησίας ως προς τις μεταβλητές σχεδιασμού πορώδους. |

Table 5.3: Σύνοψη αντικειμενικής συνάρτησης, μεταβλητών σχεδιασμού, επαυξημένης διατύπωσης, συζυγών εξισώσεων, οριακών συνθηκών και τελικών παραγώγων για το πρόβλημα βελτιστοποίησης της κυψέλης καυσίμου.

| Περιοχή | Κεντρικές ΠΔ | Adjoint | Απόκλιση (%) |
|---|---|---|---|
| *Αραιό Πλέγμα* | | | |
| AGDL | -0.007929183 | -0.007501527 | 5.393 |
| ACL | -0.000195090 | -0.000192667 | 1.242 |
| AMPL | -0.000296728 | -0.000294846 | 0.634 |
| *Πυκνό Πλέγμα* | | | |
| AGDL | -0.007799778 | -0.007560392 | 3.069 |
| ACL | -0.000191860 | -0.000189925 | 1.008 |
| AMPL | -0.000296018 | -0.000293141 | 0.326 |

Table 5.4: Σύγκριση μεταξύ πεπερασμένων διαφορών ($\delta\epsilon = 0.01$) και της συζυγούς τεχνικής για τη μέθοδο 1.

| Περιοχή | Κεντρικές ΠΔ | Adjoint | Απόκλιση (%) |
|---|---|---|---|
| *Αραιό Πλέγμα* | | | |
| AGDL | -0.004777719 | -0.004700378 | 1.619 |
| ACL | -0.000121849 | -0.000120401 | 1.188 |
| AMPL | -0.000182312 | -0.000181186 | 0.617 |
| *Πυκνό Πλέγμα* | | | |
| AGDL | -0.004715906 | -0.004680907 | 0.742 |
| ACL | -0.000120493 | -0.000119321 | 0.973 |
| AMPL | -0.000180590 | -0.000180201 | 0.215 |

Table 5.5: Σύγκριση μεταξύ κεντρικών πεπερασμένων διαφορών ($\delta\epsilon = 0.01$) και της συζυγούς τεχνικής για τη μέθοδο 2.

ρεύματος. Η συγκεκριμένη μεθοδολογία είναι κατάλληλη για προβλήματα μεγάλου μεγέθους, καθώς αποφεύγει το τεράστιο υπολογιστικό κόστος που θα απαιτούσε η ξεχωριστή διαφόριση ως προς κάθε μεταβλητή σχεδιασμού.

Στον Πίν. 5.6 παρουσιάζεται η μαθηματική δομή του ανεπτυγμένου συζυγούς μοντέλου. Η εισαγωγή των διαφορικών περιορισμών στην επαυξημένη συνάρτηση μέσω των πολλαπλασιαστών Lagrange επιτρέπει τον ταυτόχρονο υπολογισμό των συζυγών μεταβλητών για το πεδίο ταχυτήτων, πίεσης και ηλεκτρικού δυναμικού.

Για την επικύρωση της αξιοπιστίας των υπολογιζόμενων συζυγών κλίσεων, πραγματοποιήθηκε ποσοτική σύγκριση με τη μέθοδο Κεντρικών Πεπερασμένων Διαφορών, τα αποτελέσματα της οποίας συνοψίζονται στον Πίν. 5.7. Η σύγκριση διεξήχθη για το στρώμα διάχυσης αερίου της ανόδου (AGDL) για τάσεις 0.6 V και 0.8 V και διαφορετικές πυκνότητες υπολογιστικού πλέγματος. Η μέγιστη απόκλιση μεταξύ των δύο μεθόδων δεν υπερβαίνει το $1.64\%$, γεγονός που πιστοποιεί την ακρίβεια της μαθηματικής γραμμικοποίησης και της αριθμητικής υλοποίησης του συζυγούς κώδικα, ακόμη και για το σύνθετο συζευγμένο φαινόμενο.

Στο Σχ. 5.6 απεικονίζεται η σύγκλιση της διαδικασίας βελτιστοποίησης μέσω της εξέλιξης της αντικειμενικής συνάρτησης σε συνάρτηση με τους κύκλους του αλγορίθμου, για τις δύο εξεταζόμενες τάσεις λειτουργίας. Παρατηρείται ότι ο αλγόριθμος επιτυγχάνει

| Στοιχείο | Συζυγής Διατύπωση |
|---|---|
| **Επαυξημένη Συνάρτηση** | $$F_{\text{aug}} = F + \int_\Omega u_i R_i^v \, d\Omega + \int_\Omega q R^p \, d\Omega + \int_\Omega \phi R^\Phi \, d\Omega$$ |
| **Συζυγείς Εξισώσεις (Σύστημα 3 εξισώσεων)** | $$\frac{\partial q}{\partial x_j} v_j - \frac{\partial u_i}{\partial x_j} v_j v_i - \left( \frac{\partial u_i}{\partial x_i} - \delta J_{\text{Nernst}} \right) \frac{p}{\rho} = 0$$ $$\frac{\partial q}{\partial x_i} \rho - \frac{\partial u_j}{\partial x_i} \rho v_j - \frac{\partial u_i}{\partial x_j} \rho v_j - \mu \frac{\partial}{\partial x_j} \left( \frac{\partial u_i}{\partial x_j} + \frac{\partial u_j}{\partial x_i} \right) + \delta S_{\text{Darcy}} = 0$$ $$\frac{\partial}{\partial x_j} \left( \sigma_E \frac{\partial \Phi_E}{\partial x_j} \right) + C_k - \Phi_E \delta S_E - \Phi_I \delta S_I + C_k q \frac{\omega \sum M_i}{zF} = 0$$ |
| **Οριακές Συνθήκες Συζυγούς Προβλήματος** | **Είσοδος:** $q = 0,\ u_t = 0,\ u_n = 0$<br>**Τοίχωμα:** $\partial q / \partial n = 0,\ u = 0$<br>**Έξοδος:** $q = 0$, τύπου Robin για $u_i$<br>**Ηλεκτρικά πεδία:** Dirichlet ή Neumann όπως στο πρωτεύον πρόβλημα |

Table 5.6: Συνοπτική διατύπωση του συζυγούς μοντέλου 3 εξισώσεων (πεδίο ροής–συνέχεια–ηλεκτρικό πεδίο).

Table 5.7: Σύγκριση των αποτελεσμάτων κεντρικών πεπερασμένων διαφορών και των παραγώγων από τη συζυγή μέθοδο για την περιοχή AGDL.

| Τάση | Πλέγμα | $e_0$ | $\Delta e$ | Κεντρικές ΠΔ | Συζυγής Μέθοδος | Απόκλιση (%) |
|---|---|---|---|---|---|---|
| 0.6 V | Πυκνό | 0.5 | 0.001 | 0.005948924 | 0.006002257 | -0.896517 |
| 0.6 V | Αραιό | 0.5 | 0.001 | 0.005853548 | 0.005949379 | -1.637138 |
| 0.8 V | Αραιό | 0.3 | 0.001 | 0.074164382 | 0.073196540 | 1.304996 |

μονονότονη αύξηση της παραγόμενης πυκνότητας ρεύματος, η τάση σταθεροποίησης (πλατό) που εμφανίζεται στη συνέχεια υποδεικνύει την επιτυχή προσέγγιση της βέλτιστης κατανομής πορώδους υπό τους τεθέντες γεωμετρικούς και φυσικούς περιορισμούς. Συνολικά, η βελτιστοποίηση απέδωσε αύξηση κατά $3.9\%$ και $5.0\%$ για τις τάσεις λειτουργίας 0.6 V και 0.8 V, αντίστοιχα.

Οι Πίν. 5.8 και 5.9 παρέχουν μια λεπτομερή καταγραφή της πορείας βελτιστοποίησης για τα 0.6 V και 0.8 V αντίστοιχα, παρουσιάζοντας τις τιμές του πορώδους ($\varepsilon$) και των αντίστοιχων παραγώγων ευαισθησίας ($dJ/db$) για τα στρώματα διάχυσης της ανόδου (AGDL) και της καθόδου (CGDL). Από την ανάλυση των δεδομένων προκύπτει ότι το CGDL αποτελεί την κυρίαρχη περιοχή επιρροής, καθώς οι ευαισθησίες του είναι σημαντικά υψηλότερες σε απόλυτη τιμή, οδηγώντας το πορώδες στο κατώτατο επιτρεπτό φυσικό όριο ($e_{CGDL} = 0.150$). Αντίθετα, η περιοχή του AGDL εμφανίζει μικρότερες και εναλλασσόμενες

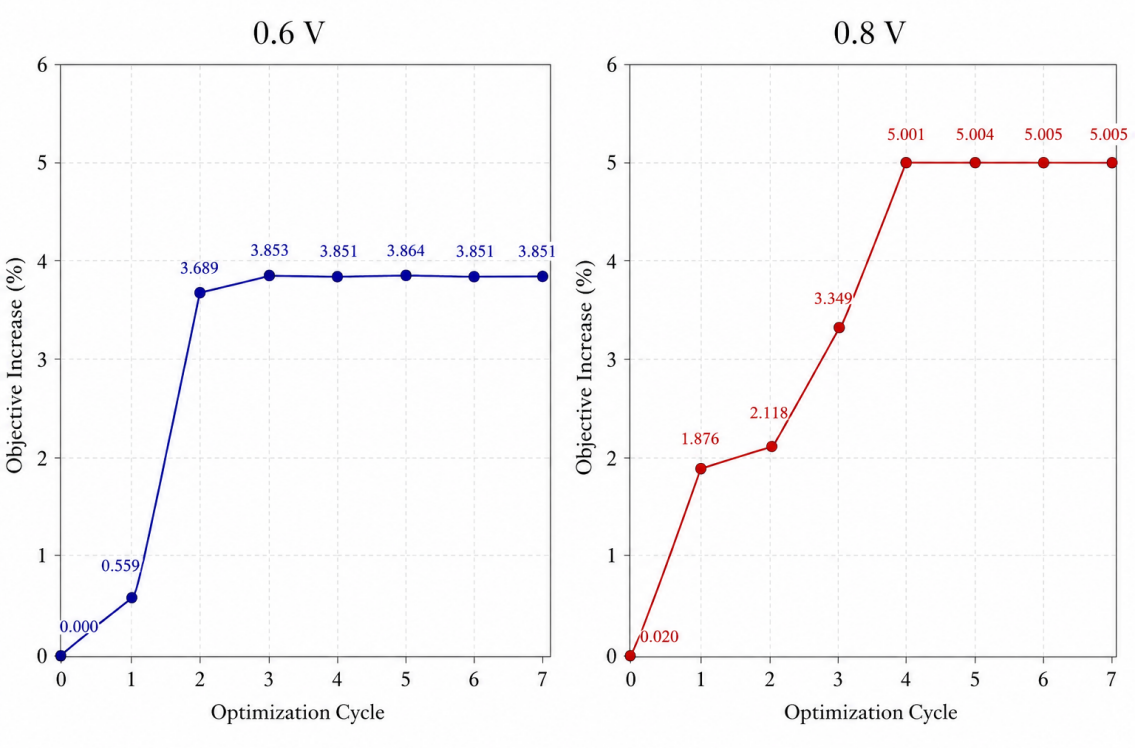


Figure 5.6: Εξέλιξη της βελτίωσης της αντικειμενικής συνάρτησης κατά τη διάρκεια των κύκλων βελτιστοποίησης στα 0.6 V (αριστερά) και 0.8 V (δεξιά).

Table 5.8: Ιστορικό βελτιστοποίησης και εξέλιξη παραγώγων για λειτουργία στα 0.6 V.

| Κύκλος | $e_{AGDL}$ | $e_{CGDL}$ | $dJ/db_{AGDL}$ | $dJ/db_{CGDL}$ |
|---|---|---|---|---|
| 0 | 0.500 | 0.500 | -0.0138 | -0.801 |
| 1 | 0.472 | 0.340 | 0.0113 | -0.783 |
| 2 | 0.495 | 0.183 | -0.0105 | -4.167 |
| 3 | 0.465 | 0.150 | 0.0201 | -5.886 |
| 4 | 0.475 | 0.150 | 0.0092 | -6.352 |
| 5 | 0.493 | 0.150 | -0.0090 | -6.357 |
| 6 | 0.475 | 0.150 | 0.0087 | -6.352 |
| 7 | 0.493 | 0.150 | -0.0085 | -6.352 |

τιμές ευαισθησιών, υποδηλώνοντας μια πιο ήπια ανακατανομή γύρω από την αρχική τιμή σχεδιασμού.

Μετά την ολοκλήρωση της διαδικασίας βελτιστοποίησης, η οποία βασίστηκε στο απλοποιημένο μονοφασικό συζυγές μοντέλο τριών εξισώσεων, η βέλτιστη γεωμετρία που προέκυψε αξιολογήθηκε χρησιμοποιώντας τον πλήρη διφασικό πρωτεύοντα επιλύτη. Το στάδιο αυτό είναι απαραίτητο για την επαλήθευση της απόδοσης της βελτιστοποιημένης διαμόρφωσης υπό την πλήρη φυσική περιγραφή του προβλήματος, η οποία λαμβάνει υπόψη όλα τα σχετικά φαινόμενα διφασικής μεταφοράς.

Το ηλεκτρικό ρεύμα που αντιστοιχεί στην αρχική γεωμετρία είναι

$$I_0 = 0.1046 \text{ A}. \tag{5.3}$$

Μετά την εφαρμογή της βέλτιστης γεωμετρίας στο πλήρες διφασικό μοντέλο, το παραγόμενο ηλεκτρικό ρεύμα διαμορφώθηκε σε

$$I_{opt} = 0.1145 \text{ A}. \tag{5.4}$$

Η αντίστοιχη βελτίωση του ηλεκτρικού ρεύματος υπολογίζεται ως

$$\text{Ποσοστιαία Αύξηση} = 9.44\%. \tag{5.5}$$

Τα αποτελέσματα αυτά καταδεικνύουν ότι η βέλτιστη γεωμετρία, η οποία προέκυψε μέσω της διαδικασίας βελτιστοποίησης με το απλοποιημένο συζυγές μοντέλο, οδηγεί επίσης σε σημαντική βελτίωση της απόδοσης όταν αξιολογείται με το πλήρες διφασικό μοντέλο. Συγκεκριμένα, παρατηρείται αύξηση του παραγόμενου ηλεκτρικού ρεύματος κατά περίπου $9.4\%$.

Table 5.9: Ιστορικό βελτιστοποίησης και εξέλιξη παραγώγων για τη συνθήκη λειτουργίας στα 0.8 V.

| Κύκλος | $e_{AGDL}$ | $e_{CGDL}$ | $dJ/db_{AGDL}$ | $dJ/db_{CGDL}$ |
|---|---|---|---|---|
| 0 | 0.300 | 0.300 | 5.7746 | -0.9217 |
| 1 | 0.415 | 0.281 | 0.8774 | -1.1402 |
| 2 | 0.433 | 0.258 | 0.6066 | -1.4850 |
| 3 | 0.463 | 0.184 | 0.2489 | -4.9431 |
| 4 | 0.476 | 0.150 | 0.1351 | -5.2509 |
| 5 | 0.483 | 0.150 | 0.0687 | -5.2537 |
| 6 | 0.486 | 0.150 | 0.0357 | -5.2550 |
| 7 | 0.489 | 0.150 | 0.0116 | -5.2559 |

# Επίλογος

Τα αριθμητικά αποτελέσματα έδειξαν ότι η συνεχής συζυγής διατύπωση παρέχει συνεπείς και ακριβείς παραγώγους και ότι η επαναληπτική βελτιστοποίηση οδηγεί σε βελτίωση της ηλεκτροχημικής απόδοσης του PEMFC. Η επαλήθευση του μοντέλου με πεπερασμένες διαφορές επιβεβαίωσε την ορθότητα της υλοποίησης, ενώ οι υπολογιστικές δοκιμές κατέδειξαν ότι η προσέγγιση αυτή μπορεί να υποστηρίξει τόσο την ανάλυση όσο και τον σχεδιασμό βελτιωμένων δομών κυψελών καυσίμου. Επιπλέον, η εργασία αναδεικνύει τη σημασία της προσεκτικής αριθμητικής διαχείρισης, καθώς το πρόβλημα είναι ιδιαίτερα μη γραμμικό, συζευγμένο και ευαίσθητο σε επιλογές οριακών και αρχικών συνθηκών.

Ένα επιπλέον πλεονέκτημα της παρούσας εργασίας είναι ότι συνδυάζει τη θεωρητική διατύπωση με ένα πλήρως λειτουργικό υπολογιστικό περιβάλλον. Η ανάπτυξη στο OpenFOAM

επιτρέπει την εκμετάλλευση δοκιμασμένων αριθμητικών εργαλείων, την ευελιξία στην τροποποίηση του κώδικα και τη δυνατότητα επέκτασης σε πιο σύνθετα προβλήματα στο μέλλον. Η ενσωμάτωση της συζυγούς μεθόδου σε ένα τέτοιο περιβάλλον καθιστά το πλαίσιο ιδιαίτερα χρήσιμο για περαιτέρω έρευνα, είτε για πιο λεπτομερή φυσική μοντελοποίηση είτε για μελέτες σχεδιαστικής βελτιστοποίησης σε βιομηχανικής κλίμακας γεωμετρίες.

Συνολικά, η παρούσα διπλωματική εργασία συμβάλλει στην ανάπτυξη ενός πλήρους και συνεπούς υπολογιστικού πλαισίου για την ανάλυση και βελτιστοποίηση PEMFCs μέσω της συνεχούς συνοδού μεθόδου. Η προσέγγιση αυτή επιτρέπει την αποδοτική εξαγωγή ευαισθησιών ως προς το πορώδες, την αξιόπιστη επαλήθευση με πεπερασμένες διαφορές και τη συστηματική βελτίωση της απόδοσης του στοιχείου. Η μελέτη καταδεικνύει ότι η συνδυασμένη χρήση φυσικής μοντελοποίησης, αριθμητικής ανάλυσης και συνοδού βελτιστοποίησης μπορεί να προσφέρει ουσιαστικά αποτελέσματα στον σχεδιασμό προηγμένων ηλεκτροχημικών συστημάτων και να αποτελέσει τη βάση για μελλοντικές επεκτάσεις σε ακόμη πιο σύνθετα μοντέλα.

**Λέξεις-κλειδιά:** PEMFC, OpenFOAM, συνεχής συζυγής μέθοδος, βελτιστοποίηση, πορώδες, Kozeny–Carman, Nernst, υπολογιστική ρευστοδυναμική.